UNIVERSITY OF CALIFORNIA, SAN DIEGO

Epithelial wound response: How do cells know where they are and what to do after a wound?

A dissertation submitted in partial satisfaction of the requirements for the degree of Doctor of Philosophy

in

Chemistry

by

Linda Naomi Handly

Committee in charge:

Professor Roy Wollman, Chair
Professor Edward A. Dennis, Co-chair
Professor Amitabha Sinha
Professor Gurol Suel
Professor Susan S. Taylor

2017

The Dissertation of Linda Naomi Handly is approved, and it is acceptable in quality and form for publication on microfilm and electronically:

_____

_____

_____

_____

Co-Chair

_____

Chair

University of California, San Diego

2017

DEDICATION

To my mentors during my undergraduate education at Brigham Young University, Dr. Richard Watts and Dr. Emily Bates, thank you for instilling confidence in me that I can solve challenging scientific problems.

To Roy Wollman. Thank you for taking a risk on me as your first graduate student. I learned more than I ever thought possible.

To my many friends and co-workers during graduate school who motivated me to be better.

To my parents for prioritizing education and science since I was a child and supporting me through every trial I encountered during graduate school.

To Erika and Jonah. Thanks for being wonderful siblings.

To my Ojiichan. Thank you for teaching me to snatch every opportunity, for your never-ending support, and for always being proud of me.

To my dogs, Mia, Cleo, and Gretyl. Thank you for always putting a smile on my face.

TABLE OF CONTENTS

LIST OF FIGURES

LIST OF TABLES

LIST OF SUPPLEMENTARY FILES

Chapter 1: Paracrine Communication Maximizes Cellular Response Fidelity in Wound Signaling

1) Handly_Ch1SuppMovie1_Fluo4Ca2+Wound.avi

   Isotropic Ca^{2+} response to wounding. Ca^{2+} response to a 300μm wound, indicated by the Fluo-4 Ca^{2+} sensor. Upon wounding, Ca^{2+} response propagates isotropically from the wound. Movie time lapse is 5 minutes.

2) Handly_Ch1SuppMovie2_DualWound.avi

   Ca^{2+} and ERK dual wounding. Ca^{2+} and ERK are measured simultaneously using the fluoresecent reporter RGECO for Ca^{2+} (pink) and the ERK FRET sensor EKAREV (cyan). Ca^{2+} response is completed within 5 minutes whereas ERK response takes approximately 30 minutes.

ACKNOWLEDGEMENTS

I would like to acknowledge Professor Roy Wollman as the chair of my committee. His love for science and mentorship over the past 5 years has been invaluable.

The introduction, in full, is a reprint of the material as it appears in Handly, L.N.; Yao, J.; Wollman, R. Signal Transduction at the Single-Cell Level: Approaches to Study the Dynamic Nature of Signaling Networks. J. Mol. Biol. 2016, 428, 3669-3682. The dissertation author is the first author on this paper.

Chapter 1 in full is a reprint of the material as it appears in Handly, L.N.; Pilko, A.; Wollman, R. Paracrine communication maximizes cellular response fidelity in wound signaling. eLife. 2015, 4:e09652. The dissertation author is the first author on this paper.

Chapter 2 in full is a reprint of the material in press for publication as it appears in Handly, L.N.; Wollman, R. Wound induced Ca^{2+} wave propagates through a simple Release and Diffusion mechanism. Mol. Biol. Cell. 2017, In Press. The dissertation author is the first author on this paper.

Chapter 3 is a work in collaboration with Anna Pilko and Alon Oyler-Yaniv. The dissertation author is the author of this material.

VITA

2011	Bachelor of Science, Brigham Young University
2012-2014	Master of Science, University of California, San Diego
2017	Doctor of Philosophy, University of California, San Diego

PUBLICATIONS

Handly, L.N.; Wollman, R. *Wound induced Ca^{2+} wave propagates through a simple Release and Diffusion mechanism. Mol. Biol. Cell.* **2017,** In Press.

Handly, L.N.; Yao, J.; Wollman, R. *Signal Transduction at the Single-Cell Level: Approaches to Study the Dynamic Nature of Signaling Networks*. *J. Mol. Biol*. **2016**, *428, 3669-3682*.

Handly, L.N.; Pilko, A.; Wollman, R. *Paracrine communication maximizes cellular response fidelity in wound signaling. eLife.* **2015,** *4:e09652.*

Hilton, R.J.; Zhang, B., **Martineau, L.N.****; Watt, G.D., Watt, R.K.; *Anion deposition into ferritin. J. Inorganic Biochem.* **2012**, *108, 8-14*.

Snow, C.L.; **Martineau, L.N.****; Hilton, R.J.; et al. *Ferritin Iron Mineralization Proceeds by Different Mechanisms in MOPS and Imidazole Buffers. J. Inorganic Biochem.* **2011,** *105*, 972-977.

***Previously Martineau, L.N.*

FIELDS OF STUDY

Major Field: Biochemistry

Studies of the iron core of Ferritin
Professor Richard K. Watt

Studies of wound response signaling
Professor Roy Wollman

ABSTRACT OF THE DISSERTATION

Epithelial wound response: How do cells know where they are and what to do after a wound?

by

Linda Naomi Handly

Doctor of Philosophy in Chemistry

University of California, San Diego, 2017

Professor Roy Wollman, Chair

Wound healing begins as soon as the wound occurs and can continue for days, weeks, or even months. Although decades of research have established the multiple-steps required to heal a wound, little is known about the cellular response immediately following the wound. Furthermore, because the location of the wound is relevant to the healing process, healthy cells responding to a wound require positional information, or knowing where they are in relation to the wound. Thus, there are two important questions not fully understood in wound healing: 1. How do cells know where they are? and 2. How do the initial signaling

mechanisms influence downstream genetic expression and overall healing? Here, using recent technological advancements in single-cell fluorescent microscopy and fluorescent biomarkers, we determine that ATP, an initial signaling molecule released from wounded cells, creates spatial patterns immediately following an epithelial wound using a simple Release and Diffusion mechanism. Then we determine that epithelial cells use paracrine signaling to spatially average the initial wound response signals over a specific distance to maximize the signal-to-noise ratio. Finally, we establish a method titled SpaSeq (Spatial Sequencing) that utilizes FACS and RNA-Seq in addition to fluorescent proteins to measure the spatio-temporal gene expression patterns following a wound.

INTRODUCTION

Signal transduction at the single-cell level: Approaches to study the dynamic nature of signaling networks

Abstract

Signal transduction, or how cells interpret and react to external events, is a fundamental aspect of cellular function. Traditional study of signal transduction pathways involves mapping cellular signaling pathways at the population level. However, population averaged readouts do not adequately illuminate the complex dynamics and heterogeneous responses found at the single-cell level. Recent technological advances to observe cellular response, computationally model signaling pathways, and experimentally manipulate cells now enables studying signal transduction at the single-cell level. These studies will enable deeper insights into the dynamic nature of signaling networks.

Introduction

Defining cellular signaling pathways is important to understand many biological processes including tissue development, immune response, cancer development, cellular growth and migration, and more. Traditional biological approaches to study cellular signal transduction include bulk assays to measure cellular response at the population level. Although these studies have been useful in mapping signaling pathways and making qualitative predictions, population averaging can often mask the spatial and temporal dynamics important in physiological processes. Furthermore, population averaging results in information loss regarding biological variability that often has important physiological implications.

Over the last few years, technological advancements in measuring, manipulating, and modeling signaling activities at single-cell resolution has enabled researchers to go beyond the limitations of population-averaged bulk assays. These new studies often reveal that previous knowledge about signaling dynamics at the population level may not be the complete picture. For example, earlier studies of the p53 signaling pathway provided support for damped oscillations to stimulus [1]. However, single-cell studies revealed that there are no damped oscillations in the individual cell. Instead, differences in pulse cycle between cells created a population average behavior showing damped oscillations [2]. More recent work on this pathway elucidates the complex dynamic patterns of p53 activities that cells use to encode and transmit information [3]. Analysis based solely on population level readouts completely masked these insights. Similarly, single-cell studies of the NF-κB pathway show complex digital activation patterns in individual cells that are hidden by population level studies [4,5]. Single-cell studies have uncovered the importance of temporal dynamics in information transmission through cellular signaling networks [6]. Furthermore, single-cell information exposes the complexity of cellular response distribution. The implications of cellular heterogeneity is a key area of research important to understanding fundamental issues such as variability of drug response at the cellular and organism level [7].

The ability to fully comprehend signal transduction at the single-cell level requires advancements in how we observe cells, model cellular behavior, and manipulate biological systems. However, single-cell studies continue to utilize the same overarching approach as

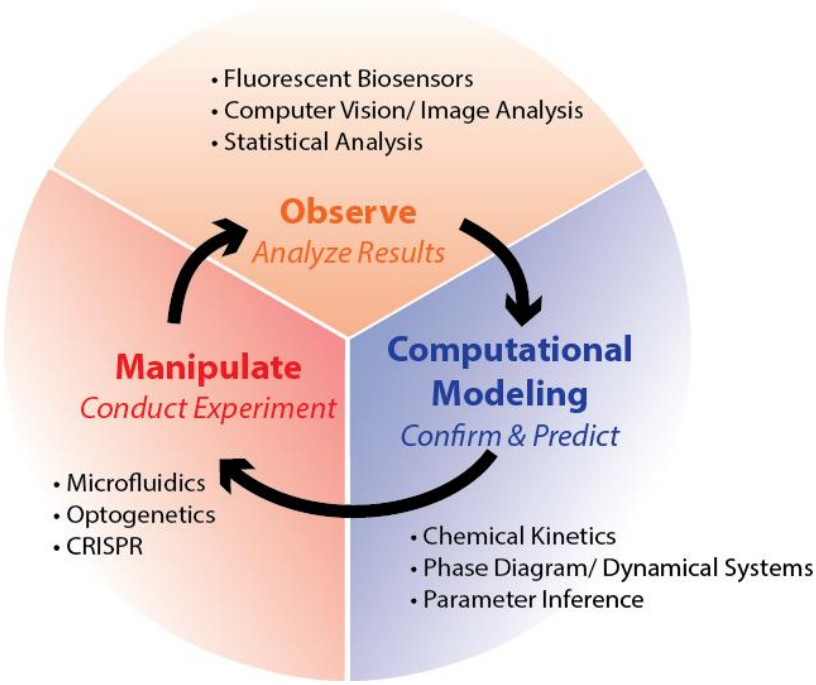

Figure 0.1 Studying Signal Transduction at the Single-Cell Level. Advancements in observing single-cells, computational modeling, and techniques to manipulate cells in a spatio-temporal manner enable insights into signal transduction at the single-cell level.

traditional population level studies (Figure 1). Observing cells at the single-cell level is now possible using better fluorescent biosensors and single-cell analysis techniques. Additionally, the development of complex computational algorithms can dissect the dynamics and distribution of single-cell behavior found in the complicated and rich datasets produced by single-cell measurements. Computational models confirm intricacies in cellular network behavior that are difficult to elucidate through observation alone. Additionally, predictions made using computational models facilitate directed experiments. Although the specific

techniques to manipulate biological systems is different, the overarching theme of changing the internal and external environment of cells remains the same between single-cell and bulk-level assays. In the following review we will discuss the specific methods and developments used to observe, model, and manipulate biological systems to study dynamic signal transduction at the single-cell level.

Observe: Dynamical measurements of signaling activities at single-cell resolution

Fluorescent biosensors and computational image analysis have enabled evaluating the distribution of the cellular response across a population in real-time. Traditional biological techniques such as western blots only provide a population average level readout (Figure 2). As a result, this type of analysis lacks both temporal and spatial resolution. In contrast, fluorescent biosensors can capture dynamic cellular events in living cells at subcellular resolution. Increased cellular, spatial, and temporal resolution has contributed to rich datasets that require image analysis algorithms to fully capture the complexity of the data. Furthermore, meaningful interpretations of single-cell datasets require advanced statistical methods such as dimensionality reduction and information theory to quantify and properly interpret the distribution of cellular behavior.

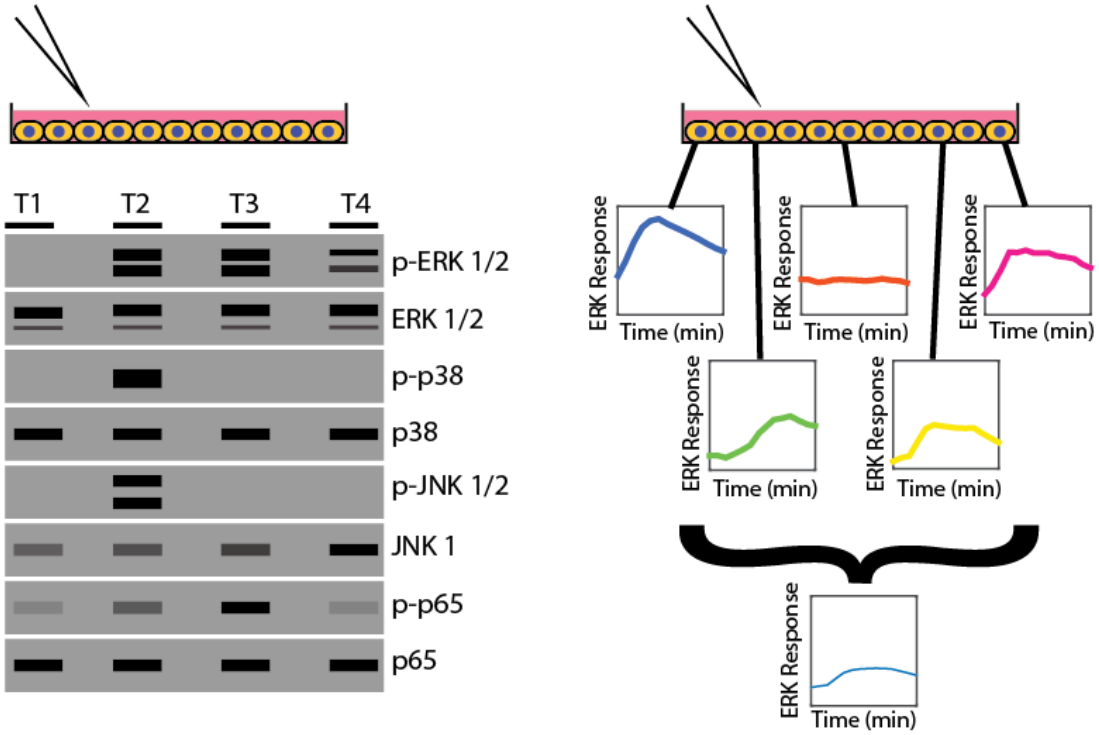

Figure 0.2. Bulk Assays vs Single-Cell Assays to Study Response Dynamics. Bulk-level assays, such as Western blots, provide population level response with limited temporal resolution (T1-T4, left). Fluorescent microscopy using biosensors shows the distribution of the population response at the single-cell level (right).

Sampling Cellular Signaling Networks-Expanding the Palette of Fluorescent Biosensors

Reliable dynamic biosensors are crucial for live single-cell analysis of signal transduction. Fluorescent biosensors function by coupling one or more fluorescent proteins to an activity sensing domain. Biosensors have been developed for a number of different signaling molecules by designing the sensing domain for a specific signaling molecule [8]. The intricate process of designing sensing domains compatible with fluorescent proteins to properly report signaling molecule activity has been reviewed elsewhere and will not be addressed here [8–11]. Rather, here we will discuss advancements in biosensor development that have led to an enriched variety of fluorescent proteins with optimized molecular properties and improved modular design of fluorescent reporters.

Increasing the variety of optimized fluorescent proteins enables multiplex imaging to expand the number of potential biological readouts. Significant efforts have been made to optimize fluorescent proteins to enhance brightness and contrast, increase photostability, and expand the range of available colors, where color is defined as the unique excitation and emission spectra of a protein. For example, cyan, green, and red fluorescent proteins have improved in all three areas with the development of mTurquoise2, mClover3, and mRuby3, respectively [12,13]. Improving fluorescent proteins also enables expanding the range of available colors for a specific molecule. Increasing the variety of colors for a specific molecule allows researchers to select a fluorescent protein color that does not interfere with the spectra of other fluorescent proteins in a given experiment. Researchers now have a much wider range of fluorescent proteins and can choose them based on the needs of the experiment rather than resorting to what is available [10,14].

The development of fluorescent biosensors to report dynamic cellular activity has evolved rapidly over the past 15 years. Kinase activity is of particular interest due to the large number of biological processes regulated by protein phosphorylation such as cell growth, cell cycle, and immune response [15]. The ability to monitor kinase activity using genetically encoded FRET biosensors presented a modular design adaptable to different proteins with increased dynamic range [16]. Zhang et al. first developed a genetically encoded protein kinase A (PKA) activity reporter (AKAR) in 2001 using a generalizable FRET backbone [17]. The development of AKAR2 enabled measurement of reversible PKA activity by increasing cellular phosphatase sensitivity [18]. By taking advantage of better fluorescent proteins, such as those discussed above, further improvements were made in AKAR dynamic range with AKAR3 and AKAR4, with each iteration brighter than the last [19,20]. AKAR also expanded beyond the commonly used CFP/YFP FRET pair with GFP/RFP AKAR2 and CFP/RFP

AKAR3 variants [21,22]. Using improved fluorescent proteins not only increased the dynamic range of the sensors, but also enabled co-imaging with other FRET pairs to increase the number of biological readouts per experiment [22]. In addition to improvements in design and color range, AKARs were also modified to localize to different areas of the cell to measure PKA dynamics in specific locations such as the plasma membrane (AKAR4-Kras) and sarcoplasmic reticulum (SR-AKAR3) [23,24].

The advent and improvements made to AKARs also triggered the development of a multitude of FRET kinase reporters. Perhaps the most intuitive adaptation was to other protein kinases with activity reporters for protein kinase B, protein kinase C, and protein kinase D [25–27]. Other kinase reporters also followed the AKAR design such as the c-Jun N-terminal kinase (JNK) activity reporter JNKAR1 and the extracellular signal-regulated kinase (ERK) activity reporter EKAR [28,29]. To make the AKAR design more generalizable and improve the dynamic range, Komatsu et al developed an intramolecular FRET biosensor with an optimized backbone using a longer linker to make the fluorescent protein pair completely "distance-dependent" as opposed to "orientation-dependent" [30]. The increased length of the backbone, termed the Eevee (EV) backbone, makes the FRET backbone adaptable to kinases and GTPases. Removing the need to optimize each sensor per biological readout makes biosensor development simpler and faster. This backbone was adapted to make FRET biosensors for PKA (AKAREV), ERK (EKAREV), JNK (JNKEV), among many others [30]. FRET kinase biosensors continue to be used to measure single-cell dynamics to solve complex problems while still improving in design. For example, the EKAREV sensor was used to quantitatively measure ERK dynamics during proliferation and was again improved in design to increase the signal-to-noise ratio [31,32].

A deeper understanding of signaling networks requires measuring multiple dynamic biological outputs simultaneously. Although FRET biosensors present advantages over single-protein reporters such as an increased dynamic range, the use of two fluorescent proteins makes measuring multiple biological outputs during a single assay challenging. Regot et al developed a kinase activity reporter that measures the phosphorylation of kinases using reporter translocation rather than fluorescent strength as an activation indicator [33]. Here, rather than comparing the ratio between two fluorescent proteins, the fluorescent ratio between the nucleus and cytoplasm measures the level of kinase activation in a cell. Additionally, using a few simple design principles, KTRs can be adapted for a variety of kinases.

Live single-cell fluorescent imaging provides quantifiable dynamic spatio-temporal data not available with population level analysis techniques (Figure 2). The use of fluorescent biosensors now enables better subcellular resolution in addition to spatial and temporal dynamics of a specific protein, gene, or second messenger of interest. Despite extensive advancements made in fluorescent proteins and biosensors, experiments remain limited in the number of biological readouts during a single experiment in comparison to assays such as western blots that have a plentiful selection of detection antibodies (Figure 2). This is in part due to limitations set by the number of fluorescent proteins able to be used in a single read-out. Although each fluorescent protein color has a unique excitation and emission spectra, overlap between spectra makes using multiple proteins in a single experiment challenging. Practically, experiments remain limited to a maximum of 3-4 fluorescent proteins depending on the specific microscope configuration. Furthermore, biosensor development requires specific expertise in protein kinetics and structure, constraining the variety of available sensors for specific biological readouts. Continuing developments to improve fluorescent protein

properties as well as improved modular designs will open new avenues for improved live-cell multiplex imaging.

Sampling the Cellular Signaling State: Acquiring Cellular Signaling State Distributions

Measuring the signaling state, or the level of activation of a specific molecule in a signal transduction pathway, at the single-cell level based on fluorescent biosensors as described above requires quantifying the fluorescent levels at single-cell resolution. Typically, flow cytometry or fluorescence microscopy approaches are utilized to measure cellular signaling states. Although fluorescent microscopy approaches enable live-cell imaging to fully capture signaling state dynamics, measuring multiple readouts simultaneously remains limited, as discussed above. On the other hand, flow cytometry methods are only able to measure cellular signaling states at a single time point, but are capable of measuring multiple readouts simultaneously. Specifically, maturation of fluorescent flow cytometry methodology has made previously highly challenging and demanding experiments, such as the simultaneous measurement of >10 color channels, more commonplace. In addition, developments in readout technology substantially increases the multiplexing capacity. For example, mass cytometry combines time-of-flight mass spectroscopy with the readout of a flow cytometer. Specifically, single-cells are captured and the concentration of isotopically pure rare metals conjugated to antibodies [34] and nucleic acid probes [35] are measured. Mass cytometry pushes the boundaries of multiplex measurements and can now concurrently measure >40 channels in a single-cell. The wealth of information produced by mass cytometry methods has already made important contributions to understanding the distribution of single-cell responses [36–38].

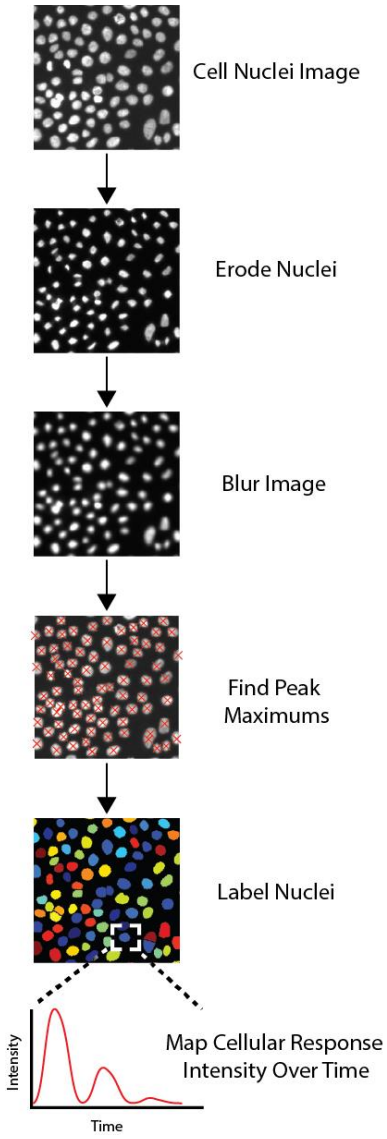

Figure 0.3. Cellular Segmentation Analysis. Cellular segmentation separates cells from each other and the background of the image. A raw image of the cells (here an image of nuclei stained with Hoeschst is shown) undergoes a sequential process to eventually create a label for each cell. A series of images showing the response can be mapped to this cell label to create a cell response time series.

Unlike cytometry, advances in fluorescent microscopy are not focused towards measuring throughput or increasing multiplexing capacity. Rather, recent developments focus on increasing resolution by utilizing super-resolution approaches. Therefore, hardware used

for high-content imaging systems has not significantly changed in recent years. Instead, improvements in software allow better measurements. Developing better analysis software is important since interpreting and quantifying microscopy images is a non-trivial process. Existing microscopes effectively allow image acquisition at rates of a few images per second. Therefore, a standard multi-well overnight acquisition can generate >100,000 images. Manual analysis of these large datasets is practically impossible. Moving from manual to automated image analysis to properly and efficiently identify cells, track cells, and measure changes in biosensor state over time requires computer vision and sophisticated algorithms (Figure 3). The majority of computational image analysis approaches for high-content screening (HCS) follow a similar workflow [39]. In the first step, called segmentation, cells are identified in the image and distinguished from each other and from regions without cells (Figure 3). Subcellular structures and organelles can also be segmented and associated with their parent cell. In live-cell time-lapse microscopy, tracking cells over the entire sequence of acquisitions is a critical step to obtain a cellular response time-series at single-cell resolution. Additionally, quantifying the phenotypic states of cells, i.e. cellular shape, size, microenvironment, etc, is necessary to better understand heterogeneity between single-cells [40–45]. A large number of cellular segmentation and tracking algorithms have been developed and are available in commercial and open source software packages [46–49].

Sampling Cellular State Space: Challenges in Quantifying the Distribution of Cellular Behavior

While catchy, the phrase “single-cell analysis” is misleading to a degree. Single-cell analysis does not aim to understand the behavior of a particular individual cell. Rather, single-cell analysis aims to understand population behavior by analyzing single-cell distributions.

New statistical tools enable the analysis of complex cellular state distributions which enable deeper insights into underlying biology.

Single-cell statistical analysis methods are needed to interpret increasingly complex biological data. Many single-cell datasets not only characterize biological responses at a single-cell resolution, each cellular response is measured at a multivariate level resulting in highly complex datasets. Increasing data complexity makes gaining even an initial intuition of raw data prior to analysis difficult. For example, a typical mass cytometry dataset generates a data matrix of ten thousand rows and thirty-eight columns. Understanding and properly interpreting such a large dataset is non-trivial. To address this complexity a large array of statistical analysis methods have been developed to simplify complex data in a manner that attempts to capture the relationships between cells. This technique, often called dimensionality reduction, is used in the initial stages of data analysis to identify natural groupings between data types(e.g. types of genes). Groupings with similar relationships provide a simplified representation of complex high-dimensional data. A challenge with dimensionality reduction is that the interpretation of the simplified representation is often not obvious. Proper interpretation of the simplified data requires understanding what assumptions were made to simplify the dataset. Techniques like principal component analysis identify a less complex and lower dimensional representation of the data that preserves most of the variance. On the other hand, techniques like isomap, t-SNE and its variants such as viSNE preserve local relationships between neighboring cells [50–52]. In the case of the mass cytometry dataset mentioned above, t-SNE transforms the data matrix from ten thousand by thirty-eight into a simplified matrix of ten thousand by two. This simplification maintains single-cell information while combining information from several distinct readouts (e.g. columns) into two quantities that can be plotted against each other in a standard scatter plot.

The suitability of dimensionality reduction methods continues to expand as single-cell datasets become richer and more complex. However, it is important to note that such methods are a visual aid to initially interpret intricate data and does not provide quantitative information. Quantitative analysis of single-cell data that does not depend on an initial simplified interpretation requires computational tools that provide meaningful statistics summarizing single-cell response distributions. Fortunately, a large array of existing data analysis methods combined with freshly developed quantification methods is able to accomplish these tasks. One example of the adoption of such methods is the growing usage of information theory in the analysis of variability in signal transduction. Information theory has powerful techniques to measure relationships between random variables [53]. New developments and tools in information theory enable better insights into complex and highly variable cellular responses [6,37,54].

Computational Modeling: Confirm & Predict

The American psychologist Kurt Lewin famously said "There is nothing as practical as a good theory." [55]. Traditionally, biological sciences have not been as receptive to mathematical modeling as other disciplines such as engineering, physics, and chemistry. A major contributing factor is the difficulty of integrating biological data with mathematical models. Even with a physiologically sound mathematical model, it is difficult to measure or estimate kinetic parameters that produce useful predictions. Despite these challenges, there have been significant advancements in modeling several major signal transduction pathways.

Pioneering works in several important canonical signaling pathways such as calcium, NF-kB and MAPK utilized mathematical modeling to gain biological insights not available

using experiments alone. Calcium signaling pathways regulate a multitude of biological process such as transcription, cell motility, and muscle contraction through diverse cellular response patterns [56]. Various mathematical models have been proposed to explain the oscillatory behavior of cellular calcium response. For example, models proposed by De Young & Keizer and Dupont & Erneux rely on the biochemical properties of IP3 channels to explain calcium induced calcium release [57,58]. Other models consider ryanodine receptor and voltage-gated channels to explain this phenomenon [59,60]. In addition to models describing cellular calcium oscillations, there are numerous models describing calcium spikes in non-excitable cells by incorporating surface receptor signaling and receptor desensitization parameters [61,62]. The NF-κB pathway provides an additional important example of the utility of mathematical modeling. Initial work by Hoffmann et al. provided a comprehensive mathematical model of the IκB-NF-κB signaling module [63]. Hoffmann et al successfully accounted for the population level temporal behavior of NF-κB in the EMSA data using their model. A classic study by Huang & Ferrell on the MAPK pathway predicted that the MAPK signaling cascade would produce a steep dose response curve, allowing cells to switch from one state to another [64]. This prediction was subsequently supported by experiments.

Cellular heterogeneity measurements, as indicated by single-cell datasets, motivate the use of mathematical models to uncover the underlying causes of cellular heterogeneity based on the mechanistic details of the signaling pathway. Albeck et al. and Spencer et al. utilized computational modeling to explain the heterogeneous apoptosis behavior in the TRAIL pathway [65–67]. By changing the rate parameters downstream of the TRAIL receptor or the protein concentration levels in the mathematical model, heterogeneity in timing delays to apoptosis can be accounted for in the simulated data. In another study concerning the TRAIL pathway, Eissing et al. used a properly reduced model to perform a bistability analysis to

deduce the diverging behaviors in the TRAIL pathway [68]. Nelson et al. used computational modeling in conjunction with single-cell NF-κB measurements to demonstrate how varying transcriptional activity of IκBα can alter the NF-κB oscillation frequency [69]. Lee et al. parameterized a dynamic model of NF-κB induced transcription using a combination of single-cell nuclear NF-κB measurements and transcript numbers in the same single-cells [70]. From their model they were able to determine how cells can detect a fold-change in NF-κB levels as opposed to absolute concentrations to induce transcription. Nonlinear systems analysis techniques, such as bifurcation analysis, were employed by Koenigsberger et al. to model calcium oscillations to study the mechanisms for smooth muscle cells to synchronize their oscillations [71].

Mathematical modeling is a useful tool to gain useful biological insights at the single-cell level. Feedback properties of signaling pathways can also be exploited to study the underlying causes of cell-to-cell variability. Birtwistle et al. observed bimodal behavior in the MAPK/ERK cascade which produces two populations of ppERK output in response to EGF stimulation [72]. By inspecting the negative feedback loop structure in the mathematical model of the pathway and performing computational simulations, they deduced that the heterogeneity in RasGTP levels coupled with varying ERK activation threshold levels eventually produced bimodal behavior in the cell population. Ferrell et al. studied the progesterone stimulation of the MAPK pathway leading to oocyte maturation [73]. While the population average data conveyed a graded response, single-cell data revealed an all-or-none response. Analysis of the mathematical model of the pathway showed that bistability and positive feedback within the pathway provided the switch for cell fate decision making in the cell. Using single-cell microfluidic perturbations in combination with data-driven clustering of dynamic ERK profiles, Ryu et al were able to construct an updated MAPK model to determine

differences in cellular fate decision making [74]. Ultimately they were able to use their mathematical model to determine how cellular fate decisions can be rewired with different growth factors. Feinerman et al. studied T-cell receptor signaling using both single-cell data and mathematical modeling [75]. They investigated how variation in signaling proteins changes cellular responsiveness. Interestingly, the co-receptor and negative feedback loop of SHP-1 together regulate the activation threshold and the switch behavior of the cell's responsiveness to regulate the diversity of cellular phenotypes. A number of other models based on single-cell datasets have been developed for a variety of signaling systems [76,77].

In addition to moving from population level to single-cell level analysis, there has also been an increasing focus on adapting modeling approaches to account for biological noise and model parameter uncertainty. Elowitz et al. succinctly described intrinsic biological noise, the stochastic thermal fluctuation internal to the system, and extrinsic biological noise, the fluctuation external to the system of interest and is deterministic within the same cell but different among cells [78]. Others in the biological modeling community such as Janes & Lauffenburger and Gutenkunst et al. have indicated that the structure of a model is more important than the individual kinetic parameters when making predictions because multiple sets of kinetic parameters can fit a model equally well [79,80]. This implies that assigning distributions of parameter values to the model will increase single-cell model predictability (Figure 4). Tay et al. described the level of NF-κB and TNFR-1 using lognormal parameter distributions in order to account for extrinsic noise between cells [4]. Cheng et al. applied probabilistic based mathematical modeling to the TRIF pathway [81]. They modeled four key parameters in the areas of TLR4 synthesis, MyD88 activation, TRIF activation, and endosome

maturation as probability distributions rather than as fixed values. The simulated signaling pathways generated similar heterogeneous behaviors as found in the experimental data. Eydgahi et al. used Bayesian and Monte Carlo methods and calibrated a mathematical model of apoptosis single-cell data to obtain probability distributions for all kinetic parameters in the model [82]. This approach allowed for discrimination between competing mathematical models of apoptosis.

Overall, the methods discussed above made specific assumptions regarding the shapes of the distributions of certain kinetic parameters. A possible alternative approach is to fit the individual cell trajectories to the mathematical model using Bayesian sampling methods such that each cellular trajectory will have a set of parameter distributions. A potential advantage of using direct Bayesian sampling is that it assumes little concerning the form of parametric distributions that could potentially have complex structure not initially assumed by researchers.

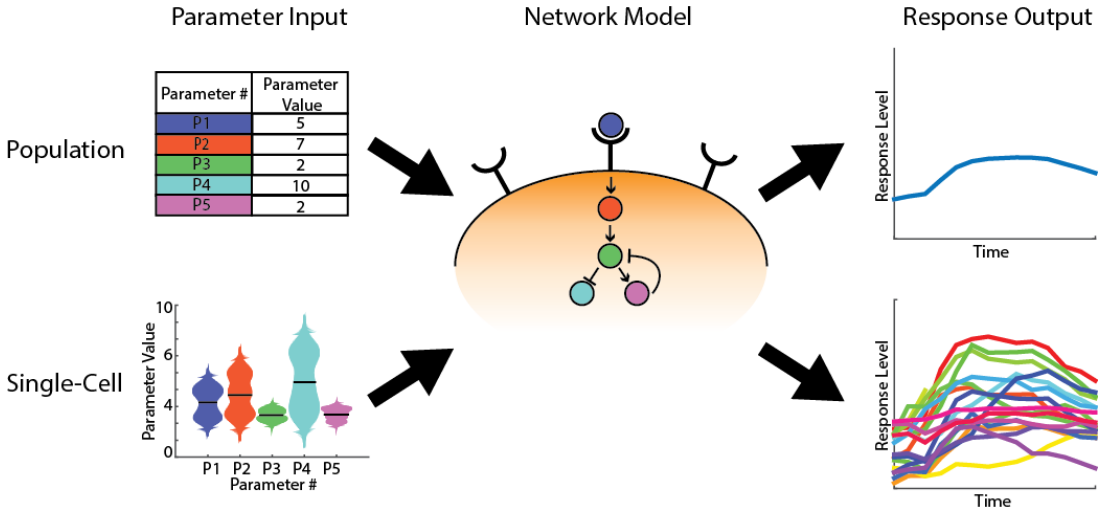

Figure 0.4. Population vs Single-Cell Computational Model Parameterization. Although a network model between population and single-cell level models remains the same, differences in parameter selection and distribution elicit different response outputs. Population level parameters have a single value per parameter whereas single-cell level parameters consist of a range of values. Population level parameters provide a single response output that represents that entire population of cells whereas single-cell level parameters show the distribution of responses within the population.

Manipulate: Biological Insights through Internal and External Manipulation

Experimentally investigating a cellular signaling system involves either changing the outside or the inside of a cell. The outside is perturbed by changing the cellular environment by either adding or removing a specific factor. Similarly, the inside of a cell can be changed by over expressing or removing specific genes of interest. Although the concept behind experimental manipulation does not change with single-cell techniques, the specific techniques used to manipulate cells has evolved.

Microfluidics: Environmental Changes at a Micro Scale

The application of microfluidics to biological research has powerful implications for single-cell signal transduction measurements. Microfluidics enables the researcher to manipulate fluids with a high level of control at the submilliliter scale. This high level of control permits spatial and temporal manipulation of the cellular environment. The ability to customize a microfluidic chip to the specific needs of an experiment removes previous limitations set by currently available tissue culture technology. The complexity of a microfluidic chip depends on the specific biological question. Complexity ranges from very simple to extremely complicated depending on the biological phenomena in question (Figure 5). The increased usage of microfluidic devices in biological research over the past two decades has been extensively reviewed elsewhere [83–86]. Here we discuss the spatial and temporal benefits of microfluidics devices that range from very simple to highly complex.

Figure 0.5. Complexity of Microfluidic Chip Design Depends on Desired Experimental Output. Simple microfluidic designs (left) do not equate to less information in comparison to complicated designs (right). Rather, the complication level of each design depends on the required information from the experiment whether it be spatio-temporal dynamics of wound response (left) or cellular response to dynamic, temporal inputs (right, image courtesy of Savas Tay at the Institute for Molecular Engineering at the University of Chicago).

Temporal modulation allows researchers to control the duration and frequency of changes to the cellular environment. Environmental changes include modifications to growth media conditions or stimulating cells via a perturbation of interest. No longer are researchers limited to population level bolus additions of stimulus at a single time point. In the Suel lab, media conditions are manipulated to determine the specific growth mechanisms of biofilms [87,88]. Here, Prindle et al. use an unconventionally large microfluidic design to observe the growth of a biofilm [87]. Although there are only two ports allowing media to flow in and out of the cell chamber, they were still able to add and remove specific components of the media to determine factors necessary to biofilm growth. Another simple design by Herson et al measures the signaling pathway response over varying input frequencies [89]. In order to ensure rapid media changes with distinct period times, Herson et al employ a "Y" design where each arm of the Y is connected to a different media solution. The simplicity of these designs enables easier manufacture and implementation of the design. However, they are limited in throughput and can only change between two different inputs. On the other end of the spectrum, the Tay lab uses a complex microfluidic design that is able to precisely vary the

duration and dose of the stimulus at a high throughput level to determine how cellular outputs are influenced by dynamic inputs [90–92]. However, the complicated design requires higher technical expertise.

In addition to temporal stimulation, microfluidic device designs also allow for spatial modulation. Spatial modulation is important in cases where gradient information is important such as in wound healing or chemotaxis. Spatial perturbations are possible using microfluidic devices due to the low Reynold's number characteristic of microfluidics devices. This property ensures that any gradient formation and mixing is due to diffusion rather than convection within the device. Handly et al. take advantage of this property to study paracrine communication of the initial wound response using a simple two-layer microfluidic design [93]. On the bottom is a cell chamber and the top an air layer. The ceiling of the cell chamber contains a pillar such that when air pressure is increased in the air layer the pillar lowers down onto the cells to mechanically wound the cells. The lack of convection within the device ensures that any molecules released into the extracellular environment move between cells according to diffusive principles rather than flow through the device. Chen et al. employ a more complicated design to study the migration of heterogeneous tumor cells at the single-cell level [94]. Their device design involves capturing single cells in narrow capillaries and applying a gradient across the capillary to mimic concentration gradients of chemokines that induce tumor cell migration. The formation of this gradient directly takes advantage of even-mixing facilitated by diffusion in microfluidic devices. The geometry of these capillaries also imitates the shape of blood and lymphatic capillaries to provide a more physiologically relevant study of tumor cell migration. Again, although each device design probes a spatially relevant biological question, the degree of device complexity is determined by the specific needs of the experiment.

Optogenetics- Intracellular Manipulation through Extracellular Stimulus

Advancements in optogenetics have opened up the possibility to expand spatio-temporal stimuli to intracellular signaling states. Traditional cellular manipulation involves perturbing the entire population of cells through genetic or pharmacological manipulations. However, these types of irreversible population level changes do not allow for selective spatial activation and dynamic temporal inputs which are important in testing hypotheses related to cellular communication. Optogenetic approaches use light to perturb genetically manipulated

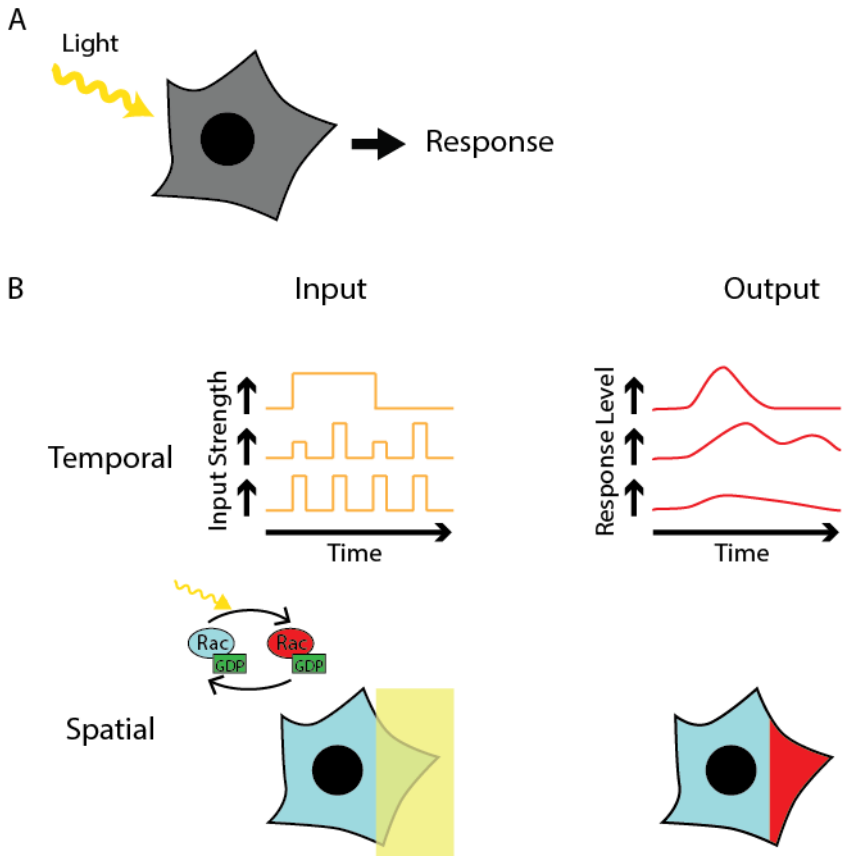

Figure 0.6. Optogenetics enables controlled spatial and temporal inputs. A. Genetically manipulated cells are perturbed by light to elicit a response. B. Cells can be manipulated with light both temporally and spatially using optogenetics. Dynamic light inputs can generate varying cellular response outputs (temporal). Optogenetic control of specific signaling molecules, such as the GTPase Rac, enables precise spatial control over which area of the cell is activated (spatial).

cells and can do so in a spatial and temporal manner to investigate cellular signal transduction (Figure 6).

Although initial applications of optogenetics focused on neurobiology, the ability to regulate intracellular signaling pathways in a spatio-temporal manner using photoactivatable proteins has made optogenetics a functional tool to study signal transduction. The application of light-activated proteins varies from conformational changes to uncaging. However, the basic ability to perturb an intracellular signaling pathway with high spatio-temporal resolution remains the same. Toettcher et al. developed optogenetic tools able to activate isolated signaling nodes within the cell to determine how different temporal inputs regulate downstream responses [95]. Using a photoactivatable Ras protein, they measure how the dose and frequency of Ras activation determines downstream ERK response. The kinetics of the Raf/MEK/ERK pathway were also investigated using optogenetics by Zhang et al [96]. Using temporal activation patterns they were able to induce PC12 cell differentiation similarly to NGF stimulation.

Optogenetics also enables precise spatial manipulation of cells, either at the subcellular or multicellular level. This type of stimulation is important when examining specific proteins required for cellular behavior or determining how gradient formation determines cellular response. Wu et al. utilize a photoactivatable Rac to produce cell protrusions and ruffling at specific subcellular locations to control the direction of cellular motility [97]. The Gautam group developed an optogenetic method to spatially manipulate GPCRs at a subcellular level to create gradients of GPCR activation within the cell [98,99]. By forming gradients of GPCR activation within cells they were able to control the movement of the immune cell. At the multicellular level, optogenetics enables experiments where only a specific portion of cells are stimulated to determine how the surrounding cells respond to the

stimulated cells. Wang et al. demonstrate this principle by activating Rac using light in a single cell within a cluster of border cells in Drosophila [100]. Although only a single cell was activated, communication between cells caused the other cells within the cluster to move according to the activation level of the initial cell. The ability to precisely localize activation in a group of cells has exciting potential in the realm of cellular signaling. These types of experiments are useful when considering gradient formation across a tissue during embryonic development, wound healing, in addition to cellular migration.

Combining the spatiotemporal control of optogenetics with the genome editing abilities of CRISPR-Cas-9 has exciting potential in the study of signal transduction at the single-cell level. At the fundamental level, genome editing using CRISPR-Cas9 is effective in population level studies. However, advancements in light-inducible CRISPR-Cas9 systems [101–103] enables researchers to make specific edits to the genome with high spatiotemporal control. Combining optogenetics with CRISPR-Cas9 enables temporal activation of specific genes to study biological outputs as well as activation of specific genes in localized regions. The development of more optogenetic systems that utilize CRISPR-Cas9 will provide an exciting set of tools in the study of single-cell signal transduction.

Combining Single-Cell Manipulation Methods for Effective Study of Signal Transduction

Using microfluidics, optogenetics, and CRISPR-Cas9 allows for controlled manipulation of both the intra- and extracellular environment. Although advances are being made to combine these technologies, such as with the photo-inducible CRISPR-Cas9 systems mentioned above [101–103], studies that fully integrate all three technologies is difficult. A combination of these three approaches has powerful abilities in controlling the spatial and temporal manipulation of cellular environment and function. As these technologies mature and become commercially available it will increase the adaptation of systems biology approaches

to study signal transduction. For example, user friendly microfluidic designs or commercially available microfluidic-like devices expand single-cell study beyond traditional cell culture tools. Additionally, increasing usage of CRISPR-Cas9 and optogenetic technologies will expand the available selection of target genes and signaling systems.

Outlooks

Approaches to study signal transduction networks at the single-cell level are in a renaissance period. The ability to observe, manipulate, and model biological systems using constantly advancing single-cell techniques drives new discoveries and enables deeper insights into the inner working of cells. As cellular dynamics and heterogeneity are key aspects to understanding signaling pathways, the adoption of single-cell approaches is critical for future progress. One of the key challenges that limits the adoption of these approaches is technical. Single-cell studies require tools from engineering, biology, and computer science. Unfortunately, these three disciplines are not well integrated in traditional curriculum. However, this is changing with increasing numbers of undergraduate and graduate programs emphasizing the importance of quantitative training.

Here we outlined recent advances pivotal towards progress in understanding the dynamic nature of signaling networks at a single-cell resolution. In parallel, other single-cell technologies that can probe the internal state of the cells have made tremendous progress. Omics technologies, including both “molecular profiling” and “molecular perturbations” [104] provide rich datasets useful with many benefits over currently available microscopy methods. Omics technologies have the ability to examine thousands of genes, proteins, and post-translational modifications at one time whereas microscope technologies are limited in the number of nodes within a network they are able to monitor concurrently. We anticipate that integrating single-cell approaches within signal transduction, such as measuring dynamic

single-cell signaling responses, with OMICs single-cell approaches, such as RNAseq, will play a major role in future work concerning signaling networks.

Signal transduction studies at the single-cell level provide information about the dynamic nature of biological signaling networks. Although these approaches follow the same scientific methodology of hypothesis, experiment, analysis, and conclusion, the specific approaches to decipher the intricacies of single-cell variability differ. Advancements in these technologies have come a long way to make answers to biological questions at the single-cell level possible. Future advancements of single-cell approaches and integration with other technologies shows promise for exciting developments in understanding biological network dynamics.

Acknowledgments

The work was supported by NIH grants GM111404 and EY024960.

The introduction, in full, is a reprint of the material as it appears in Handly, L.N.; Yao, J.; Wollman, R. Signal Transduction at the Single-Cell Level: Approaches to Study the Dynamic Nature of Signaling Networks. J. Mol. Biol. 2016, 428, 3669-3682. The dissertation author is the first author on this paper.

CHAPTER 1

Paracrine communication maximizes cellular response fidelity in wound signaling

Abstract

Population averaging due to paracrine communication can arbitrarily reduce cellular response variability. Yet, variability is ubiquitously observed, suggesting limits to paracrine averaging. It remains unclear whether and how biological systems may be affected by such limits of paracrine signaling. To address this question, we quantify the signal and noise of Ca^{2+} and ERK spatial gradients in response to an in vitro wound within a novel microfluidics-based device. We find that while paracrine communication reduces gradient noise, it also reduces the gradient magnitude. Accordingly we predict the existence of a maximum gradient signal to noise ratio. Direct in vitro measurement of paracrine communication verifies these predictions and reveals that cells utilize optimal levels of paracrine signaling to maximize the accuracy of gradient-based positional information. Our results demonstrate the limits of population averaging and show the inherent tradeoff in utilizing paracrine communication to regulate cellular response fidelity.

Introduction

Cellular variability is likely a biological trait with significant phenotypic consequences. Technological advances in single-cell measurement methodologies reveal substantial cellular variability. For instance, single-cell quantification of protein concentration variability between cells shows that the concentration of many signaling molecules can vary by ~25% (coefficient of variation) [67,105,106]. Furthermore, a large and rapidly growing body of single-cell

transcriptomics experiments further demonstrates that cells homogeneous in “type” have substantially heterogeneous gene expression patterns [107].The origin of this cellular variability has been traced to fundamental properties of gene expression. Notably, single-molecule kinetics regulates gene expression and, as a result, is an inherently stochastic process [108].

While the costs and benefits of cellular variability are likely dependent on the specific physiological context, the functional significance of cellular variability suggests that cellular variability magnitude is regulated. Functional analysis of cellular response variability demonstrates that the observed cellular variability affects the core function of signaling networks. Despite a homogenous environment, cells respond in a heterogeneous manner due to biological variability. Response variability potentially degrades transmitted information and decreases downstream effector ability to reliably respond to environmental changes [5,109–111]. The abundance of cellular variability throughout biological processes and the potential consequences of information degradation suggest that biological systems have developed mechanisms to regulate cellular variability. However, cellular variability is not necessarily detrimental to cellular function. In fact, cellular heterogeneity often plays a critical role in ensuring proper cellular response by mechanistically increasing the cellular response range to a constantly changing environment [112]. For example, single-cell noise in NFκB dynamics creates robust population level responses to a wider range of inputs [113,114].

Cells share information with each other via paracrine signaling, which effectively averages variable cellular responses and therefore reduces cellular variability. Overall population-level averaging decreases variability by following the statistical laws of the central limit theorem and the law of large numbers [115]. Paracrine signaling averaging can decrease variability in a similar manner, but functions on a local population level. Specifically,

paracrine signaling averaging functions such that the local concentration of the paracrine ligand, or the concentration of ligand a cell is exposed to, is the average ligand concentration secreted by local cells (Figure 1A). Indeed, the benefits from paracrine communication were previously demonstrated to increase post-paracrine cellular response fidelity [116,117]. The process of local population "information averaging" by each cell enables increased accuracy of inherently single cell decisions such as proliferation and differentiation.

Despite promises of noise mitigation from paracrine averaging, parameters set by biological systems can limit these potential benefits. For example, population averaging due to paracrine communication may cause loss of information in a similar manner to the information loss of single-cell dynamics due to "population average" bulk measurements [78,106,118]. The potential information loss due to "over-averaging" of variable single-cell responses demonstrates a limitation to paracrine communication. Limitations to paracrine communication are also observed in post-paracrine single-cell responses that remain highly variable despite paracrine averaging. These limitations suggest an overall functional constraint to the potential benefits of paracrine communication. However, the identity and source of these limitations on paracrine communication benefits are unknown.

The initial paracrine signaling pathways that are activated in response to Damage Associated Molecular Patterns (DAMPs) are a good model system for investigating the influence and limits of paracrine communication on cellular response fidelity. Paracrine communication is pervasive during initial wound response. Wound healing begins as soon as the wound occurs and the initial cellular wound response provides the foundation for proper downstream healing. The initial cellular wound response relies on external environmental cues as well as programs inherent to the cell, including DAMPs as primary danger signals [119]. DAMPs are released from necrotic cells and bind to extracellular receptors on surrounding

cells. This binding initiates a signal in the surrounding cells to secrete a secondary set of cytokines and growth factors required to coordinate the wound healing process. Many DAMP signals, such as extracellular ATP, are transient and released in limited quantities. As a result, the initial wound response to such DAMPs shows high cellular variability and low fidelity. Despite the limited fidelity of the initial wound response, the wounded epithelium is able to establish a robust healing response. The complicated and multi-step wound healing process utilizes several paracrine communication mechanisms to share cellular information and coordinate the overall healing program.

Here we use the paracrine release of epidermal growth factor (EGF) ligands initiated by ATP binding to P2Y receptors as a model to investigate the limits of cellular information sharing through paracrine communication to mitigate biochemical noise (Figure 1A). We show that paracrine communication increases extracellular signal-regulated kinase (ERK) response fidelity using live single-cell quantitative fluorescent imaging of primary Ca^{2+} and secondary ERK responses downstream of P2YR and EGFR, respectively. Statistical analysis of the primary response signal-to-noise ratio (SNR) demonstrates that the increase in response fidelity is limited by paracrine communication distance (PCD). To analyze this pathway in the physiological context of wound response we developed a new microfluidics device to monitor the spatial propagation of initial wound response signaling. Our results demonstrate that the interplay between the wound induced spatial signaling gradient and the cellular noise pattern produces an optimal PCD. The optimal PCD balances the benefits of decreased noise from local averaging with the cost of reduced signal of the spatial signaling gradient due to over-averaging. Empirical measurements of the PCD reveal that cellular communication occurs at a distance to maximize cellular response fidelity.

Results

Paracrine signaling reduces response variability

Here we establish that the paracrine activation of ERK by ATP provides a suitable system to investigate signaling response fidelity changes due to paracrine communication. Extracellular ATP binding to P2YR results in EGF family ligand release to bind EGFR and activate ERK response as monitored by ERK activity following ATP addition. In the mammary epithelial cell line MCF-10A, addition of extracellular ATP increases ERK kinase activity in an EGFR dependent manner (Figure 1B) similar to results reported in other in vitro epithelial models [120]. ERK, as measured by the genetically encoded FRET sensor EKAREV [30,31], increases when stimulated with ATP. Inhibiting EGFR with tryphostin AG1478

prevents ERK activation upon ATP addition showing that ERK activation depends on secreted EGF binding to EGFR. [121].

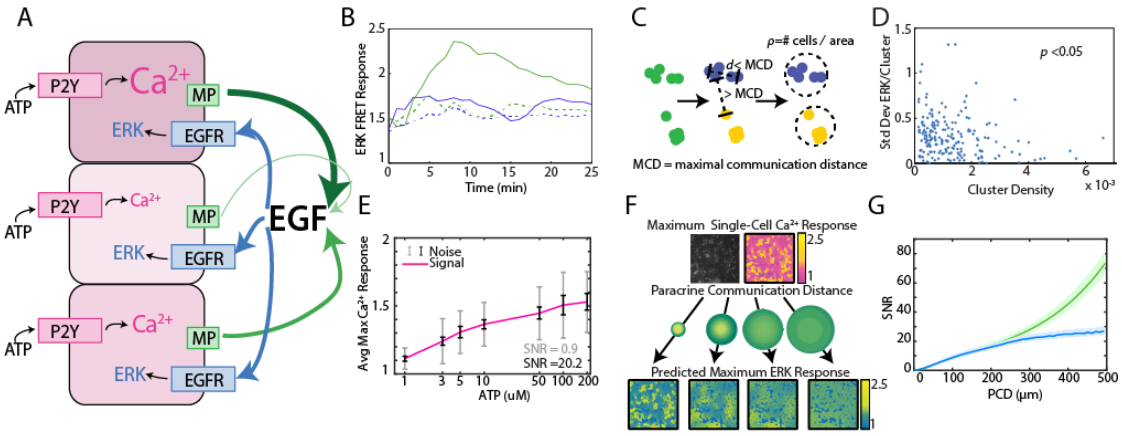

Figure 1.1. Local averaging using paracrine signaling reduces response variability in a communication distance dependent manner. A. A hypothesis for local averaging based reduction of response variability using paracrine signaling for ERK activation by P2Y receptors. ATP binds to P2Y receptors to increase cytosolic Ca^{2+} levels with high variability between cells despite equivalent ATP dosage per cell (pink shading). EGF release from each cell is proportional to the primary response to ATP (green arrows). Due to diffusion of EGF, the local concentration will be the average of EGF released from nearby cells and subject cells in a local neighborhood to the same level of EGF (blue arrows) to result in similar ERK activation. B. ATP activates ERK in a paracrine fashion in MCF-10A cells. ERK response to 10μM ATP addition with (green dashed) and without (green solid) 1μM of EGFR inhibitor tryphosphitin AG1478. 0μM ATP addition with (blue dashed) and without (blue solid) 1μM AG1478 shown as controls. C. MCF-10A cells were clustered based on their spatial proximity so that cells within a cluster were within a specific maximal communication distance (MCD) and cells in other clusters were farther than the MCD. Cluster denisty was calcuated by dividing the number of cells per cluster by the circular area inhabitated by each cluster. D. Standard deviation of ERK response per cluster to 10μM ATP. Standard deviation decreases with increasing cluster density (p-value<0.05, Pearson correlation). E. Average maximum Ca^{2+} response with increasing ATP dosage. The standard deviation, i.e. noise, of the Ca^{2+} response to each ATP dosage is large when compared to the increase in average response with increasing ATP dose, i.e. signal (SNR=0.9, gray error bars (standard deviation)). Noise decreases when Ca^{2+} response is locally averaged with a PCD of 100μm (SNR=20.2, black error bars (standard deviation)). x-axis shown in log-scale. F. Single-cell maximum Ca^{2+} response is locally averaged across an area specified by the PCD to produce a predicted single-cell ERK response. Variability between cells in the predicted ERK response decreases with increasing PCD. Response magnitude of Ca^{2+} and ERK response indicated by pink to yellow and blue to yellow colorbars, respectively. G. The SNR of the predicted ERK response from locally averaged Ca^{2+} data continually increases with increasing PCD shown for a model with rapid diffusion (green) or limited by the diffusion rates and integration time of paracrine signals (blue, Material and Methods). SNR calculated in same manner as panel E with increasing PCD. Shaded area is SEM (N=5).

With our paracrine communication system established, we next confirmed the influence of paracrine communication on cellular response variability. Under conditions of low cell density we used a spatial clustering analysis to group cells such that the distance between groups effectively constrained communication to cells within groups (Figure 1C, D, Supplemental Figure S1-S2). In the case that cellular coordination is beneficial, we anticipated that the ERK response within groups of higher cellular density, i.e. cells have increased communication ability, would have reduced response variability than cell clusters with decreased communication ability. ERK response variability within clusters decreases with increasing cluster density indicating increased intercellular communication ability. Increased intercellular communication ability is not observed in the absence of paracrine communication such as with the primary Ca^{2+} response to ATP (Figure 1D, Supplemental Figure S2). Furthermore, disrupting paracrine communication by partially inhibiting Src results in the loss of the observed benefit of paracrine communication in higher density clusters (Figure 1D, Supplemental Figure S3-S4). Together these observations support the hypothesis that paracrine communication decreases cellular variability by increasing cellular coordination.

Computational analysis of variability reduction resulting from paracrine information sharing

Next we developed a computational model that mimics the coordination-effects of paracrine communication (see methods for details). This computational model quantifies the overall observed benefit of paracrine coordination and predicts the potential reduction in variability. Experimental single-cell dose response data of primary Ca^{2+} (prior to paracrine communication) response to ATP is used as an input to predict the secondary ERK response. We quantify cellular response fidelity by using a simple signal-to-noise analysis (SNR). In this analysis the cellular response magnitude of the input ligand (signal) is divided by the cellular response variability (noise). The signal is estimated by calculating the spread between the

average cellular Ca^{2+} responses from multiple ATP concentrations using multi-well dose response data. Noise is calculated from the average variability between cellular responses to a single input ligand concentration. SNR is simply the ratio of these two estimates (Figure 1E). To mimic the benefit of paracrine communication our computational model performs a local, spatially weighted average (convolution) of the primary Ca^{2+} response to predict the variability of response post paracrine communication (ERK) (Figure 1F). In short, the convolution averages the signal for every cell with its associated surrounding cells by weighting the surrounding cells based on a Gaussian function parameterized with varying PCDs. The PCD represents how far the paracrine molecule travels from a single-cell to activate its associated surrounding cells. Local spatial averaging provides an upper bound of the possible benefit resulting from cellular communication in conditions where no additional noise exists in the paracrine pathway. This analysis indicates that paracrine averaging using a PCD of 100μm increases response SNR from 0.9 to 20.2 by decreasing noise, or response variability, of the predicted ERK response (Figure 1E, gray/black). To investigate the limits of paracrine averaging, we repeated this analysis for multiple PCDs. Interestingly, our analysis estimates that the overall response SNR can increase up to 80-fold at PCDs of 500μm when paracrine diffusion is not limiting, and up to 25-fold when diffusion of the paracrine ligand is limiting (Figure 1G). More sophisticated statistical measures, such as mutual information, produce similar results (Figure 1G, Supplemental Figure S5). The large maximal SNR benefit suggests a potentially noise-free ERK response. However, experimental measurements of ERK response fidelity shows substantial ERK variability indicating potential factors that limit the benefit gained from paracrine communication (data not shown).

Cellular response fidelity depends on the extent of paracrine signaling during wound response

Extracellular ATP released from necrotic cells act as DAMPs to activate healthy cells proximal to the wound [122]. Given this role, the spatial component produced by the ATP concentration gradient and the resulting cellular positional information relative to the wound may be important in the analysis of paracrine communication that occurs over hundreds of microns from the wound. Our previous SNR analysis demonstrating an increasing SNR with increasing communication distance was done based on multi-well experiment data. However, the bolus addition of ATP creates a spatially uniform ligand concentration in the well and does not represent a physiologically relevant spatial component. To examine whether ATP spatial patterns influence the paracrine communication benefit we repeated the SNR analysis using single-cell wound response data.

In order to measure the spatial wound response for epithelial cells, we first developed a convection-free, small-volume wounding device. Scratch-assays, where a monolayer of cells is mechanically wounded using a pipet tip, are traditionally used for epithelial cell wounding [123]. Although the scratch-assay is useful for studying cell-migration following wounding, scratch-assays lack the ability to study paracrine signaling. The large volume above the cells and convection caused by the scratch present challenges to examine paracrine signaling due to the dilution and inadvertent mixing of any paracrine molecules released from a cell into the surrounding media. To circumvent these technical issues we developed a microfluidics based wounding device (Figure 2A, B). Our device has two components: an air channel (black) and a cell chamber with a ~ 2.5μL volume (orange). The ceiling of the cell chamber has a PDMS pillar that, when air pressure is increased in the upper air channel, lowers down on to the cells, thereby wounding the cells in the cell chamber in a highly controlled and reproducible manner (Figure 2B, C, Supplemental Figure S10, Movie 1).

We used our wounding device to monitor Ca^{2+} and ERK response to a 300μm diameter wound using a stable, dual reporter MCF-10A cell line expressing the genetically encoded Ca^{2+} indicator RGECO [124,125] and the EKAREV FRET reporter for ERK [30,31] (Figure 2D, E—Video 2). We verified the key role of ATP in initial wound response by wounding in the presence of apyrase, an enzyme that rapidly hydrolyzes ATP. Wounding in the presence of apyrase inhibits both Ca^{2+} and ERK response (Figure 2D, E, insets). From each wound we quantified single-cell time traces for over 3000 cells. Notably, the maximum activity per cell shows a larger response in cells closer to the wound compared to cells farther away from the wound for both Ca^{2+} and ERK. These response gradients demonstrate the importance of the cellular position to determine the cellular response, or positional information (Figure 2D, E). We used coefficient of variation (CV) to measure the variability of the post-paracrine ERK response and the pre-paracrine Ca^{2+} response in the wound (Figure 2F). Indeed, the CV for Ca^{2+} wound response shows statistically higher variability than ERK wound response indicating that paracrine communication reduces response variability during initial wound response.

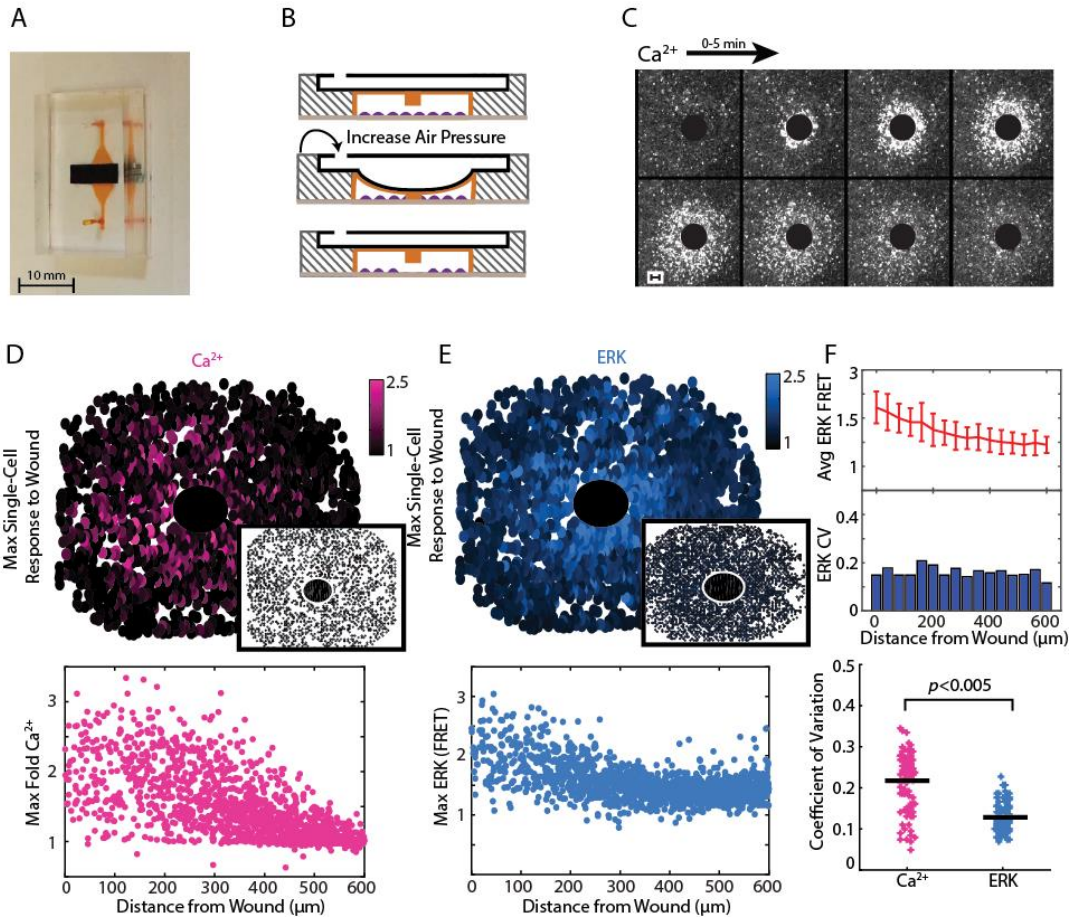

Figure 1.2. Paracrine communication reduces response variability during wounding. A. Dual layer microfluidic-based wounding device with a top air channel (black) and bottom cell chamber (orange). B. Schematic of wounding in the device. Cells are first loaded into the cell chamber (top). Increasing the air pressure in the air channel lowers a pillar in the ceiling of the cell chamber until cells below the pillar are mechanically crushed (middle). The pillar returns to the original height when air pressure is released (bottom). C. Ca^{2+} response visualized by the Fluo-4 Ca^{2+} indicator dye over a period of 5 minutes following a 300μm diameter wound (black circle). D. Top: Maximum single-cell (dots) Ca^{2+} response to a 300μm wound. Inset shows maximum Ca^{2+} response to 300μm wound in the presence of the ATP scavenger apyrase. Bottom: Maximum single-cell (dots) of Ca^{2+} response to wound according to distance from the wound. E. Same as D but for maximum ERK response. F. Top: Cells are binned according to distance from the wound (Figure 3A) and the average and standard deviation (error bars) are found for each bin. Middle: Coefficient of variation (CV) calcuated by dividing the standard deviation of each bin by the mean of that bin. Bottom: Ca^{2+} has higher variability than ERK response for the wound according to the CV of every bin for all wounds (Black bar=average CV, *p*-value by t-test).

We adapted the computational SNR analysis to wound response data to determine the influence of spatial patterns on response fidelity. As opposed to the dose-response data, the wound response data uses the distance of each cell from the wound as the input rather than the concentration of activating ligand (Figure 3A). Similar to the dose-response data, noise is estimated by averaging the cellular response variability over all distances. The variability between the average response magnitude of each distance constituted the signal (Figure 3B). Other statistical measures of response fidelity such as mutual information were also adapted for the wound context (Figure 3, Supplemental Figure S11).

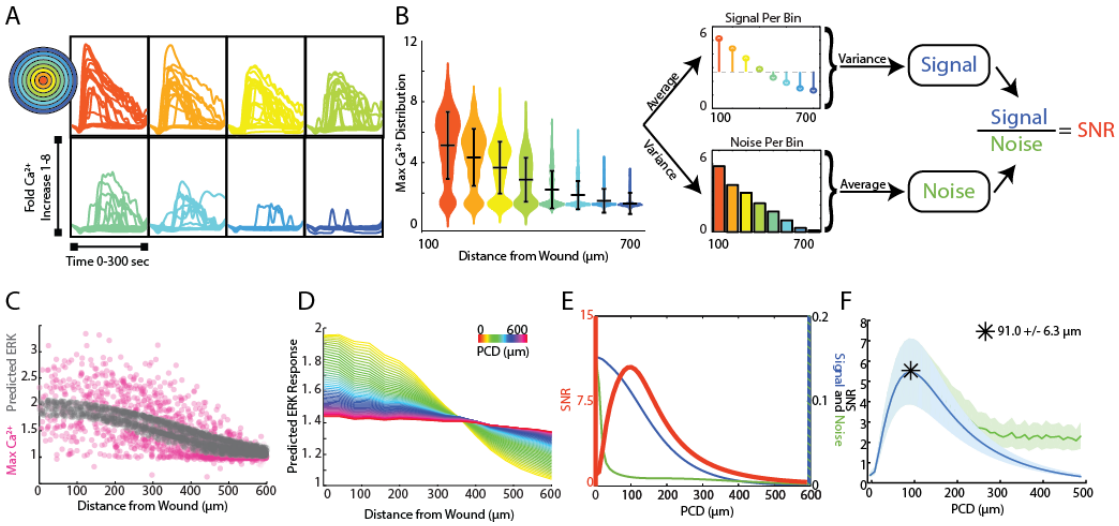

Figure 1.3. Signal to Noise analysis of initial wound response shows limits to paracrine communication. A. Representative single-cell time traces of Ca^{2+} response to wounding, grouped according to distance from the wound (concentric circle colors). B. SNR calculation method for Ca^{2+} response adpated to the wound. Horizontal bars represent bin average and error bars represent bin variance. C. Maximum single-cell (dots) Ca^{2+} response to wound with respect to distance away from the wound (pink). Predicted ERK cellular response after paracrine communication as determined by local averaging (gray). Local averaging done in same manner as Figure 1F. D. Predicted ERK response according to distance from the wound using PCDs of 0 to 600μm (colorbar). Predicted ERK response determined through local averaging using increasing PCDs results in decreased response magnitude over space. E. Signal (blue), Noise (green) and SNR (orange) as function of PCD of locally averaged Ca^{2+} response trends in panel D. F. SNR analysis of locally averaged Ca^{2+} response to a wound with increasing PCD shows a maximum SNR at PCD of 91.0μm+/-6.3μm indicated by the asterick (blue, SEM indicated by shaded region, N=5). The maximum SNR for conditions controlled for biologically relevant integration times show the same maximum SNR (green, Material and Methods).

The maximum primary Ca^{2+} response shows highly variable cellular response when plotted according to distance (Figure 3C, pink). This variability complicates the ability for a cell to distinguish its respective position to the wound based on its response We again mimicked paracrine communication to predict the post-paracrine ERK response by locally averaging the single-cell Ca^{2+} wound response using a Gaussian kernel (Figure 1F). Locally averaging the cellular Ca^{2+} response creates a smoother predicted ERK response pattern versus distance from the wound (Figure 3C, gray). However, the reduction in variability also decreases the overall response pattern trend. Locally averaging the Ca^{2+} signal using increasing PCDs decreases the magnitude of change of the average predicted ERK response between cells closest to the wound and farthest from the wound (Figure 3D). In other words, the response gradient becomes less obvious when cells are averaged over larger distances. Therefore, although the increase in PCD decreases response noise, the corresponding decrease in signal demonstrates the limit of PCD on the SNR benefit (Figure 3E). The difference in rates at which the signal and noise decrease results in a maximum SNR at a PCD of 91.0 +/- 6.3μm (SEM, N=5) (Figure 3F). This peak corresponds to a PCD where the amount of noise is decreased to the lowest amount possible without reducing the response gradient due to "over-averaging". The predicted PCD with maximal benefit did not change when we expand the model to consider limits dues to diffusions (Figure 3F green curve, Material and Methods). Similar analysis using mutual information statistics shows a similar PCD with the maximal mutual information at the distance that showed maximal SNR (Figure 3E, F, Supplemental Figure S11B). This analysis shows that the benefits from paracrine communication depend on how far a paracrine molecule travels which, in this specific case, has a maximal benefit at ~100 μm, or approximately three cell diameters.

Direct measurement of Paracrine Communication Distance

We next empirically measured the PCD in our experimental system to compare to the PCD predicted to maximize the SNR in the wound context. To measure the PCD of ERK activation we first established a co-culture system that allows us to separate the effects of autocrine and paracrine signaling. Our assay utilizes a synthetic GPCR: Designer Receptors Exclusively Activated by Designer Drugs (DREADD). The Gq human muscarinic derived GPCR DREADD is activated by a synthetic small molecule, clozapine-N-oxide (CNO), that has no known endogenous receptors [126]. In addition, DREADD activates the Gq pathway similar to purinergic ATP receptors [127]. Using a co-culture of DREADD expressing (activated by CNO) and non-expressing cells (not activated by CNO), we can determine which cells release EGF (DREADD expressing-red) and which cells accept EGF (non-expressing-gray) (Figure 4A). Using a synthetic system allows us to directly measure the average communication distance of EGF. CNO addition selectively activates Ca^{2+} response in DREADD expressing cells while the surrounding non-expressing cells show no response indicating a lack of paracrine activation of Ca^{2+} response in cells (Figure 4A). Although some systems show that Ca^{2+} response can propagate from cell-to-cell through gap junctions [128], this does not appear to be the case in MCF-10A cells as non-expressing cells showed no cytosolic Ca^{2+} increase upon activation of DREADD cells. Alternatively, ERK response was found in both DREADD expressing and the surrounding non-expressing cells upon CNO addition but was inhibited in both cell types in the presence of the EGFR inhibitor tryphosphitin AG1478, confirming paracrine activation of ERK in the DREADD system (Figure 4B). The Ca^{2+} and ERK responses in the DREADD system suggest that local averaging takes place only at the EGF level between Ca^{2+} and ERK response. Additionally, increasing the ratio of DREADD cells to non-expressing cells shows an increasing ERK

response magnitude in non-expressing cells, further supporting that paracrine communication locally activates ERK (Figure 4C).

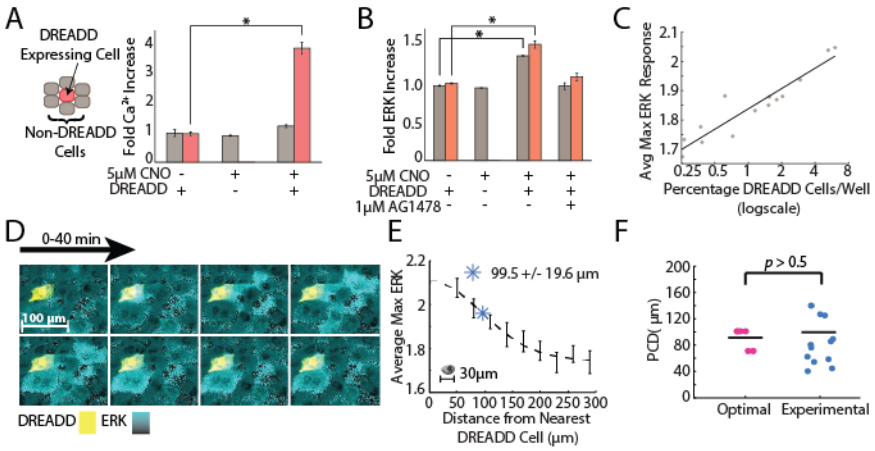

Figure 1.4. Empirical PCD measurement using DREADD synthetic GPCR show that cells use optimal level of paracrine communication levels that maximizes cellular response fidelity. A. The addition of 5μM CNO to a co-culture of DREADD expressing (red) and non-expressing (gray) MCF-10A cells shows increased fold Ca^{2+} response in DREADD expressing cells but not non-expressing cells. (SEM indicated by error bars, N=3; * *p*-value<0.005, t-test) B. Fold ERK increase in DREADD co-culture assay. Both DREADD and non-expressing cells show significant ERK increase when both DREADD cells and 5μM CNO are present. ERK activation inhibited by 1μM AG1478. (SEM indicated by error bars, N=3; * *p*-value < 0.005, t-test) C. The average maximum ERK response of non-expressing cells in a given well increases linearly with an increasing percentage of DREADD cells per well. D. Representative images from a timelapse experiment showing ERK activation (cyan) in non-expressing cells surrounding a single activated DREADD cell (yellow) over a 40 minute time period. ERK activation level indicated by black to cyan colorbar E. Average maximum ERK activation in non-expressing cells surrounding single DREADD cell according to distance from the DREADD cell. PCD was calcuated as the spread, or sigma, of the fitted Gaussian curve (dashed line) and measured to be 99.5μm +/-19.6μm (blue *) (SEM indicated by error bars, N=12 DREADD cells). Scale bar represents average length of a single-cell. F. Comparison between calculated optimal PCD per wound (pink, Figure 3F) and experimentally measured PCD found using the DREADD co-culture assay per DREADD cell (blue, figure 4E) (*p*-value>0.5, t-test). Horizontal bars represent average.

We measured the PCD by monitoring local paracrine ERK activation with our DREADD co-culture assay. We co-cultured DREADD cells at a low concentration compared to non-expressing cells to ensure that neighboring non-expressing cells were activated only by a single DREADD cell. We then analyzed the ERK response of ~1500 non-expressing cells

neighboring a DREADD cell. (Figures 4D, E). Local ERK activation of non-expressing cells surrounding a DREADD cell show decreasing response with increasing distance from the DREADD cell. ERK response as a function of distance follows a Gaussian fit, consistent with how the concentration of diffusing molecules, like in paracrine signaling, changes over distance (Figure 4E) [129]. The PCD was determined by calculating the spread, or sigma, of this Gaussian curve. According to our fit, the paracrine activation of ERK has a communication distance of 99.5 +/- 19.6μm (SEM, N=12 DREADD cells). This empirically measured value is statistically similar to the predicted communication distance value that maximizes the SNR of wound response (Figure 4F). In other words, the cellular communication distance is tuned to maximize the overall response fidelity during wound response signaling.

Discussion

Multicellular organisms utilize cellular diversity for specialization and division of labor. However, the variability between cells can be detrimental due to the potential loss of response fidelity [5,109–111,130]. Paracrine communication can serve to share information between cells to regulate cellular variability. In this study we analyzed the benefits and limitations of paracrine communication based information sharing between cells as a mechanism to control cellular response variability.

We analyzed the limits of paracrine communication on cellular response fidelity in two cases. First we analyzed the response to a spatially uniform ligand. Our analysis reveals that, under these conditions, the magnitude of single-cell response fidelity increases as a function of the PCD with no upper bound. In order for cells to facilitate larger PCDs, cells would need to synthesize larger amounts of paracrine signaling molecules or utilize fast diffusing paracrine ligands like H_2O_2 [119]. The increased energy required to synthesize the

additional molecules is likely to be minor in comparison to the overall energetic demand of a cell. Therefore cells could potentially take advantage of large PCDs to substantially mitigate biochemical noise. However, a spatially uniform input, while common in cell culture experiments, is likely an inadequate representation of physiological conditions. In the second case we analyzed the response of cells to spatially defined inputs in the form of a mechanical epithelial wound. We analyzed the cellular response to extracellular ATP gradients, a damage associated molecule, following a controlled wounding of an epithelial monolayer *in vitro*. Similar to developmental systems, an extracellular input ligand conveys positional information in wound response [131,132]. Analysis of the paracrine communication benefit in our novel quantitative wound response assay with defined spatial perturbations demonstrates that paracrine communication increased cellular response fidelity, but with limitations. Unlike the spatially uniform ligand in the first case, the magnitude of the response fidelity benefit varies with increasing PCD. The maximal increase of cellular response fidelity occurrs at a PCD of ~100μm, or approximately 3 cell diameters. In vivo work measuring ERK propagation using the same EKAREV FRET sensor also showed propagation extending ~100μm [133]. Our results demonstrate that the paracrine information sharing benefit depends on the input ligand spatial scale, or PCD. Furthermore, empirical measurements of paracrine communication match the physiologically relevant spatial wound response maximum communication distance.

The process of wound healing is a complex multi-stage program that coordinates the action of multiple cell types over multiple timescales, from minutes to weeks, to address an acute need. The initial steps of wound healing programs propagate information concerning the wound in a manner that is appropriate to the magnitude of damage. Both inflammatory and fibrotic processes, critical steps in wound response signaling, are damaging when they go

awry. Therefore, the initial cellular responses and the establishment of signaling gradients are key steps in wound healing. The mechanistic details underlying how tissues robustly match the wound response magnitude to the extent of wound-induced damage remain unknown. Our results demonstrate that intercellular communication during the initial wound response is optimized to increase overall response fidelity and provides the initial evidence that matching the wound response to wound damage is a critical aspect to wound healing programs. Future work is needed to further investigate tissue level response fidelity during wound healing programs.

Paracrine communication increases the fidelity of response at the single-cell level by mitigating biological noise at the single-cell level. Each cell integrates information from its local neighborhood to increase its individual response fidelity. Local averaging at the cellular level is a distinct mechanism compared to the benefit of global averaging at the population level. Without any paracrine communication, the reliability of the average of a cell population response can only increase with the size of the population. This is a consequence of the central limit theorem where the uncertainty of a sample average decreases with sample size. However, this increase in reliability is only true for the population average and not for individual cells in the population. Therefore, in cases where the biologically significant output is the collective action of the population, e.g. the secretion of a cytokine, intercellular information sharing is not required. However, when biologically significant output requires single-cell action, local information sharing via paracrine communication increases cellular response fidelity. Therefore, whether paracrine communication is required remains context dependent. It is possible that paracrine information sharing is more prevalent in signaling networks that support individual cellular decisions and less prevalent in cases where biologically meaningful outcomes result from population averages.

In cases where paracrine information sharing is used as a method to mitigate biological noise, the breakdown of this system could be detrimental. In vivo studies of ERK response in mammary tumor cells using the same EKAREV FRET sensor utilized here show highly variable ERK response that may lead to the survival and propagation of cancer cells [134]. Although the cause for this heterogeneity is unknown, one possible mechanism may be the breakdown of paracrine communication between cells similar to how our partial inhibition of paracrine communication showed no decrease in ERK variability (Figure 1, Supplemental Figure S4).

The abundance of paracrine communication in mammals, i.e. the activation of a receptor by a ligand synthesized by another cell, demonstrates the heavy utilization of intercellular communication [135,136]. Paracrine averaging demonstrates how intercellular communication enables cellular collective decision making where the “wisdom of the crowd” is greater than the individual cell. Theoretical and empirical work in humans and animal collectives has shown that the benefit of collective decision making depends on the size of the group; big crowds are not always better than small crowds [137–140]. Therefore, it is likely that the extent of secretion of each paracrine ligand is adjust the level of cellular information sharing to ensure an effective collective decision.

The optimal PCD we identified is not universal. Rather, the optimal distance depends on the specific shape of the spatial pattern of the initial activating ligand and the noise pattern of the primary response. Additionally, propagation patterns of the same activating ligand can depend on the physiological signaling context as demonstrated by differences found during in vivo ERK propagations under wound and normal conditions [133]. The effective PCD can be regulated at the cellular level by several possible factors to optimize the benefit of paracrine communication to the specific noise and spatial patterns characteristic to each signaling

system [141–143]. PCD also depends on the effective diffusion coefficient of the secreted molecule, transmitted signal strength (e.g. number of secreted molecules), and receiver cell sensitivity (e.g. receptor K_d). The diffusion coefficients of paracrine signaling molecules can vary by two orders of magnitude, let alone differences in signal strength and receptor sensitivity in individual paracrine signaling pathways [144,145]. Fine-tuning each of these factors provides a possible mechanism for cells to regulate the PCD and thereby the extent a cell locally communicates. The ability to specifically tune PCD raises the possibility that evolutionary pressures can tune paracrine communication to provide the optimal benefit in many other paracrine communication systems.

Material and Methods

Ca^{2+} and ERK Measurements in MCF-10A Cells

MCF-10A cells were cultured following established protocols [146]. Before plating cells, each surface was first treated with a collagen (Life Technologies), BSA (New England Biolabs), fibronectin (Sigma-Aldrich) solution in order for cells to completely adhere, according to established methods. In order to maintain a viable environment, cells were imaged at 32°C and 5% CO_2. All EGF (PeproTech) titrations and DREADD experiments were conducted in 96-well plates using extracellular hepes buffer (ECB) to reduce background fluorescence (5 mM KCl, 125 mM NaCl, 20 mM Hepes, 1.5 mM $MgCl_2$, and 1.5 mM $CaCl_2$, pH 7.4). All imaging for wounding was done in MCF-10A assay media [146].

ERK and Ca^{2+} activation by DREADD

Cells were plated at a density of 2,000,000 cells/100mm plate and allowed to adhere overnight. Cells were transfected with the Gq-coupled DREADD HA-tagged hM3D with an mCherry tag using a 3:1 ratio of FuGene HD (Promega) to DNA and allowed to incubate overnight [127]. In order to measure the paracrine signal from a single-cell, non-transfected

cells were mixed with DREADD-transfected cells at ratios of 1:0, 1:1, 1:2, 1:5, 1:7, and 0:1 (non-transfected:DREADD) and plated in 96-well plates at a density of 30,000 cells/well. The following day, cells were loaded with 1μM Hoechst dye for nuclear imaging for 30 minutes for cell segmentation purposes. 5μM clozapine-N-oxide (CNO) (Enzo Life Sciences) was added to each well to specifically activate DREADD cells. ERK activation was monitored using the EKAREV FRET reporter [30,31] and Ca^{2+} activation was monitored using the Ca^{2+} indicator dye Fluo-4 using the published protocol (Invitrogen).

Cell clustering assay and analysis

In order to measure the standard deviation of Ca^{2+} and ERK activity within a small group of cells, MCF-10A cells were plated at densities of 1000, 2000, and 3000 cells per well in a 96-well plate, taking advantage of the natural tendency for MCF-10A cells to cluster together. Cells were stimulated with 10μM or 100μM ATP and imaged for 5 minutes every 3 seconds (Ca^{2+}) or 30 minutes every minute (ERK).

Standard deviation and average expression of Ca^{2+} and ERK were analyzed by grouping cells in to clusters based on the distances between cells and clusters (Figure 1, Supplemental Figure S1). Following the cluster analysis, the average and standard deviation of Ca^{2+} and ERK activation were calculated for each cluster. ERK activation was measured using the ERK FRET reporter (Albeck et al. 2013; Komatsu et al. 2011) and Ca^{2+} activation was monitored using the genetically encoded sensor R-GECO [125].

Wounding Device Design, Fabrication, and Wounding Assay

Master molds for the microfluidics based wounding device were created using silicon wafers and layer-by-layer photolithography using established methods [147]. A separate mold for both the air layer and cell layer were made using negative photoresists and masks. Chips were made by pouring uncured polydimethylsiloxane (PDMS) onto each mold, allowing the

PDMS to harden, and bonding the layers together and subsequently to a glass slide. Cells were loaded into the devices through the inlet port using a 20G needle. During wounding the outlet port was plugged using tape and the inlet port held a reservoir of media to prevent evaporation in the chamber. Wounding was accomplished by increasing the air pressure in the top layer of the device until the pillar made contact with the bottom of the device after which the air pressure was released to raise the pillar back up. Cells were loaded in to the wounding device at a density of 15,000,000 cells/mL using a 20G needle. Following trypsinization and resuspension, cells were put on ice to prevent aggregation. Two o-rings were attached to the device surrounding both the inlet and outlet ports for media reservoirs. Each o-ring was attached using a thin film of vacuum grease. Wounding devices were kept in an empty pipet box filled with water to prevent media evaporation. Cells were allowed to adhere for 18-24 hours before wounding.

Imaging and Image Analysis

Imaging was accomplished using a Nikon Plan Apo λ 10X/0.45 objective with a 0.7x demagnifier and Nikon Eclipse Ti microscope with a sCMOS Zyla camera. All imaging was accomplished using custom automated software written using MATLAB and Micro-Manager [148]. Image analysis was accomplished using a custom MATLAB code published previously [109] and is available through GitHub repository https://github.com/rwollman/CellSegmentation.git.

Model for paracrine communication based on local isotropic diffusion

The paracrine ligand concentration (P) for a cell at position (x, y) observed by (P(x,y)) is the local average of the concentration of ligand released by cells in the local neighborhood (Figure 1A). We modeled this paracrine ligand local average using a convolution of two functions: $S(x,y)$ that represents the amount of ligand secreted by each cell and $D(x,y)$ that

represents the expected diffusion of the paracrine ligand during the timescale of paracrine signal integration:

(1) $$P(x,y) = \iint dudvS(x,y)D(x-u,y-v)$$

The function S(x,y) was estimated using experimental cellular Ca^{2+} response data according to:

(2) $$S(x,y) = \begin{cases} \max\left(Ca_i^{2+}(t)\right) & x,y \in cell\ i \\ 0 & x,y \in background \end{cases}$$

The function D(x,y) was approximated to follow Gaussian weights with a length-scale we named the Paracrine Communication Distance (PCD):

(3) $$D(x,y) = \frac{1}{PCD\sqrt{2\pi}} e^{\frac{-\left(x^2+y^2\right)}{PCD^2}}$$

Detailed analysis of how PCD depends on diffusion, number of secreted paracrine molecules, sensitivity of detection, physiological levels of fluid flow [149], and cellular decoding of time varying paracrine signal are presented in Material and Methods. In cases where biologically relevant integrations times may influence the predicted paracrine communication response, the PCD did not exceed the approximate distance EGF could travel before the first ERK response (Figure 1G, Figure 3F, Material and Methods). Based on single-cell ERK data to ATP stimulation, this time was found to be ~5 minutes which resulted in a maximum PCD of ~300μm (data not shown) based on EGF diffusion coefficient of 50μm^2/sec.

Signal to Noise Analysis

Signal to Noise ratio analysis on Ca^{2+} response to ATP titration data was estimated as was done previously (Selimkhanov 2014). Briefely, the signal S was calculated using:

(4) $$S = \underset{bins}{\mathrm{var}}\left(\underset{cells}{\mathrm{avg}}\left(\max_{t}\left(Ca^{2+}(t) \right) \right) \right)$$

The noise N was calculated by:

(5) $$N = \underset{bins}{\mathrm{avg}}\left(\underset{cells}{\mathrm{var}}\left(\max_{t}\left(Ca^{2+}(t) \right) \right) \right)$$

Where $Ca^{2+}(t)$ is the temporal time series of Ca^{2+} response measured experimetnally. Cells are separated into bins according to either different dosages of ATP added to multiple wells (Figure 1) or different distances from the wound source (Figure 3). SNR was then simply: SNR=S/N.

Analysis of the effects of diffusion, secretion and integration time on paracrine communication

In this section we analyze how the Paracrine Communication Distance (PCD), the characteristic length-scale of paracrine communication, depends on factors related to the paracrine signal. Specifically we look into how the PCD depends on the diffusion coefficient D, the number of molecules released from a cell N_r, the number of molecules needed for detection N_d, and the total integration time T.

To understand how PCD depends on the factors mentioned above, we considered the diffusion of a paracrine ligand from a single cell to its surrounding neighbors. We considered a 2D-like geometry where cylindrical cells, each of height h_c and radius ρ, grow in a chamber of total h_f height. We simplify the below analysis by approximating the cell monolayer geometry to a series of "cell cylinders". The key results of the scaling of PCD and

required integration time are similar for other comparable geometries (data not shown). Under these conditions one could write the analytical solution of the diffusion equations:

(6) $$C(r,t) = \frac{\mathrm{N_r}}{h_f \cdot 4D\pi t} \mathrm{e}^{-\frac{r^2}{4Dt}}$$

Where $C(r,t)$ is the concentration of paracrine ligand for distance *r* and time *t*. For a neighboring cell to respond to this paracrine signal, a critical number of molecules N_d need to reach the volume surrounding the cell. We assume that a cell "senses" a volume comparable to the volume of a cell itself. For a cylindrical cell of area $\pi\rho^2$ and height h_c the critical concentration required for cellular response will be:

(7) $$C_{detect} = \frac{N_d}{h_c \pi \rho^2}$$

This is simply the required number of molecules divided by the cell volume. Combining equations 6 and 7 we can solve for the distance and time of where the critical concentration will be reached. Solving for distance we get that

(8) $$r_{detect} = 2\sqrt{Dt \ln\left(\frac{\rho^2 h_c N_r}{4DtN_d h_f}\right)}$$

The concentration of the paracrine ligand is diluted as it diffuses from the source. Therefore, there is a point in space which is the maximal distance from the source that the critical detection concentration C_{detect} will be reached at some point in time. Distances that are greater than the critical distance will only experience concentrations lower than the critical detection concentration C_{detect}. The existence of such maximum can also be seen by the non-

monotonous dependency of r_{detect} on t in equation 8. To find the maximal distance we can simply find the maximum of 1.3 in respect to t. Doing so we get that:

(9) $$PCD = e^{-\frac{1}{2}} \rho \frac{\sqrt{h_c}\sqrt{N_r}}{\sqrt{h_f}\sqrt{N_d}}$$

We can simplify the analysis by the introduction of two dimensionless variables: 1) $S = \frac{N_r}{N_d}$ represents the strength of the signal and is defined as the ratio of released molecules N_r and the number of molecules needed to detect the signal N_d . 2) $\eta = \frac{h_c}{h_f}$ represents the fraction of the height of the flow chamber that cells occupy. When we substitute the new variables into Eq 1.4 we get that:

(10) $$PCD = \tfrac{1}{2} e^{-\frac{1}{2}} \rho \sqrt{\eta S}$$

Interestingly this shows that the value of PCD does not depend on the diffusion coefficient. Rather, PCD scale as a function of the square root of the strength of the signal S with a multiplicative constant that depends on the specific cell geometry. PCD also depends on cell geometry with the cell radius ρ and the relative height of a cell in the effective environment η. Supplemental Figure S6 shows equation 10 graphically.

While the analysis above shows that the diffusion coefficient has no influence on the overall PCD, the time required to reach this maximal distance has important biological implications. “Paracrine averaging” requires cells to integrate the signal. However, the time required for signal integration must be biologically feasible given the cellular response time and diffusion coefficient.

From equation 8 we can identify the time by which the PCD is maximal to be:

(11) $$T_{int} = \frac{\rho^2 \eta S}{4eD}$$

The integration time grows linearly with signal strength S. This is because the PCD itself scales as a square root of S and the diffusion time grows with the square of the distance. The integration time decreases with increasing diffusion coefficient as expected. Supplemental Figure S7 shows the scaling of the integration time with the diffusion coefficient for a few PCD values.

For diffusion coefficient values of ~10-100 $\frac{\mu m^2}{s}$ and a PCD of 100 μm (similar to the distance measured in Figure 3) integration times ranged between 0.5 to 5 minutes. Given that ERK activation is observed only after 5 minutes post-activation, the required integration time does not pose an issue. However, larger PCDs will require higher diffusion coefficients to allow proper integration of the paracrine signal. Interestingly, H_2O_2, another key paracrine signaling molecule critical to initial wound response signaling, has a diffusion coefficient of ~2000 $\frac{\mu m^2}{s}$. A larger diffusion coefficient could allow for a much longer PCD with reasonable biological integration times.

Analysis of the effect of fluid flow on paracrine communication

All the analysis above assumed static conditions, i.e. no fluid mixing or advection of any kind. In this section we analyze the degree to which the principles of paracrine communication are applicable in non-static conditions.

Non-static fluid conditions potentially have two effects on mass transport. 1) Non-static fluid conditions can create mixing due to turbulence and 2) Laminar advection can transport secreted molecules away from the secretion source. Since the extracellular environment is characterized by a low Reynold's number there is effectively no turbulent mixing in biologically relevant parameters.

To analyze the relative contribution of advection and diffusive transport we utilize a dimensionless number, the Péclet number (*P*), that represents the ratio between the contribution of advection and diffusion:

(12) $$P = \frac{vL}{D}$$

Where *v* is the interstitial flow rate, D is the diffusion coefficient and L is the characteristic length scale. In our case, the characteristic length scale is the PCD, which depends on the signal strength as described above (equation 10 & Supplemental Figure S6). Therefore, the P number can be expressed as a function of the signal strength S and diffusion coefficient:

(13) $$P = \frac{\sqrt{S\eta}\,\rho v}{D\sqrt{e}}$$

Graphical representation of this expression is shown in Supplemental Figure S8 where the map of D and S is color coded by the Péclet number with three highlighted regions: A red region where flow will dominate, a cyan region where diffusion will dominate, and the region in between where both advection and diffusion contribute to paracrine communication.

To gain further insight into the relative contribution of advection and diffusion we looked at the distance molecules will travel via advection for a specific signal strength

(S=1000). As can be seen in Supplemental Figure 8B, for diffusion coefficients of small protein ligands advection will contribute minimally.

When considering positional accuracy of cellular response, an important consideration is that advection can potentially "shift" the effects of paracrine signaling downstream of the flow. Even if the shift is characterized by low Péclet number, advection can interfere with positional information accuracy (as analyzed in Figure 3). To estimate the potentially degrading effects of flow we calculate the expected level of positional accuracy error induced by flow. We estimate that the wound induced signaling gradient (Figure 3C) to be > 500 μm. Therefore the effect on positional accuracy will be minimal (<10%) at advection distances up to 50 μm, or for a PCD of 100 μm, a Péclet number up to 0.5. The isocline of a Péclet number of 0.5 is shown in Supplemental Figure 8A as a dotted black line. This shows that for paracrine ligands with a diffusion coefficient >40 μm^2/sec, advection will have little effect on positional accuracy of initial wound response signaling.

Analysis of the effect of cellular decoding schemes on paracrine communication

The analysis in the previous two sections assumes that the concentration of the paracrine ligand decreases over increasing distance from the source of secretion according to a Gaussian fit where the diffusion length-scale represents the PCD. The cellular response to a paracrine ligand depends on cellular decoding of the temporal paracrine concentration profile a cell observes. As both the temporal profile of the secreted paracrine molecule and the temporal cellular decoding are unknown, we consider the simple assumption of a Gaussian profile reasonable. To quantitatively test this assumption we compared the Gaussian profile to an alternative model that could be addressed analytically. In the alternative model, we assume that all paracrine molecules are released at T=0 and that cellular decoding of the paracrine

signal is simple temporal averaging. Under these assumptions one can write an expression of the temporal average of the paracrine concentration at a distance r from the source as:

(14) $$C_{avg}(r) = \int_0^{t_0} C(r,t) = \int_0^{t_0} \frac{\mathrm{N_r}}{h_f \cdot 4D\pi t} \mathrm{e}^{-\frac{r^2}{4Dt}} = -\frac{\mathrm{N_r}}{4D\pi \mathrm{h_f\, t_0}} \mathrm{ei}\left(-\frac{r^2}{4D\mathrm{t_0}}\right)$$

Where all symbols follow equation 6 and ei represent the exponential integral:

$$\mathrm{ei}(x) = \int_{-\infty}^{x} \frac{e^t}{t} dt$$

Comparison of the two models can be seen in Supplemental Figure S9. Overall, the two models generate very similar Paracrine Averaging Weights (the effect of cellular decoding of paracrine signal). There is a small discrepancy between the two models at very low distances (<50 μm). However, this discrepancy is most likely a result of the assumption in the alternative model that all the paracrine molecules are released at once. Under the more realistic assumption where paracrine molecule release duration is not much smaller than the time to diffuse 50 μm (12.5 seconds at D=50 μm^2/sec) we anticipate that the similarity between these two profiles will further increase.

Acknowledgments

We thank Jeff Hasty, Ryan Johnson, and Megan Dueck from the San Diego Center for Systems Biology Cell Dynamics core for their technical assistance. The work was supported by GM111404 & EY024960 (RW), and a training grant (GM007240) for LNH.

Chapter 1 in full is a reprint of the material as it appears in Handly, L.N.; Pilko, A.; Wollman, R. Paracrine communication maximizes cellular response fidelity in wound signaling. eLife. 2015, 4:e09652. The dissertation author is the first author on this paper.

Supplemental Figures

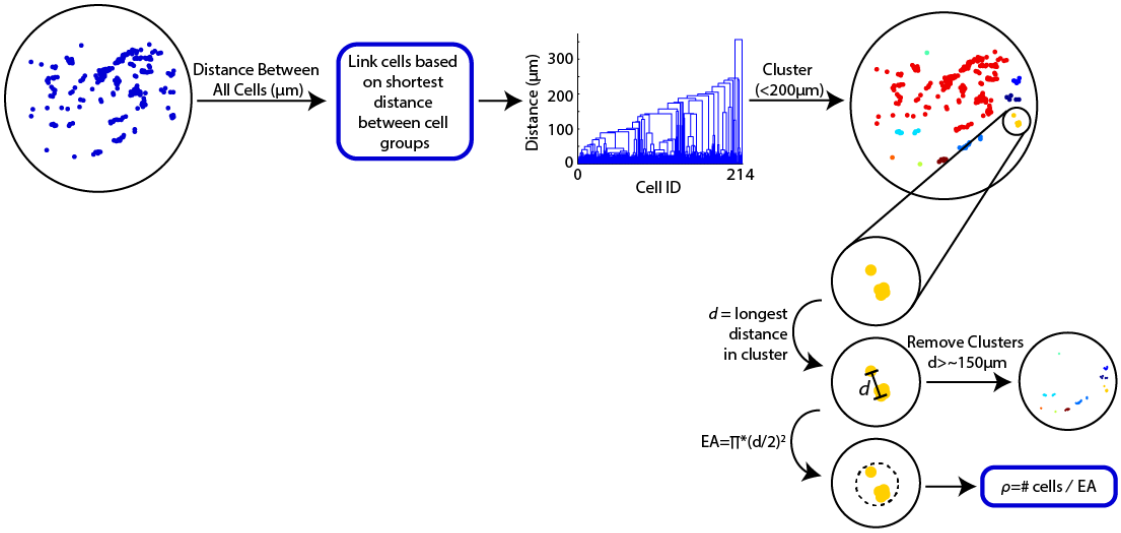

Supplemental Figure S1.1. MCF-10A cells can be separated and analyzed in cell clusters when plated at low densities. Cells were grouped into clusters based on distance between cells. First, the distance between all cells was calculated based on the distance from the center of the cell. A hierarchical clustering based on the shortest distance linkage between cell groups was used to group cells. Cells linked within 200µm (maximum PCD, or MCD) of each other were assigned as a cell cluster. To calculate the local cell density (ρ) within the cluster, the longest cell-to-cell distance within the cluster was measured (*d*). Clusters with a *d* greater than 150µm were removed since the PCD was calculated to be 99.5µm. Effective area (EA) of the cluster was calculated by finding the area of the circle encompassing the cluster using *d* as the diameter of the circle. ρ was estimated by dividing the number of cells within the cluster by the EA. This process was repeated for all clusters.

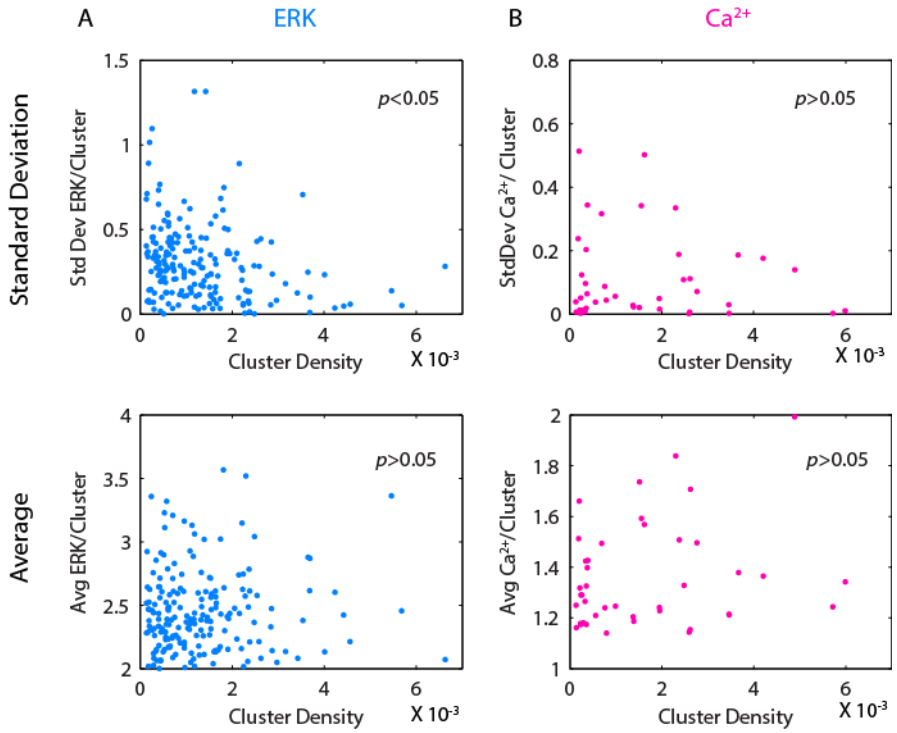

Supplemental Figure S1.2. Cluster standard deviation and cluster average as a function of cluster density show significant trends for ERK activation but not Ca2+ activation. Cells were plated at low density to form groups of cells and clustered according to figure 1—figure supplement 1. ERK and Ca^{2+} activation were monitored following the addition of 10μm ATP. All *p*-values obtained through Pearson correlation. A. Standard deviation of ERK expression for each cluster significantly decreases with increasing cluster density (*p*-value<0.05) indicating that ERK expression becomes more reliable as cells coordinate with more cells. The average ERK expression per cluster, however, does not significantly decrease (*p*-value>0.05) verifying that the decrease in standard deviation of ERK expression is not related to changes in the average ERK expression. B. The standard deviation of Ca^{2+} activation does not significantly decrease with increasing cluster density (*p*-value>0.05) assuring that decreases in ERK cluster standard deviation represent communication via paracrine signaling and not due to similarities in cellular expression between sister cells in a cluster. Similarly to A., the average Ca^{2+} response for each cluster does not significantly decrease with increasing cluster density (*p*-value>0.05).

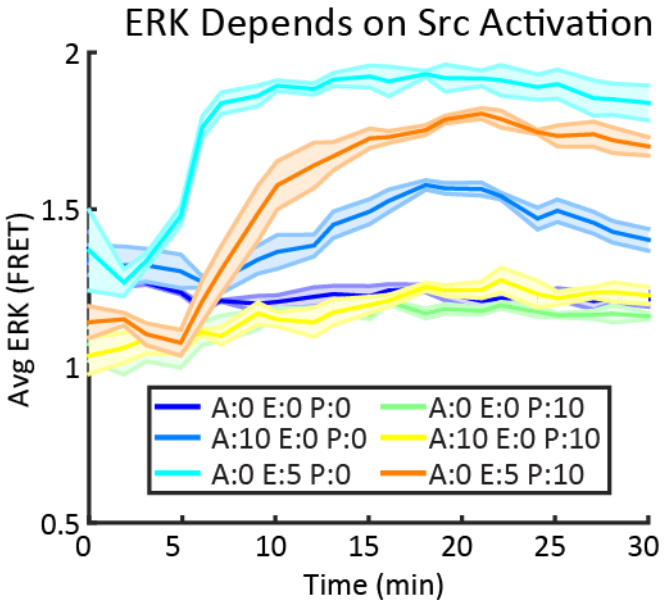

Supplemental Figure S1.3. Paracrine ERK activation depends on Src prior to MMP activation. MCF-10A cells expressing EKAREV FRET ERK reporter were incubated with 10μM of the selective Src kinase inhibitor PP2 (Tocris) for 30 minutes at normal cell culture conditions before addition of 10μM ATP or 5ng/mL EGF. (A=AP, E=EGF, P=PP2). Shaded region indicates SEM (N=5).

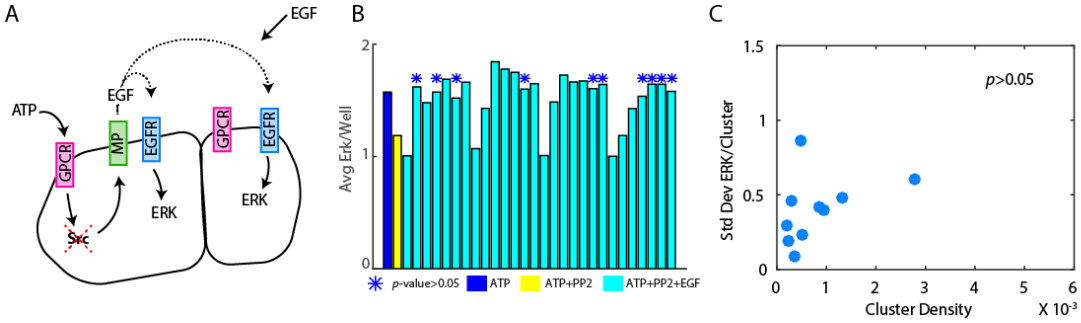

Supplemental Figure S1.4. Inhibiting paracrine communication does not allow decreased cellular response variability. Cells were plated in a 96 well plate at low density to form groups and clustered according to figure 1—figure supplement 1. All *p*-values obtained through Pearson correlation. A. Cells were incubated with varying concentration of PP2 (0—10μM, red dashed X) for 30 minutes in normal cell culture conditions to inhibit Src to varying degrees and therefore limit the concentration of secreted EGF (black broken lines). Additional EGF (0—1 ng/mL) was added to compensate for the lack of secreted EGF to ensure that the average ERK response of the well remained similar to controls. Cells were then perturbed with 10μM ATP to activate ERK response in a paracrine fashion. PP2, EGF, and ATP were added such that cells were perturbed with every combination of PP2, EGF, and ATP. B. Wells that showed statistically similar average ERK activation (cyan) to the control well (blue, 10μM ATP) were selected for analysis (blue *, *p*-value>0.05, t-test). Complete inhibition by PP2 shown as negative control (yellow). The cells within wells labeled with blue * were clustered in the same manner as figure 1—figure supplement 1. C. The standard deviation of ERK response per cluster is not significantly correlated with cluster density (*p*-value>0.05, Pearson correlation) indicating that ERK variability does not decrease when paracrine communication is inhibited.

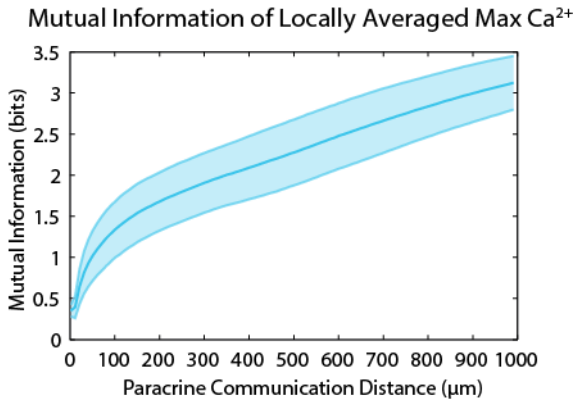

Supplemental Figure S1.5. Mutual information and SNR both continue to increase with increasing PCD. A mutual information analysis using established methods on a Ca^{2+} dose response to ATP as a secondary and more sophisticated approach to our SNR analysis [109]. As expected, the mutual information exhibits a similar increase with increasing PCD with no upper bound, similar to the SNR analysis. Shaded area represents SEM (N=5).

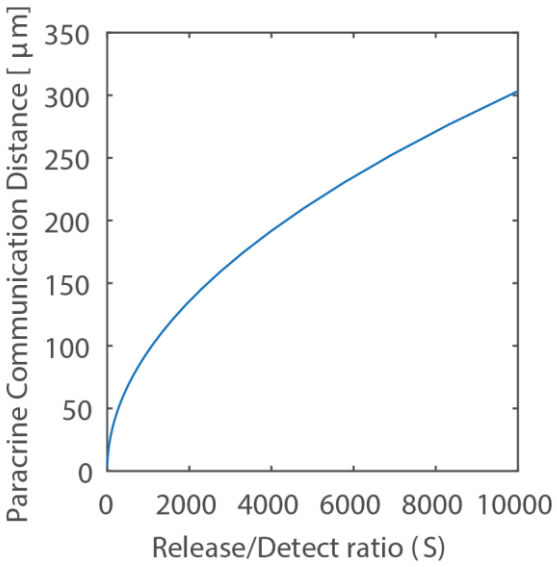

Supplemental Figure S1.6. Scaling of Paracrine Communication Distance. The scaling of Paracrine Communication Distance with the strength of the paracrine signal expressed as the ratio of released molecules to the number of molecules needed for signal detection. Cell radius is 10 □m, height 15 µm and chamber height is 60 µm. These values were chosen to approximate the analysis in Figure 2.

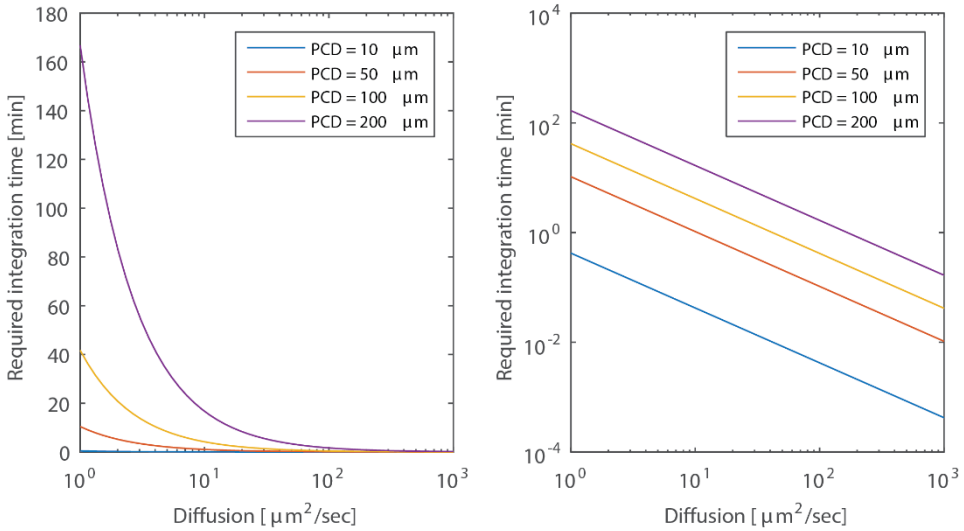

Supplemental Figure S1.7. Required Integration time. The required integration time for selected Paracrine Communication Distance values shown in linear (left) and log (right) scales. Geometry is the same as in Figure 1 supplement 6: Cell radius is 10 µm, height 15 µm and chamber height is 60 µm.

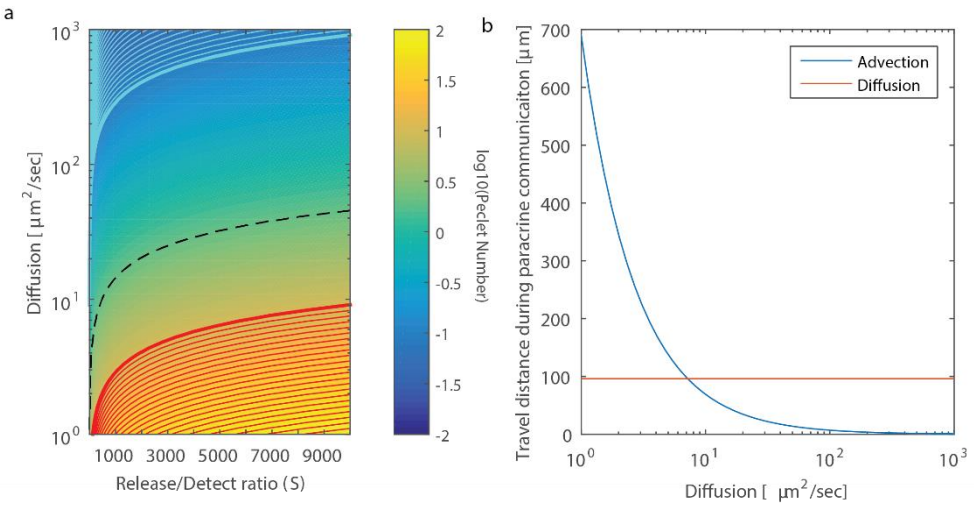

Supplemental Figure S1.8. The effect of fluid flow on paracrine communication. a Color map of Péclet number (shown in Log10 scale). The red (cyan) region show combination of signal strength (S) and Diffusion coefficient (D) where advection (diffusion) is dominating over diffusion (advection). The dotted dark line show the regime above which advection will have little effect on positional accuracy. **b** The expected distance of advection based spread as a function of D for a signal strength of 1000. The geometry and parameters here are the same as in Figures M1 & M2. Interstitial flow rate used was 0.3 µm/sec based on [149].

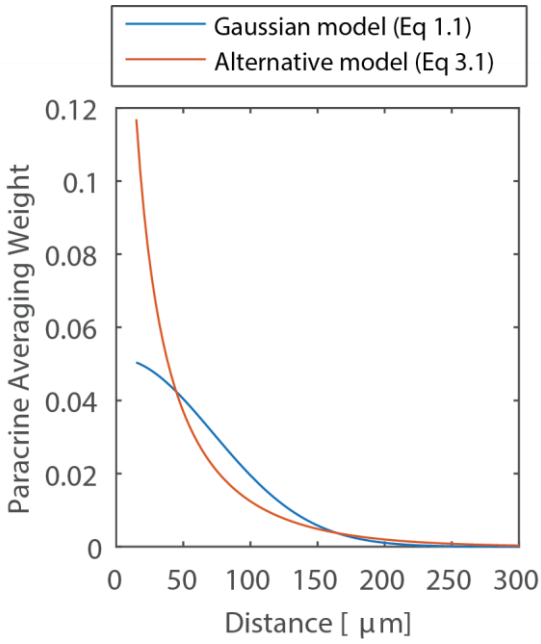

Supplemental Figure S1.9. The effect of cellular decoding schemes on paracrine communication. Comparison of Paracrine averaging weights between the Gaussian model used in this work to represent paracrine communication and an alternative model that is based on an assumption of instant release temporal averaging of paracrine signal.

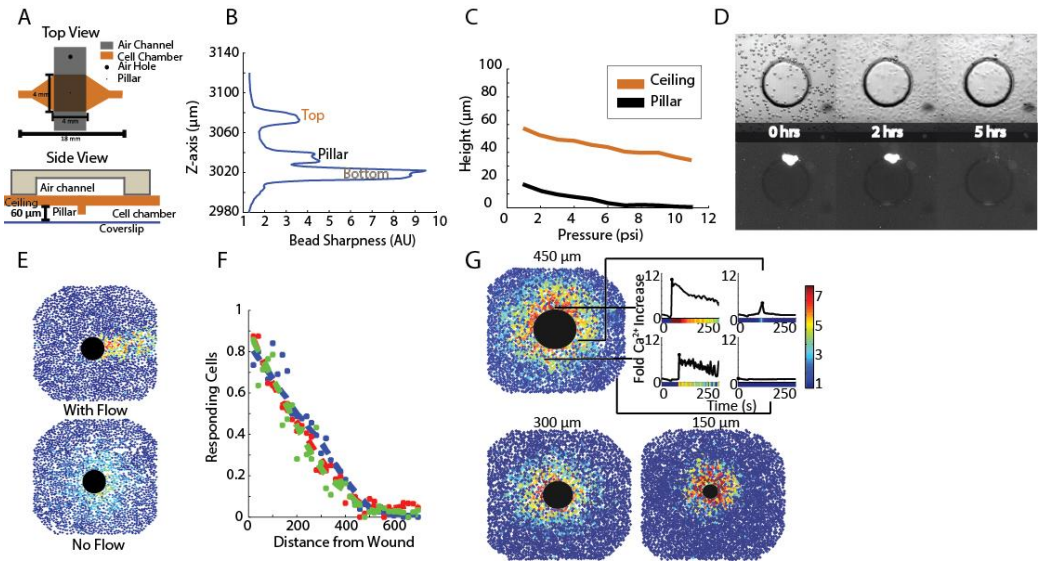

Supplemental Figure S1.10. Microfluidic wounding device characterization demonstrates cell viability, isotropic wounding, wounding control, and reproducibility. A. Top (top panel) and side (bottom panel) view of the microfluidic wounding device. The wounding device is constructed of 2 layers, a top air layer (black) and bottom cell chamber (orange). The air layer has an air hole at one end where air pressure is increased by flowing air through a small tube connected to the hole. The ceiling of the cell chamber has a PDMS pillar that is lowered down on to the cells in the cell chamber when air pressure is increased in the air layer. B. Cell chamber heights were measured by loading fluorescent beads into the device and allowing them to settle on the surfaces within the device (bottom, pillar, ceiling). Height was measured by scanning the cell chamber through the Z-axis and seeing where the beads had settled based on where they were in focus (bead sharpness). Cell chamber height within the device as measured by bead sharpness revealed a chamber of approximately 60µm in height and a distance of approximately 15µm between the bottom of the pillar and the bottom of the cell chamber. These distances provide ample room for cell growth while still limiting the z-space in which extracellular signals can diffuse. C. The change in height of the ceiling of the cell chamber (orange) and the pillar (black) with increasing air pressure as measured by bead sharpness shows controlled movement of the pillar with increasing air pressure. Although the ceiling of the cell chamber also moves with the pillar, this does not interfere with cellular wounding. D. MCF-10A cells were loaded in to the wounding device cell chamber and allowed to adhere in the presence of propidium iodide (PI) to measure cell viability within the device over time in static media conditions. Cells were able to adhere within 5 hours after which the media began to dry up and cells began to die indicating that cellular response following wounding can be measured for up to 5 hours in a static setting before cell death. E. Wounding in non-static (with flow) and static (no flow) media conditions. Static media conditions were accomplished by placing a piece of tape over one of the ports of the wounding device during imaging. When flow was present, the signal went in the direction of the flow. However, when flow was not present, the signal propagated isotropically from the wound indicating that the response was a measurement of signal transfer and not simply due to the flow in the environment. F. Ca^{2+} response according to distance away from the center of a 300µm diameter wound shows reproducible wounding between 3 experiments as represented by 3 different colors. Cellular response is measured as the percentage of responding cells according to distance away from the wound. G. Due to the layer-by-layer photolithography manufacture of the molds used to make the wounding device, the size of the wound can be controlled and reproducible. We were able to measure the single-cell spatiotemporal Ca^{2+} response in cells wounded by a 450µm, 300µm, and 150µm wound. The single-cell responses for 4 different cells at varying distances from the wound are highlighted for the 450µm wound with colorbar indicating fold maximum increase.

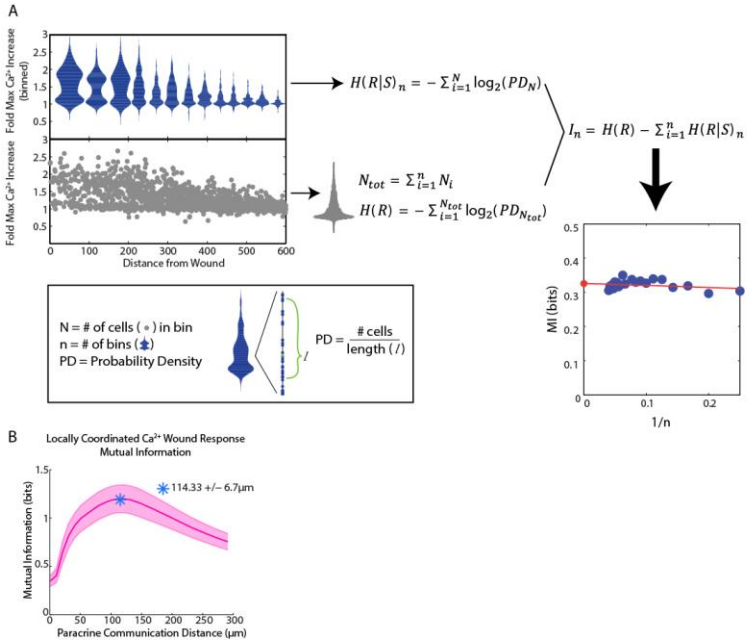

Supplemental Figure S1.11. Mutual information analysis of locally averaged Ca^{2+} response to wounding shows similar peak to SNR analysis. A. Mutual information was calucated by binning the cells according to their distance away from the wound. The maximum response per cell (gray circles) is divided into bins such that there are the same number of cells in each bin (blue plots). The conditional response ($H(R|S)$) is calculated for each bin using the probability density (PD) of each cell. The PD of each cell is calculated by finding the 10^{th} nearest neighbor for each cell, counting the number of cells within that space, and then dividing by the distance covering that space. The non-conditional response ($H(R)$) is calcuated by measuring the PD of all of the cells. The cells are divided into multiple sets of bins and the mutual information (I) is calculated for each set of bins. Each I is then plotted according to the number of bins after which the final MI is found by extrapolating back to zero to ensure no dependence on bin number. B. Mutual information was used as a measurement tool to further confirm the SNR analysis of locally averaged Ca^{2+} response. Indeed, the mutual information analysis found an optimal coordination length-scale of 114.33μm +/-6.7μm (SEM, N=5), matching the optimal coordintation length-scale found in the SNR analysis (shaded region indicates SEM, N=5).

CHAPTER 2

Wound induced Ca^{2+} wave propagates through a simple Release and Diffusion mechanism

Abstract

Damage associated molecular patterns (DAMPs) are critical mediators of information concerning tissue damage from damaged cells to neighboring healthy cells. Adenosine triphosphate (ATP) acts as an effective DAMP when released into extracellular space from damaged cells. Extracellular ATP receptors monitor tissue damage and activate a Ca^{2+} wave in the surrounding healthy cells. How the Ca^{2+} wave propagates through cells following a wound is unclear. Ca^{2+} wave activation can occur extracellularly via external receptors or intracellularly through GAP junctions. Three potential mechanisms to propagate the Ca^{2+} wave are: Source and Sink, Amplifying Wave, and Release and Diffusion. Both Source and Sink and Amplifying Wave regulate ATP levels using hydrolysis or secretion, respectively, while Release and Diffusion relies on dilution. Here we systematically test these hypotheses using a microfluidics assay to mechanically wound an epithelial monolayer in combination with direct manipulation of ATP hydrolysis and release. We show that a Release and Diffusion model sufficiently explains Ca^{2+} wave propagation following an epithelial wound. A Release and Diffusion model combines the benefits of fast activation at short length-scales with a self-limiting response to prevent unnecessary inflammatory responses harmful to the organism.

Introduction

The epithelium provides a key protective layer that isolates the internal environment of an organism from outside pathogens. A temporary loss of the epithelial barrier caused by wounds places an organism in a precarious and vulnerable situation [119]. A timely defense and healing program is vital for organism survival. Wound healing response requires the coordinated action of multiple cell types [132]. Neutrophil cells infiltrate the wounded area to proactively defend against infection. Phagocytosis of pathogens and necrotic cells requires macrophage recruitment. Fibroblasts increase extracellular matrix secretion and provide contractile forces. Finally, epithelial cells proliferate and migrate to close the wound. A plethora of cytokine mediators secreted by the different cell types participating in the wound response regulate the complex wound healing program. However, cytokine secretion, which often requires de novo expression, occurs on an hour timescale [132,150]. The sensitive state of the wounded epithelium requires that wound healing begin as soon as the wound occurs. Therefore, cytokine secretion is too slow to act as the initial signal that activates wound healing programs. A timely wound healing response necessitates a transcriptionally independent program to propagate information regarding the wound to neighboring healthy cells.

Damage Associated Molecular Patterns (DAMPs) are a set of chemical ligands that are released from cells upon physical damage [150]. DAMPs provide the first indication of damage and are used to activate transcriptionally independent programs. DAMPs quickly propagate information regarding the wound to notify healthy cells surrounding the wound that cellular damage has occurred. Potentially, the gradients formed by DAMPs provide neighboring cells with positional information concerning how far they are from the wound

[132]. These damage signals include Ca^{2+} waves, reactive oxygen species, and purinergic molecules such as ATP [150].

Although most known for its key role in cellular metabolism, there has been a growing appreciation for an additional role of ATP as a paracrine signaling molecule [151]. Under normal physiological conditions, extracellular ATP levels are typically ~1nM; six orders of magnitude less than cytoplasmic ATP levels of ~1mM [152]. This large gradient, actively maintained by cells, makes ATP a powerful damage indicator as any loss of membrane integrity causes an immediate increase in extracellular ATP. Furthermore, previous work has demonstrated ATP as a key initial signaling molecule required for epithelial wound response activation [153–155].

ATP released from cells following a mechanical wound initiates a Ca^{2+} wave that propagates from the wound in an isotropic pattern. Initially, ATP released from wounded cells binds to P2Y receptors on surrounding healthy cells to increase cytoplasmic Ca^{2+} levels (Figure 1). More precisely, phosphorylation of P2Y by ATP activates PLC to catalyze the degradation of PIP2 to IP3 and DAG [56,156]. IP3 then binds to IP3R on the ER to release Ca^{2+} stores into the cytoplasm. IP3 can pass between cells through connexin channels resulting in intracellular Ca^{2+} activation [157–160]. While the intracellular pathways that connect extracellular ATP to activate Ca^{2+} signaling have been carefully elucidated [161], the tissue-level pathways responsible for forming the Ca^{2+} wave remain unclear.

Like other DAMPs, ATP may provide positional information for healthy cells surrounding a wound. Handly et al. found that ATP-activated ERK transactivation maximizes positional information by locally averaging the EGF signal using paracrine communication [93]. However, the spatio-temporal propagation of ATP following a wound to provide positional information is not fully understood. Several models have been proposed to explain

how neighboring cells are notified of damage following the passive release of ATP from damaged cells (Figure 1). In the first model, Source and Sink, ectonucleotidases such as NTPDase2 quickly hydrolyze ATP [162,163]. In the second model, Amplifying Wave, active propagation mechanisms increase the concentration of extracellular ATP. Specifically, it has been proposed that cells exposed to extracellular ATP respond by actively secreting ATP through Pannexin-1 channels [162,164–166]. In the third model, Release and Diffusion, simple diffusion and dilution of the initial ATP signal controls the Ca^{2+} wave propagation. While molecular studies show support for each model, uncertainty remains concerning which model is primarily responsible to propagate the ATP induced Ca^{2+} wave. Here we use a novel wounding device to mechanically wound an epithelial monolayer [93]. Using single-cell wound data combined with genetic and pharmaceutical manipulations, we identify the underlying mechanism responsible for the spread of extracellular ATP in a mechanically wounded epithelial monolayer.

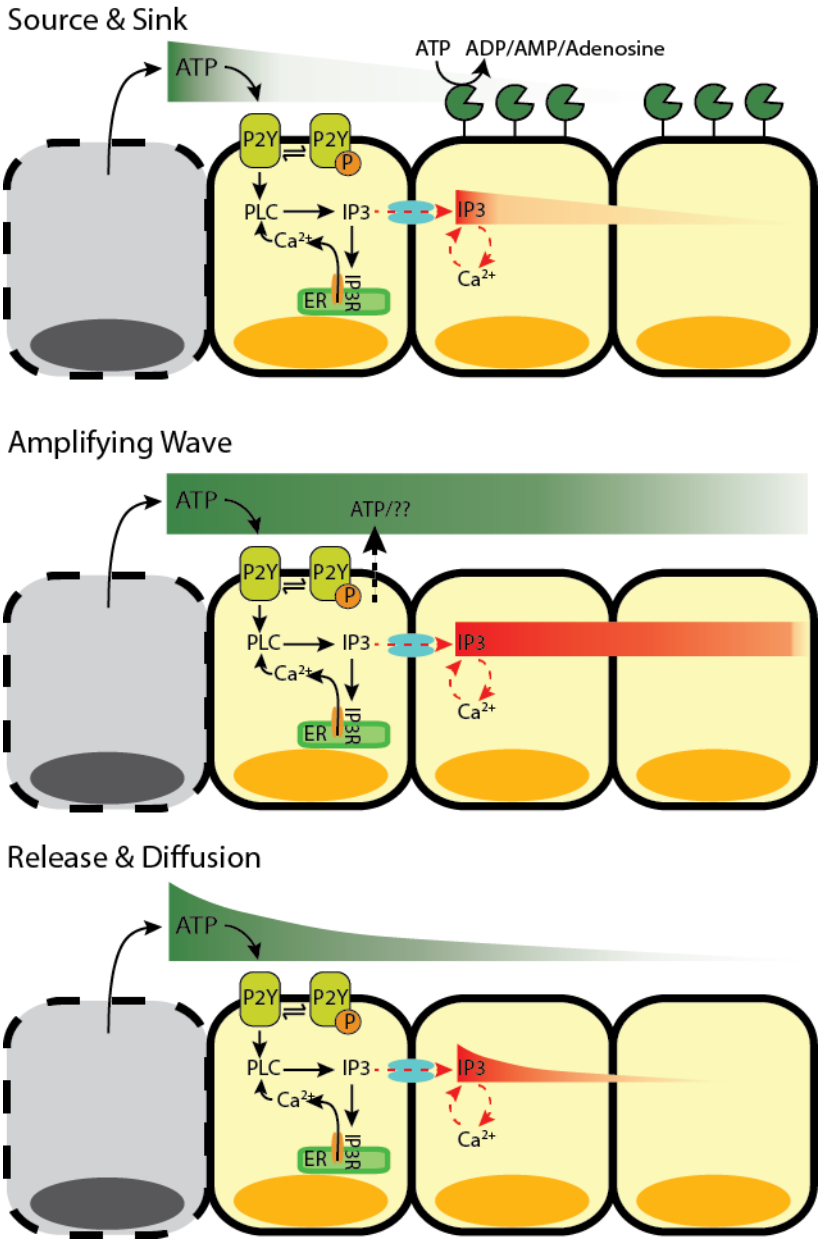

Figure 2.1. Ca^{2+} wave propagation following wounding. Following wounding, cytosolic Ca^{2+} levels increase in the surrounding healthy cells in a wave-like manner. Ca^{2+} can be activated in cells either extracellularly (ATP binding to extracellular receptors) or intracellularly (IP3 travelling between cells). However, the Ca^{2+} wave can propagate using different mechanisms. 1) Source and Sink (top). After the initial release of ATP from wounded cells (Source) that activates the cells immediately surrounding the wound, the remaining activating molecules (either ATP or IP3) are hydrolyzed (Sink) as they move away from the wounded area and activate neighboring cells. 2) Amplifying Wave (middle). In this active mechanism, ATP-induced ATP release continues to propagate ATP and IP3 molecules to activate neighboring cells at faraway distances. 3) Release and Diffusion (bottom). The release of ATP from wounded cells diffuses away from the wound source to activate neighboring cells with little to no regulation.

Results

Mechanical wounds initiate a Ca^{2+} wave that scales with wound size

Measuring the spatial cellular wound response requires the ability to wound an epithelial monolayer in a convection free environment. We developed a novel microfluidics wounding device to mechanically wound an epithelial monolayer (Figure 2A) [93]. Our wounding device has 2 layers: a bottom cell layer and a top air layer. Cells in the cell chamber are mechanically wounded by a pillar in the ceiling of the cell layer when air pressure is increased in the air layer (Figure 2B). Flow is blocked during wounding to prevent any convection within the device to create an isotropic Ca^{2+} wound response (Figure 2C). One advantage of our wounding device over conventional wounding methods such as scratch assays, is the ability to create reproducible wounds (Figure 2D). Reproducible wounding is imperative to measure the spatial response to ensure that each wound elicits a similar response from the surrounding healthy cells.

The isotropic cellular Ca^{2+} response to wounding contains a spatial response that scales with wound size. When measuring the Ca^{2+} response to mechanical wounds, we saw that the fraction of responding cells decreased with increasing distance from the wound (Figure 2D). Additionally, this response scales with wound size (Figure 2E, Supplemental Figure S1). Spatial information, or knowing where you are in relation to the wound, is imperative during wound healing to ensure that each cell responds appropriately. For Ca^{2+} response we see that cells that are further away from the wound have a smaller and slower response compared to cells that are closer to the wound. Although there are biological processes in place, such as paracrine averaging, to ensure that each cell generates the appropriate response based on its position [93], we wondered how the initial Ca^{2+} gradient forms in an epithelial monolayer following a wound.

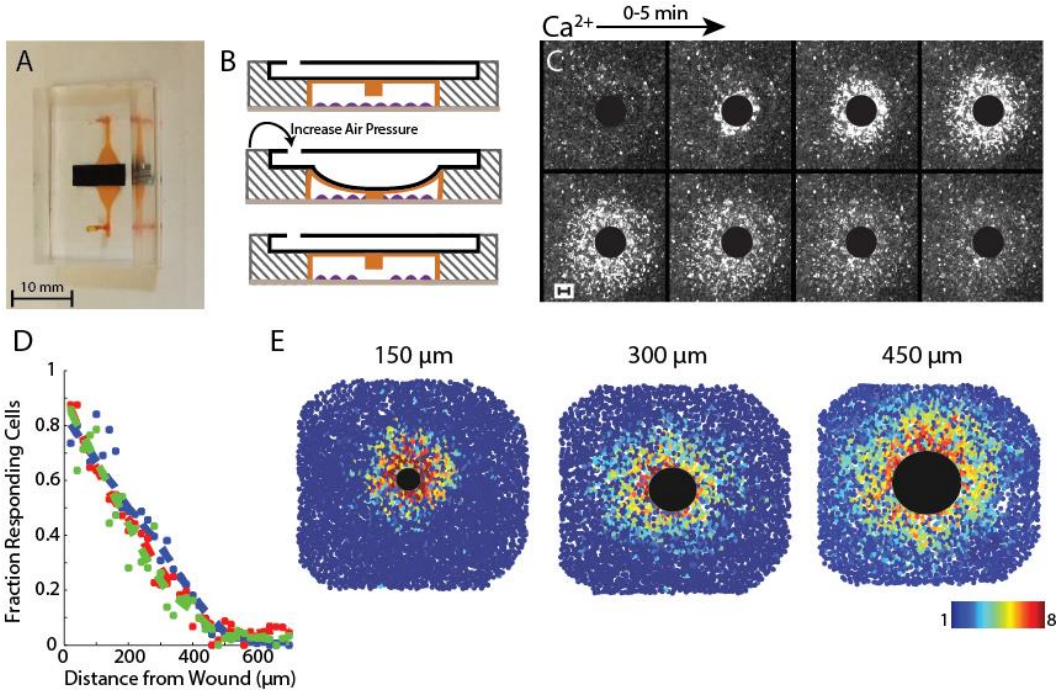

Figure 2.2. Measuring the Ca^{2+} wave using a microfluidic wounding device. A. Image of dual-layer microfluidics device with the cell chamber (orange) and the air channel (black). B. Cells (purple) cultured in the cell chamber (orange) are mechanically wounded when a PDMS pillar in the ceiling of the cell chamber is lowered down when air pressure is increased in the air layer (black). C. Ca^{2+} activation in MCF-10A cells following a 300μm diameter wound. Black circle represents wounded area. Images are over a period of 5 minutes. Cytosolic Ca^{2+} level indicated by Fluo4-AM. D. The fraction of responding cells across the healthy surrounding cells decreases with increasing distance from the wound. Dashed lines represent best fit for three different 300μm wounds. E. The Ca^{2+} wave scales with increasing wound size. Large black circle represents wounded area according to the title of the wound (150μm, 300μm, and 450μm diameter wounds). Colored circles represent fold maximum Ca^{2+} increase for a single cell as indicated by the colorbar. Ca^{2+} increase indicated by Fluo4-AM dye

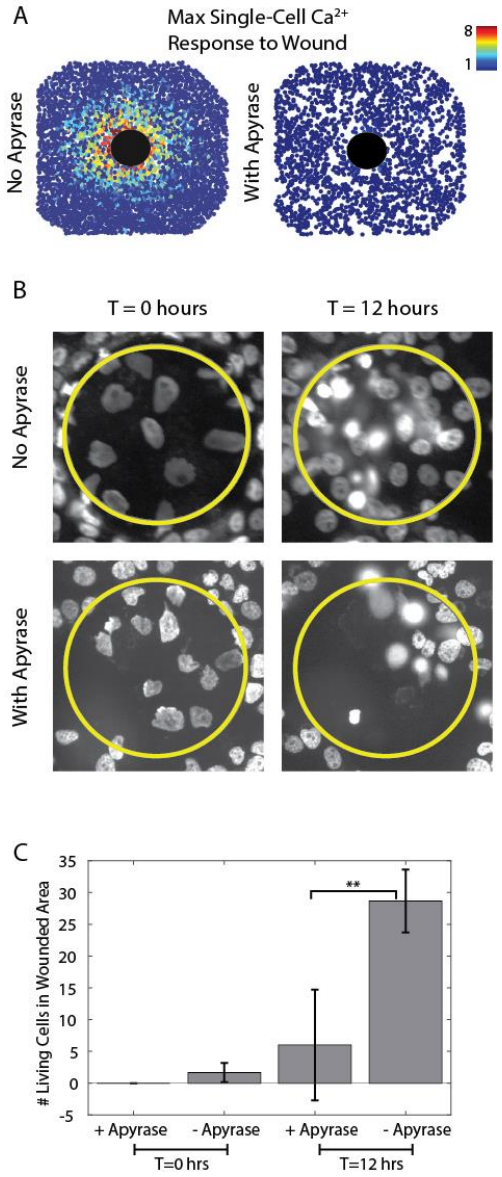

Figure 2.3. Cell migration following a wound requires ATP. A. Maximum Ca^{2+} projection indicated by Fluo-4 AM following a 300µm in diameter wound in the absence (left) and presence (right) of the ATP scavenger apyrase (5U per wounding device). Each circle represents the fold maximum Ca^{2+} increase of a single cell as indicated by the colorbar. Large black circle represents wounded area. Mechanical wounding generates a Ca^{2+} response gradient surrounding the wound. However, apyrase inhibits this response. B. Nuclei with Hoechst staining following a 150µm in diameter wound in the absence (top) and presence (bottom) of the ATP scavenger apyrase (5U per wounding device). Yellow circle represents wounded area and T indicates time following wound. Surrounding healthy cells migrate into the wounded area in the absence of apyrase in 12 hours. No migration is seen following wounding in the presence of apyrase. 3C. Quantification of Figure 3B. The number of living cells in the wounded area is significantly higher (**p<0.05, t-test, n=3 wounds) in the absence of apyrase 12 hours following a wound compared to a wound in the presence of apyrase.

ATP is released in response to mechanical wounding and is required for wound closure

ATP released from wounded epithelial cells is a key damage indicator in the initial wound response [153–155]. We verified whether a monolayer of MCF-10A cells, a breast mammary epithelial line, requires ATP release to heal mechanical wounds made by our wounding device. We first established whether initial ATP release is required for a Ca^{2+} response. Indeed, the addition of the ATP scavenger apyrase prevented a gradient of Ca^{2+} activation in cells surrounding the wound (Figure 3A, Supplemental Figure S1). Next we determined whether the initial ATP released from wounded cells is necessary to the overall wound healing response. Epithelial cells migrate and proliferate in order to close the wound. Other work has shown that epithelial cells simply sense empty space in order to proliferate and migrate into the wounded area [167,168]. However, unlike a scratch assay, wounded cells tend to remain in the wounded area using our wounding device. We see that wounding MCF-10A cells in the presence of apyrase prevents cells from migrating into the wounded area (Figure 3B, C). This lack of migration in the presence of apyrase agrees with previous wound studies [169–172]. Overall we see that the initial release of ATP is required for Ca^{2+} activation as well as epithelial wound closure.

The Ca^{2+} wave propagates by extracellular activation

The wave of Ca^{2+} activation following wounding can spread using extracellular or intracellular stimulus. Previous data indicates that the Ca^{2+} response following wounding depends on the DAMP ATP [120,150,173–175] (Figure 3). ATP initially released from damaged cells binds to extracellular receptors on neighboring cells causing a cytosolic Ca^{2+} increase within that cell. From here, the propagation of Ca^{2+} activation in neighboring cells can occur via extracellular or intracellular mechanisms. Extracellular stimulation results from ATP propagation that can be augmented by either active release of ATP from cells or

degradation by nucleotidases [162,163]. Intracellular stimulation takes place when IP3 travels between cells via GAP junctions to bind to IP3R to release internal Ca^{2+} stores cells in neighboring cells [157–160]. In intracellular stimulation, ATP released from wounded cells activates the initial Ca^{2+} response in healthy cells immediately surrounding a wound. GAP junctions then propagate the spread of Ca^{2+} activation to cells farther away from the wound. We first determined whether the Ca^{2+} wave propagates internally or externally.

In order to determine whether the spread of the Ca^{2+} wave is activated through intracellular or extracellular mechanisms, we used our novel wounding device to wound cells in the presence and absence of flow. Based on our previous data (Figure 2) we saw that the Ca^{2+} wave travels isotropically from the wound in the absence of flow. We wondered whether the response would maintain an isotropic pattern if cells are wounded in the presence of flow. If flow has no influence on the shape of the response, then the Ca^{2+} wave most likely propagates internally where it is not influenced by extracellular flow. When wounding in the presence of flow, however, we saw that the response propagates in the direction of the flow (Figure 4A, Supplemental Figure S1). This indicates that Ca^{2+} wave propagation is not independent of the extracellular environment.

We used a synthetic GPCR DREADD (Designer Receptors Exclusively Activated by Designer Drugs) that is activated by the small molecule clozapine-N-oxide (CNO) to further investigate whether Ca^{2+} response propagates intra or extra-cellularly by activating a Ca^{2+} response without ATP in a single cell and watching the surrounding cells in a non-wound

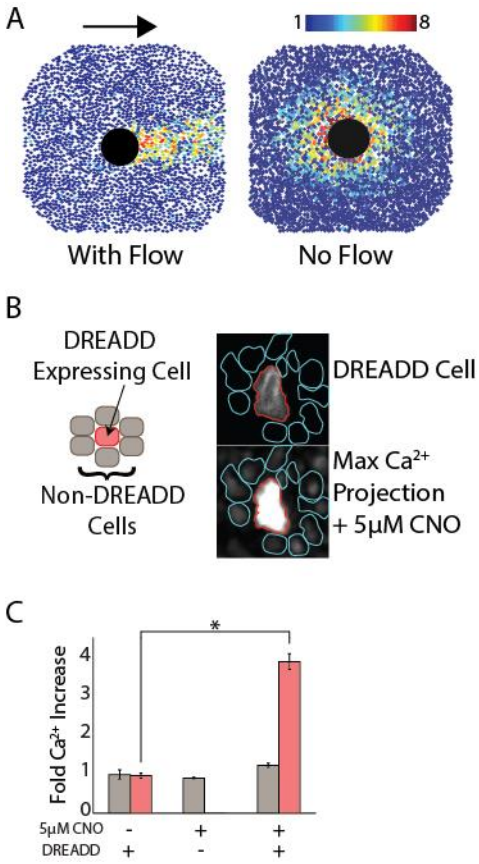

Figure 2.4. Ca^{2+} wave spread requires extracellular activation. All Ca^{2+} indicated by Fluo4-AM dye. A. When flow is present during the wound, the Ca^{2+} wave goes in the direction of the flow (left). When flow is blocked, the Ca^{2+} wave propagates in an isotropic manner (right). Large black circle represents wounded area and colored circles represent fold maximum Ca^{2+} increase for a single-cell as indicated by colorbar. Arrow indicates direction of flow. B. DREADD expressing (red) and non-expressing (gray) MCF-10A cells are co-cultured such that each DREADD expressing cell ss surrounded by non-expressing cells (left cartoon). Upon the addition of 5μM CNO, the DREADD cell shows Ca^{2+} activation but the surrounding non-expressing cells do not (right images). Images on right show the DREADD cell marked in red and the surrounding non-expressing cells in cyan. Top image shows expression of mCherry in DREADD cells and bottom image shows maximum Ca^{2+} projection following addition of 5μM CNO as indicated by Fluo-4, AM. C. Quantification of Figure 4B. DREADD expressing cells marked in red and non-expressing cells marked in gray. Only DREADD expressing cells have Ca^{2+} increase following the addition of 5μM CNO. (Error bars indicate SEM, n=3; *p-value<0.005, t-test).

setting [126,127]. By activating a Ca^{2+} response without a wound, we ensured that there are no artifacts created by flow during Ca^{2+} wave propagation. We used a DREADD that uses Gq mediated signaling to ensure that Ca^{2+} is activated in cells using the same signaling mechanism as ATP activated Ca^{2+} response. In order to determine whether the Ca^{2+} wave travels internally, we co-cultured DREADD expressing and non-expressing cells such that DREADD expressing cells are surrounded by non-expressing cells (Figure 4B). The addition of CNO activates a Ca^{2+} response in DREADD expressing cells. Whether the Ca^{2+} wave travels internally or externally is indicated by whether the surrounding non-expressing cells also show an increase in Ca^{2+}. A Ca^{2+} response in the surrounding non-expressing cells would indicate an internal propagation mechanism of the Ca^{2+} wave. However, if the wave depends on extracellular stimulus, then only the DREADD expressing cells will respond. We found that upon the addition of CNO, only DREADD expressing cells respond (Figure 4C, Supplemental Figure S2). Taken together, these pieces of evidence indicate that the Ca^{2+} wave travels extracellularly.

Source and Sink: Extracellular ATP degradation does not impact Ca^{2+} activation

In the Source and Sink model, ATP hydrolysis dominates ATP propagation. Here the lifetime of an ATP molecule determines how long and far it will diffuse from the wound source. Ectonucleotidases present on the plasma membrane metabolize ATP to ADP, AMP, or Adenosine [176]. The degradation of ATP released from wounded cells can lead to the formation of the Ca^{2+} wave gradient. In this case, each subsequent cell receives a lower dose of ATP resulting in a lower magnitude of Ca^{2+} activation in a cell. We used pharmaceutical manipulation to determine the role of ATP degradation in creating the Ca^{2+} wave gradient.

We determined whether ectonucleotidases play a role in Ca^{2+} activation by ATP after confirming the presence of ectonucleotidases on MCF-10A cells from previous research

[177,178]. Because activation depends on ATP and not necessarily from a wound, we performed these assays in a non-wound setting. We used the ectonucleotidase inhibitor ARL67156 at 200µM, according to literature values, and added a low dose of ATP (0.5 µM) [179]. Low concentrations of ATP were used to ensure that cells were not saturated with ATP, making nucleotidase inhibition negligible to the overall response. We found that inhibiting ectonucleotidases did not impac the average Ca^{2+} response (Figure 5A). Because we did not observe a change in Ca^{2+} activation, we further confirmed whether ectonucleotidases influence ATP activation of Ca^{2+} by measuring extracellular phosphate following ATP addition to cells (Figure 5B). Indeed, there is no significant difference in extracellular phosphate concentration in cells perturbed with ATP and without. Additionally, at high levels of ATP (5 µM) we saw no difference between ATP and the nonhydrolyzable analog ATPγS, further supporting that ATP hydrolysis does not play a role in shaping Ca^{2+} activation (Figure 5C).

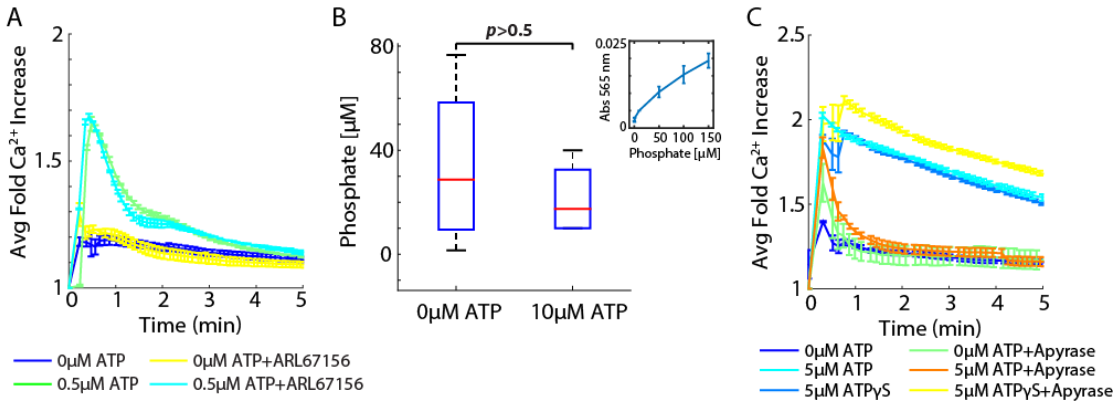

Figure 2.5. Extracellular ATP degradation does not influence Ca^{2+} activation. Ca^{2+} activation measured by genetically encoded biosensor RGECO. A. Addition of 200µM of the ectonucleotidase inhibitor ARL67156 does not increase Ca^{2+} activation by ATP in MCF-10A cells. (Error bars indicate SEM, n=3). B. Extracellular phosphate measurements after addition of 10µM ATP shows no difference when compared to 0µM. Inset shows phosphate standard curve. (Error bars indicate standard deviation, n=3, *p*-value determined by t-test). C. Ca^{2+} activation by ATP decreases in the presence of the ATP scavenger apyrase (5U). However, Ca^{2+} activation by the nonhydrolyzable ATP variant ATPγS does not decrease in the presence of apyrase (Error bars indicate SEM, n=3).

Amplifying Wave: ATP-induced ATP release does not propagate the Ca^{2+} wave

After determining that the Ca^{2+} wave forms using extracellular stimulus independent of ATP degradation, we determined whether an Amplifying Wave mechanism plays a role in forming the Ca^{2+} wave. That is, does ATP activation initiate the release of ATP to bind extracellular receptors on neighboring cells to propagate the Ca^{2+} response? Prior work has suggested that ATP induces the release of additional ATP from cells (ATP-induced ATP release) [162,164–166]. We first determined whether ATP-induced ATP release is required for ATP mediated Ca^{2+} activation. We perturbed cells with the nonhydrolyzable ATP variant ATPγS in the presence and absence of the ATP scavenger apyrase (Figure 5C). ATPγS activates a Ca^{2+} response in cells similarly to ATP. In the presence of apyrase, any additional release of ATP is hydrolyzed without affecting ATPγS. Although Ca^{2+} activation by ATPγS in the presence of apyrase shows a statistically significant but small magnitude increase compared to stimulation by ATPγS alone, apyrase does not deplete Ca^{2+} activation in cells when perturbed with ATPγS as it does with ATP. If ATP did induce ATP release, apyrase should deplete Ca^{2+} activation by ATPγS, not increase it, therefore, if an active propagation mechanism exists, cells do not release ATP to activate neighboring cells. The small increase in Ca^{2+} response to ATPγS in the presence of apyrase may be due to other mechanisms not studied here.

While we saw no evidence for ATP-induced ATP release, it is possible that ATP induces the release of another molecule that propagates the Ca^{2+} wave. We verified the presence of an active release mechanism by measuring the spatial Ca^{2+} activation patterns. Since Ca^{2+} response to wounding is ATP-dependent (Figure 3), we simulated wounding using a photoactivated ATP to ensure we were only measuring Ca^{2+} response according to ATP release and to simplify the measurement (NPE-caged ATP) (Figure 6). In this assay, UV light

illumination releases ATP at the site of illumination. We used NPE-caged ATP in combination with a photoactivated fluorescein, CMNB-caged carboxyfluorescein (caged FITC), such that the free ATP and free FITC were released in the same area at the same time. We then compared the spatial activation of Ca^{2+} in the surrounding cells with the diffusion pattern of FITC in a flow-free environment (Figure 6A, B). Cells were plated in long Ibidi channels of 400μm height to capture the full length of response and that released ATP stayed close to the cells. NPE-caged ATP and caged FITC have similar molecular weights (700.3 g/mol and 826.8 g/mol, respectively). Therefore, the respective molecules will have similar diffusion rates. We reasoned that if an active propagation mechanism exists, the spatial distance of Ca^{2+} activation will extend beyond the diffusion pattern of caged FITC. One port of the channel was sealed prior to uncaging to create a convection-free environment that ensured any response was not due to flow. However, we saw that the Ca^{2+} activation pattern and the caged FITC diffusion pattern are the same in an epithelial monolayer (Figure 6A, B). This indicates that an active propagation mechanism is not responsible for the Ca^{2+} wave but instead points to a Release and Diffusion mechanism.

Release and Diffusion: ATP passively creates a Ca^{2+} gradient following wounding

The similar patterns created by FITC diffusion and the Ca^{2+} wave indicate that a Release and Diffusion mechanism may be responsible for Ca^{2+} wave activation. That is, the initial release of ATP from wounded cells diffuses out from the wound to activate neighboring cells. However, other mechanisms may account for these matching patterns. One potential explanation may be that ATP interacts with cells (by binding/releasing to/from extracellular receptors) to form an activation pattern similar to diffusion. In order to determine the presence of an ATP/cellular interaction mechanism, we again used NPE-caged ATP to release ATP from a point source and measured the Ca^{2+} activation patterns over time and space (Figure

6C). In order to maintain a convection-free environment, the NPE-caged ATP solution was made in a 1% agarose solution that solidified on top of cells prior to uncaging. This way, any Ca^{2+} response from ATP would not be due to flow in the well. Measurements were performed in wells t easily add the agarose solution on top of the cells.

We first determined whether Ca^{2+} activation rates changed in the presence (no scratch) or absence (scratch) of cells (Figure 6D). If ATP/cellular interaction takes place, then the first response time of cells after the scratch will differ from the response time of cells at the same distance from the site of uncaging without the scratch. Because scratch wounds also elicit a

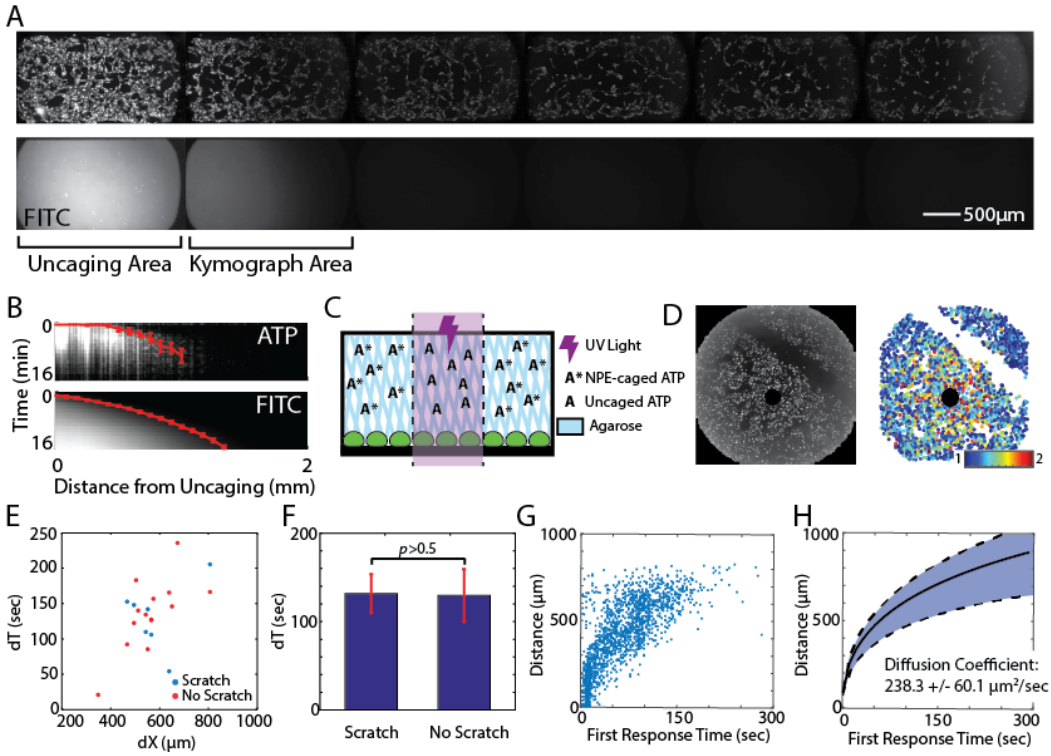

Figure 2.6. The Ca^{2+} wave propagates by ATP diffusion. A. Photoactivated ATP (NPE-caged ATP) and FITC (CMNB-caged carboxyfluorescein) are uncaged using UV light in the area labeled "uncaging region". The Ca^{2+} wave, as measured by the genetically encoded biosensor RGECO (top), travels the same distance as uncaged FITC (bottom) in the absence of any flow at 16 minutes after uncaging. Each side of the channel was taped and allowed to set for 30 minutes to create a flow-free environment. B. Kymograph of region indicated in Figure 6A showing Ca^{2+} activation and uncaged FITC according to time and distance from uncaging. Red line indicates average time of first response per binned distance from the uncaging site. Error bars indicate standard deviation of average fluorescence. C. Spatially activating cells with ATP in a flow-free environment. An NPE-caged ATP solution is made in 1% agarose and added to cells prior to uncaging. After the agarose has solidified (~10 minutes), a UV light shines on a specific area of the well to release the caged ATP. This spatial increase of ATP concentration mimics ATP released from a wound source. D. The time required for the Ca^{2+} wave to cross empty space (scratched) is measured following photoactivated ATP release (black circle). Left: Raw maximum projection of Ca^{2+} response (measured by RGECO) in MCF-10A cells. Right: Maximum Ca^{2+} projection where each circle represents a cell and the color indicates fold Ca^{2+} increase (colorbar). E. The time required for the Ca^{2+} wave to cross a specific distance (dX) in the presence (no scratch, red) or absence (scratch, blue) of cells is measured by the difference between the time a cell first responds to ATP at the distance farther away from the uncaging site and the distance closer to the uncaging site (dT). F. The Ca^{2+} wave takes the same amount of time to traverse a specific distance in the presence (no scratch) or absence (scratch) of cells (p>0.5, t-test, n=7). G. The distance of each cell according to the time each cell first shows Ca^{2+} activation above a threshold following ATP uncaging (no scratch). H. Propagation of the Ca^{2+} wave according to the first response following ATP uncaging follows a pattern best fit by diffusion. The cellular Ca^{2+} response following ATP uncaging from several wells, like the well shown in Figure 6G, are averaged for binned distances following ATP release. Data are fit according to *ATP Diffusion Fitting* under Materials and Methods to find the diffusion coefficient. The diffusion coefficient that best describes the fitted data is 238.3 +/- 60.1 μm^2/sec (SEM, n=3).

Ca^{2+} response in the neighboring healthy cells, we made the scratch more than 2 hours before the experiment to allow Ca^{2+} levels to reset to normal levels. In addition, we saw no difference in Ca^{2+} response between scratched and non-scratched wells after uncaging NPE-caged ATP (data not shown). We then measured the time of first Ca^{2+} response for each cell following uncaging. We quantified the difference in first response times for cells before the scratch (closer to the site of uncaging) and after the scratch (farther from the site of uncaging) to find the difference in Ca^{2+} response times (dT).

We used this same method for cells at similar distances from the uncaging site but without a scratch as an internal control and compared the dTs of Ca^{2+} response time for cells with and without a scratch. We found no difference in the dT of Ca^{2+} response time for cells at the same distances from the site of ATP uncaging despite the presence or absence of a scratch (Figure 6E, F, Supplemental Figure S3). This indicates that ATP does not interact with cells during the spread of the Ca^{2+} wave. Taken together, the evidence above indicates that there is no active mechanism required to form the Ca^{2+} wave gradient following wounding in an epithelial monolayer of cells. However, we see that the wave forms using extracellular stimulation. Without an activation mechanism, we next tested whether a simple Release and Diffusion model explains the propagation of the Ca^{2+} wave. Using our NPE-caged ATP method (Figure 6C), we found the time that each cell first responds to ATP according to its distance from the source (Figure 6G). We then sorted the time for first Ca^{2+} response into bins according to distance from the uncaging site and found that the pattern resembles a square root, similar to the pattern of molecules diffusing from a point source (Figure 6H). Considering the diffusion of ATP from a single point, we fit our Ca^{2+} response data and calculated a diffusion coefficient of 238.3 (+/-60.1) μm^2/sec. This value close resembles literature reported ATP diffusion coefficient values of ~300 μm^2/sec [159].

Overall, we conclude that a simple ATP Release and Diffusion model is responsible for forming the Ca^{2+} wave. In a Release and Diffusion model, ATP released from wounded cells quickly diffuses from the site of wounding to activate Ca^{2+} response in the surrounding healthy cells in an epithelial monolayer.

Discussion

Here we investigate the underlying mechanism responsible for propagation of Ca^{2+} activation from a wound. Multiple mechanisms have been proposed for wound-induced Ca^{2+} waves [120,157,173–175]. These different mechanisms can be classified under three architypes: Source and Sink, Amplifying Wave, and Release and Diffusion (Figure 1). Evidence from a combination of pharmacological perturbations and quantitative measurements of Ca^{2+} wave propagation contradict key predictions of the Amplifying Wave and Source and Sink models. These contradictions suggest that the Ca^{2+} wave propagates via a simple Release and Diffusion process. Specifically, ATP molecules released from wounded cells diffuse to activate Ca^{2+} in the surrounding healthy cells. The natural dilution of ATP molecules resulting from diffusion forms the Ca^{2+} gradient across space.

Each of the proposed models has features necessary for effective wound response but also come with key limitations. In order to initiate a proper wound response, cells need to know 1. The location of the wound and 2. The magnitude of the wound. Neutrophils, macrophages, and epithelial cells use signals indicating the location of the wound to find the wound to fight invading pathogens and close the wound. However, this response needs to scale with the magnitude of the wound. A response that is too small results in ineffective healing. A response that is too large can result in excess scarring and even cancer [180–183]. Additionally, this information must be propagated quickly to begin the wound healing process. By definition the Source and Sink model is self-limiting and ensures that the Ca^{2+} response

remains close to the wound. In this model, the response gradient forms when a large amount of initial signal is released (Source) and then hydrolyzed spatially (Sink). This model tightly regulates the ATP propagation distance. Although this tight regulation is necessary to control the spatial response, it can potentially limit how well the Ca^{2+} response gradient scales with wound size. Contrary to the Source and Sink model, the Amplifying Wave model allows Ca^{2+} activation to spread far from the wound source on a realistic timescale. However, signal amplification may result in information loss concerning the magnitude of the wound. Furthermore, although spreading the signals to far distances may be valuable to recruit immune cells, without self-limiting the wave, the spread of information to distances far from wound can initiate an undesired inflammatory response. The Release and Diffusion model contains features desired for a proper wound response mechanism. A Release and Diffusion model utilizes ATP molecules released from wounded cells as DAMPs to spread to the surrounding healthy cells. It spreads information on a short timescale, scales with wound size, and is self-limiting to prevent undesired activation of faraway cells. Furthermore, an ATP Release and Diffusion model is a simple and straightforward mechanism that requires little additional regulation.

Although the three models we investigated here were chosen as representative mechanistic archetypes, it is possible that the overall Ca^{2+} propagation mechanism uses a combination of models. For example, the Amplifying Wave and Source and Sink models could be combined to a fourth mechanism that balances the contributions of ATP secretion and hydrolysis. However, our data does not support such a model. Our experiments utilizing a cell gap or "scratch" to measure the rate of Ca^{2+} response spread are independent of the molecular pathway underlying an active propagating wave. Additionally, although our results point to a Release and Diffusion model as the core propagation mechanism, it is possible that

Amplifying Wave or Source and Sink components act in parallel. Our experimental analysis of Ca^{2+} response propagation did not find any evidence for such parallel mechanisms. If this is the case, any additional components to the core Release and Diffusion model marginally contribute to Ca^{2+} wave propagation.

One key limitation to our result is that our experiments were conducted in an in vitro setting. It is possible that more complex mechanisms occur in vivo. However, the lack of complexity in our model is informative and can direct future research in an in vivo context. It is possible that a 3-dimensional in vivo model, as opposed to the 2-dimensional monolayer in our system, will result in a different response mechanism. Yet, epithelial layers in many organs such as the cornea are very thin and extend to only three cell layers. Therefore, our results provide a good approximation of in vivo geometry. Another important consideration is that the multiple cell types required for wound healing will change the Ca^{2+} wave dynamics and, therefore, the underlying propagation mechanism. Future work quantifying the spatio-temporal dynamics of Ca^{2+} waves in vivo is required to understand how other cell types are involved. It is clear that our model does not capture the full complexity of wound healing in vivo. Yet, the simplicity of a Release and Diffusion model may be beneficial to ensure surrounding cells are alerted quickly. Future work will determine the extent to which a Release and Diffusion model plays a role in the complexity of in vivo wound healing.

Materials and Methods

Ca^{2+} Measurements in MCF-10A Cells

MCF-10A cells were cultured following established protocols [146]. Before plating cells, each surface was first treated with a collagen (Life Technologies), BSA (New England Biolabs), and fibronectin (Sigma-Aldrich) solution in order for cells to completely adhere, according to established methods. In order to maintain a viable environment, cells were

imaged at 32°C and 5% CO_2. All DREADD experiments were conducted in 96-well plates using extracellular hepes buffer (ECB) to reduce background fluorescence (5 mM KCl, 125 mM NaCl, 20 mM Hepes, 1.5 mM $MgCl_2$, and 1.5 mM $CaCl_2$, pH 7.4). All wound imaging was done in MCF-10A assay media [146].

Single-cell Ca^{2+} levels during wounding and DREADD experiments were measured using Fluo-4, AM (ThermoFisher F14201) to prevent overlap of fluorescent wavelengths of DREADD (mCherry, 587/610 nm), Fluo4-AM (494/506 nm), and R-GECO (mApple, 568/592 nm). Cells were loaded with 8μM Fluo-4, AM, 1X PowerLoad (ThermoFisher P10020), 2.5mM probenecid (P36400), and 20μM Hoechst for 30 minutes at room temperature in ECB. Cells were washed with ECB to remove any remaining extracellular dye. All other Ca^{2+} measurements were conducted using the genetically encoded fluorescent biosensor R-GECO [124,125].

Wounding Device Design, Fabrication, and Wounding Assay

Master molds for the microfluidics based wounding device were created using silicon wafers and layer-by-layer photolithography using established methods [147]. A separate mold for both the air layer and cell layer were made using negative photoresists and masks. Chips were made by pouring uncured polydimethylsiloxane (PDMS) onto each mold, allowing the PDMS to harden, and bonding the layers together and subsequently to a glass slide. Cells were loaded into the device through the inlet port using a 20G needle. During wounding the outlet port was plugged using tape and the inlet port held a reservoir of media to prevent evaporation in the chamber. Wounding was accomplished by increasing the air pressure in the top layer of the device until the pillar made contact with the bottom of the device after which the air pressure was released to raise the pillar back up. Cells were loaded in to the wounding device at a density of 15,000,000 cells/mL using a 20G needle. Following trypsinization and

resuspension, cells were put on ice to prevent aggregation. Two o-rings were attached to the device surrounding both the inlet and outlet ports for media reservoirs using a thin film of vacuum grease. Wounding devices were kept in an empty pipet box filled with water to prevent media evaporation. Cells were allowed to adhere for 18-24 hours before wounding.

Ca^{2+} activation by DREADD

Cells were plated at a density of 2,000,000 cells/100mm plate and allowed to adhere overnight. Cells were transfected with the Gq-coupled DREADD HA-tagged hM3D with an mCherry tag using a 3:1 ratio of FuGene HD (Promega) to DNA and allowed to incubate overnight [127]. In order to measure the impact of activating a single-cell, non-transfected cells were mixed with DREADD-transfected cells at ratios of 1:0, 1:1, 1:2, 1:5, 1:7, and 0:1 (non-transfected:DREADD) and plated in 96-well plates at a density of 30,000 cells/well. The following day, cells were loaded with 1μM Hoechst dye for nuclear imaging for 30 minutes for cell segmentation purposes and Fluo-4, AM to measure Ca^{2+} response. 5μM clozapine-N-oxide (CNO) (Enzo Life Sciences) was added to each well to specifically activate DREADD cells.

Manipulating extracellular ATP levels

Two methods were used to manipulate extracellular ATP: 1. Inhibition of ectonucleotideases with ARL67156 and 2. ATP hydrolysis with apyrase. Cells were plated in 96-well plates at a density of 30,000 cells/well and allowed to adhere overnight. Cells were incubated with 200μM ARL67156 for 1 hour after which 0.5μM of ATP was added to the well. Extracellular ATP was hydrolyzed by adding 5U of apyrase (Sigma A7646) to the well prior to the addition of 5μM ATP or ATPγS (Tocris 4080). In the wounding device, 5U of apyrase was added to the inlet port just before sealing off the second port to ensure that the

apyrase stayed in the cell chamber. Cells were imaged in FluoBrite DMEM media (ThermoFisher A1896701) with the components necessary for MCF-10A assay media added.

Extracellular phosphate measurement

Extracellular phosphate was measured using the PiPer Phosphate Assay Kit (P22061, Thermo Fisher) using the provided protocol. Cells were perturbed with either 0μM or 10μM ATP and allowed to sit for 5 minutes to capture full Ca^{2+} activation. A portion of the media was taken from the wells and used for the PiPer phosphate assay. Absorbance was measured on a plate reader at 565nm.

Spatial measurements of the Ca^{2+} wave

MCF-10A cells were plated in coated Ibidi μ-Slide $VI^{0.1}$ chips by adding 20μL of a cellular solution with a density of $1x10^6$ cells/mL to each channel of the μ-Slide. Cells were allowed to settle for 1 hour after which each well was filled with MCF-10A assay media [146]. Cells were allowed to adhere overnight. In order to measure the distance of Ca^{2+} wave response, we used 1mM NPE-caged ATP (ThermoFisher A1048) and 10mM CMNB-caged fluorescein (ThermoFisher F7103). NPE-caged ATP and CMNB-caged fluorescein were uncaged in specific regions by shining UV light on the region for 20 seconds. Enough NPE-caged ATP solution was added to the channel to partially fill each well. Each well was taped and allowed to sit for >30 minutes to stop flow through the channel.

All other NPE-caged ATP experiments were done in a 96-well plate in an agarose solution to prevent any convection during uncaging and imaging. NPE-caged ATP solutions were made in a 1% agarose solution and allowed to solidify for 10 minutes at room temperature prior to uncaging. Each well was exposed with UV light for 10 seconds to uncage NPE-caged ATP. To determine whether the Ca^{2+} wave could cross empty space, cells were seeded in a 96-well plate at a density of 30,000 cells/well and allowed to adhere overnight.

Cell monolayers were scratched using a 2µL pipet tip to create empty space. Scratches were done >4 hours prior to imaging to give Ca^{2+} levels adequate time to return to basal levels. A 1% agarose solution containing 10µM NPE-caged ATP was added to each well and allowed to solidify for 10 minutes at room temperature. Each well was exposed with UV light for 10 seconds to uncage NPE-caged ATP.

ATP Diffusion Fitting

We considered the diffusion of ATP from a single point to its surrounding neighbors to find the diffusion coefficient *D* of the molecule responsible for Ca^{2+} wave propagation following ATP release. We considered a 2D-like geometry where cylindrical cells, each of height h_c and radius ρ, grow in a chamber of total h_f height. We simplify the below analysis by approximating the cell monolayer geometry to a series of "cell cylinders". We also consider the number of molecules released from a cell N_r, the number of molecules needed for detection N_d, and the total integration time T. The key results of the required integration time are similar for other comparable geometries (data not shown). Under these conditions one could write the analytical solution of the diffusion equations:

(1) $$C(r,t) = \frac{\mathrm{N_r}}{h_f \cdot 4D\pi t} \mathrm{e}^{-\frac{r^2}{4Dt}}$$

Where $C(r,t)$ is the concentration of ATP for distance *r* and time *t*. For a neighboring cell to respond to this paracrine signal, a critical number of molecules N_d need to reach the volume surrounding the cell. We assume that a cell "senses" a volume comparable to the volume of a cell itself. For a cylindrical cell of area $\pi\rho^2$ and height h_c the critical concentration required for cellular response will be:

(2) $$C_{detect} = \frac{N_d}{h_c \pi \rho^2}$$

This is simply the required number of molecules divided by the cell volume. Combining equations 1 and 2 we can solve for the distance and time of where the critical concentration will be reached. Solving for distance we get that

(3) $$r_{detect} = 2\sqrt{Dt \ln\left(\frac{\rho^2 h_c N_r}{4DtN_d h_f}\right)}$$

Using the time of first response for each cell with is corresponding distance from the ATP source, we used equation (3) to fit the experimental data to get the ATP diffusion coefficient.

Imaging and Image Analysis

Imaging was accomplished using a Nikon Plan Apo λ 10X/0.45 objective with a 0.7x demagnifier and Nikon Eclipse Ti microscope with a sCMOS Zyla camera. All imaging was accomplished using custom automated software written using MATLAB and Micro-Manager [148]. Image analysis was accomplished using a custom MATLAB code published previously [109] (Supplemental Figure S4).

Acknowledgements

The work was supported by GM111404, EY024960 (RW), and a training grant (GM007240) for LNH.

Chapter 2 in full is a reprint of the material in press for publication as it appears in Handly, L.N.; Wollman, R. Wound induced Ca^{2+} wave propagates through a simple Release

and Diffusion mechanism. Mol. Biol. Cell. 2017, In Press. The dissertation author is the first author on this paper.

Supplemental Figures

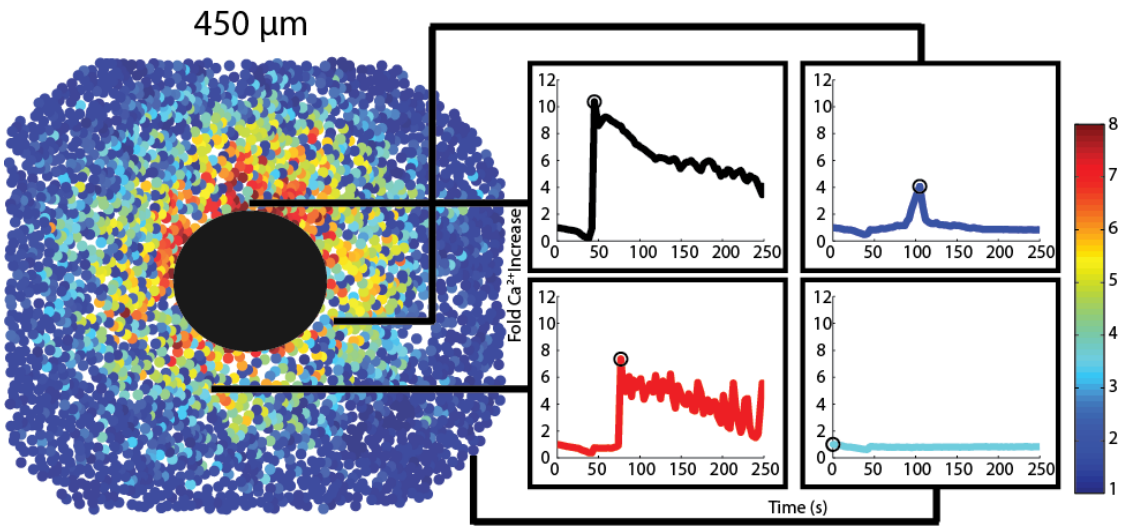

Supplemental Figure S2.1. Maximum projection of single-cell response interpretation. Throughout the manuscript, the maximum projection of cellular responses are depicted where each circle represents a single-cell. Each single-cell circle corresponds to a time-series and the color indicates the maximum value in that time-series (right) as set by a colorbar. The black circle represents the point of ATP release, either by wounding or uncaging.

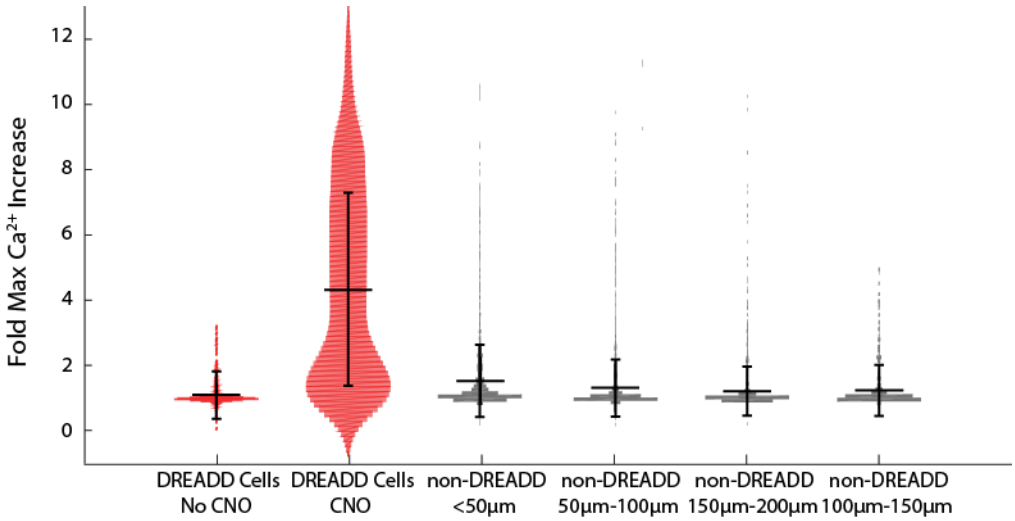

Supplemental Figure S2.2. Ca^{2+} response to CNO in DREADD and non-DREADD expressing cells. Data from Figure 4B, C are categorized according to distance from the DREADD cell. The spread of maximum Ca^{2+} response for DREADD (red) and non-DREADD (gray) expressing cells is shown according to distance from the DREADD cell indicating that only DREADD cells have a Ca^{2+} response with the addition of CNO.

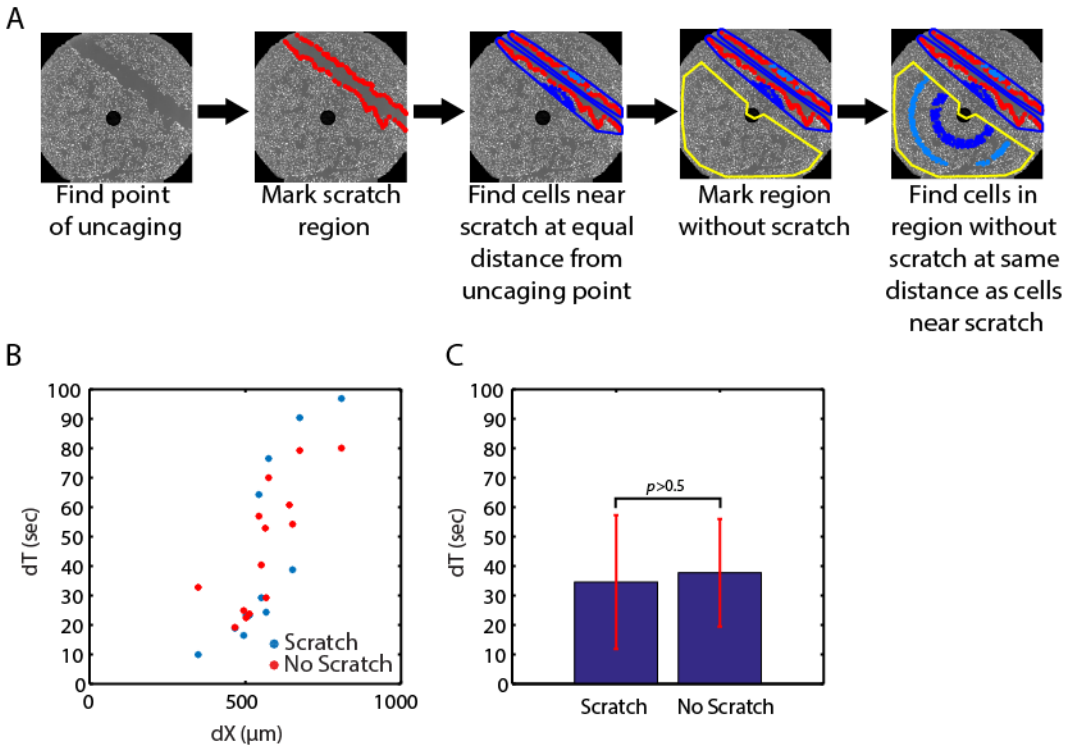

Supplemental Figure S2.3. ATP does not bind to cells to produce the Ca^{2+} gradient. Assays to measure whether ATP binds to cells to produce the Ca^{2+} gradient measures the time of Ca^{2+} response following ATP uncaging in the presence (no scratch) and absence (scratch) of cells. A. From left to right, the point of uncaging is marked with a black circle. Then the cells surrounding the scratch are labeled (red). Next, cells at similar distances from the uncaging point before and after the scratch are marked (dark blue and light blue). A region without a scratch is marked (yellow) as an internal control to compare the time of first response in the presence of cells. Cells at the same distances as the cells surrounding the scratch are marked in the non-scratch region (dark blue and light blue). B & C. The same assay as Figure 6E & F for uncaged FITC. As expected, uncaged FITC, which does not bind to cells, takes the same amount of time to traverse a region with (no scratch) and without (scratch) cells.

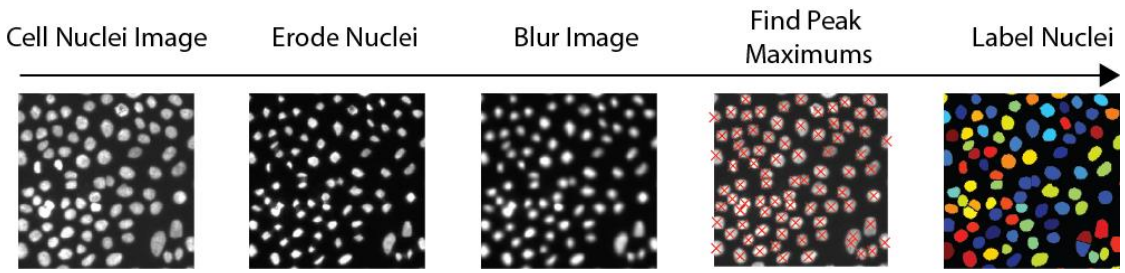

Supplemental Figure S2.4. Image Analysis Method. From left to right. Cells are stained with the nuclear dye Hoechst. Nuclei are eroded to find the points of maximum fluorescence in each cell. Next the image is blurred to reduce noise and leave only a single peak per nuclei. Using the blurred image, the maximum peak for each nuclei is identified which is then labeled as the nucleus of the cell.

CHAPTER 3

SpaSeq: A method to measure the spatio-temporal differential gene expression following a wound

Introduction

Patterns formed by wound response signals that tell neighboring healthy cells how to respond to a wound is reminiscent of a developmental program which determines the fate of every cell within an organism. *Drosophila* embryogenesis, a classic developmental biology model, first showed patterns of gene expression which determine the fate of each cell [184,185]. Similarly, cells surrounding a wound depend on positional information to determine how to respond based on the size of the wound [132].

Just as in development, wound healing relies on multiple steps. As was shown in the first two chapters, transcription-independent paracrine molecules diffuse to activate signaling mechanisms in cells [93,150]. These transcription-independent factors eventually translate into gene expression responsible for the remaining steps of wound healing including recruiting immune cells to fight potential infection, closing the wound through migration and proliferation, and finally the formation of scar tissue [186]. Each of these steps requires turning genetic programs on and off for successful wound closure. For example, cell migration and proliferation must end by the time scar formation begins to prevent keloids or other tumor-like scars.

Previous work has demonstrated differential gene expression following a wound. Pearson et al. showed differences in gene expression at different distances from the wound in *Drosophila* [187]. Additionally, wounded rat cornea epithelial cells and vocal-chords showed gene expression changing over time [188,189]. However, a comprehensive analysis of the genes expressed in both space and time following an epithelial wound has not been done.

Here we present a method we name SpaSeq (Spatial Sequencing) to measure the spatio-temporal genetic wound response in epithelial cells using a combination of photo-convertible proteins, FACS cells sorting, and RNA-Seq.

Results

Creating cellular patterns using photoconvertible proteins

In order to measure the differential gene expression across space and time in response to a wound, we first developed a method to track cells according to their distance from the wound. Here we create cellular patterns using the photoconvertible protein tdEos which transitions from green to red following UV light illumination (Figure 1) [190–192]. By shining light in a ring pattern at different distances from the center of the wound, we create rings with radii of 100μm, 250μm, 450μm, and 650μm. Second, we create a "cell sandwich" by placing a glass slide with cells loaded with pyropheophorbine a methyl ester (PPME) on top of the patterned cells to wound the cells. PPME induces cell death by producing reactive oxygen species (ROS) when cells loaded with PPME are exposed to 660nm light. We shine light only on the center of the monolayer to selectively wound the cells in the middle. Following wounding, we allow the cells to sit for 1, 4, 8, 12, or 24 hours after which the converted red cells are separated from the green cells using FACS. The sorted cells are then sequenced to measuring gene expression at all points in time and space.

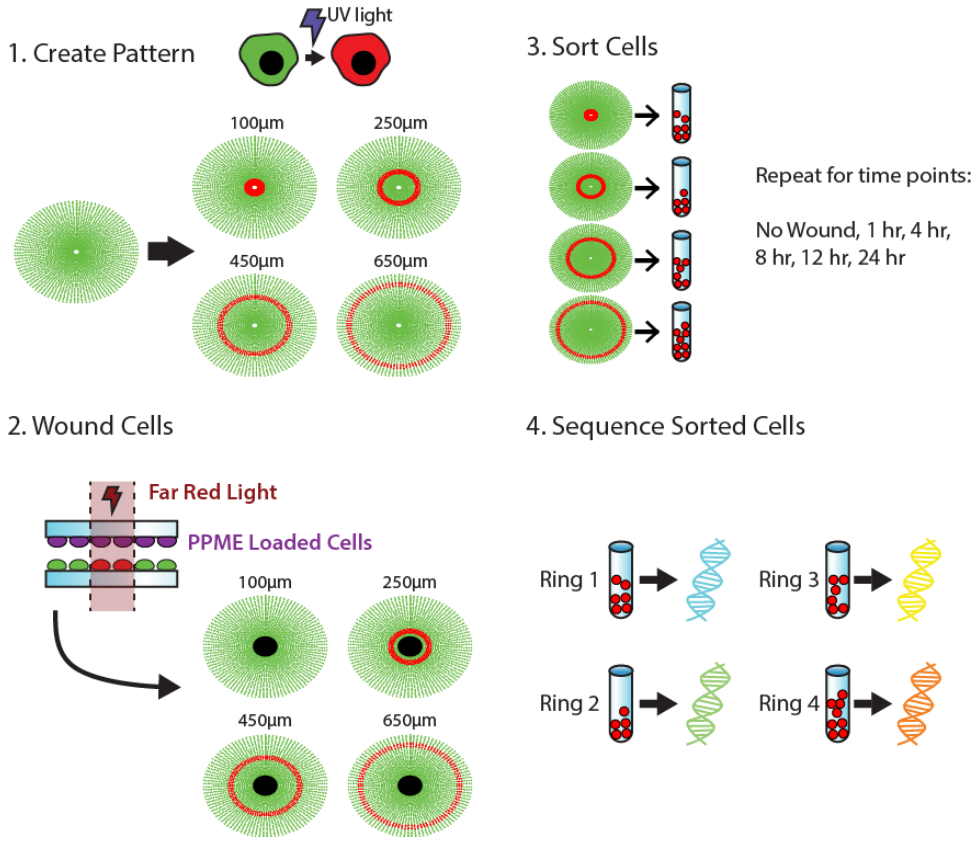

Figure 3.1. Method to measure spatio-temporal gene expression following a wound. Step 1. 405nm light converts tdEos from green to red to create distinct spatial patterns at specified radii of 100µm, 250µm, 450µm, and 650µm away from the center of the well. Step 2. Cells loaded with PPME (purple) are placed on top of the spatially patterned cells (green/red). 660nm light shines on the center of the well to specifically kill the cells in the center of the well. Black circles represent dead cells. Step 3. Cells are allowed to incubate for 1, 4, 8, 12, or 24 hours before removing the glass slide and sorting the cells. Step 4. Sorted cells are sequenced using RNA-Seq to measure the differential gene expression patterns across space and time.

Creating patterns and wounding cells requires a three-day process

The 4-step experimental design outlined in figure 1 requires a three-day process (Figure 2A). On day one, limbal stem cells (LSC) are plated on glass slides with 30 “wells”, each 2mm in diameter, made with the hydrophobic material PTFE (Figure 2B). The small growth area ensures easy separation of the converted cells from non-converted cells during the

later FACS step. Cells are plated at a density of 50,000 cells/mL in 20µL per well and allowed to adhere overnight. Cells are kept in an empty pipet tip box filled with water to prevent media evaporation.

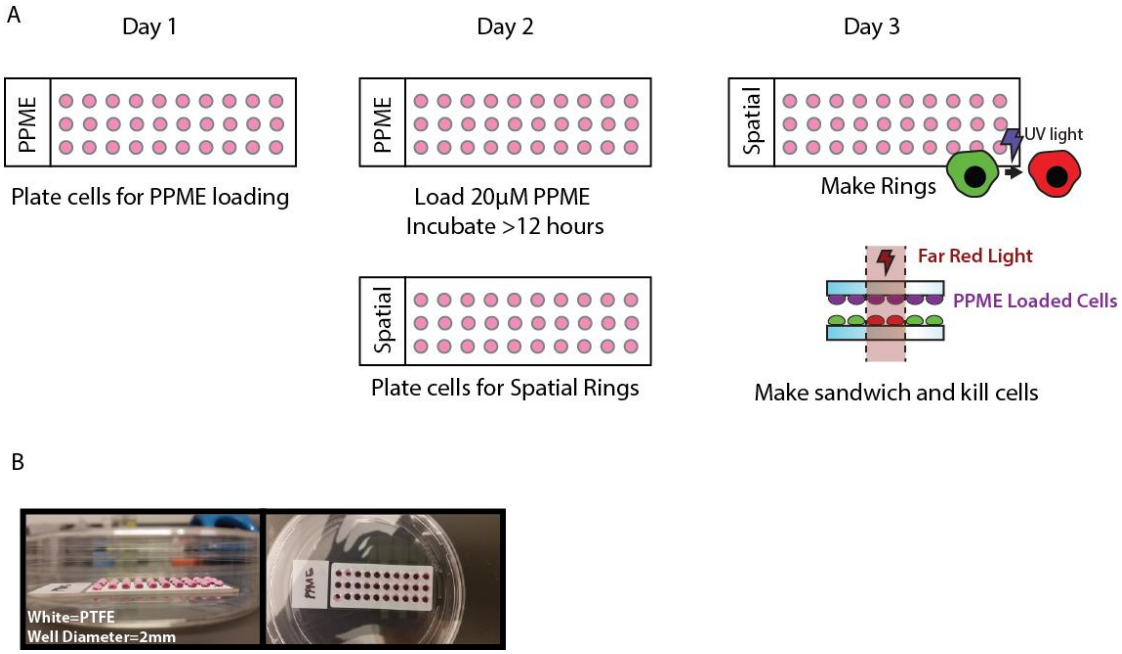

Figure 3.2. SpaSeq workflow. A. The entire SpaSeq process takes three days to plate the cells, load PPME, make the spatial rings, and kill the cells. B. Image of the PTFE coated glass slide. Each well is 2mm in diameter and has a total volume of 20µL.

On day two, the cells plated on day 1 are loaded with 20µM PPME by carefully removing approximately 90% of the media "bubble" so as not to shear the cells (Figure 2B) and adding 20µL of PPME. Cells are allowed to incubate with PPME for a minimum of 12 hours while covered with foil and kept in the dark. LSC cells expressing the photoconvertible protein tdEos for the spatial rings are also plated on day two (Figure 2A) at a density of 200.000 cells/mL in 20µL per well and allowed to adhere overnight.

On day three, we shine a 405nm laser in a specific ring pattern on each of the wells to create the spatial rings on the spatial slide (Figure 2A, Figure 3A). Every well on one slide has

the same ring size since these cells will be trypsinzed and sorted together. The radii of each ring are chosen to cover the well area but ensure adequate separation between the rings (Figure 3A). After the rings are made, the slide with cells loaded with PPME is placed on top of the converted cells to create a cell sandwich. The small volume in each well prevents dilution of any paracrine molecules released during wounding important for signaling [93]. Additionally, the PTFE between each well prevents movement of paracrine molecules between wounds. We use a 660nm light to wound cells in the center of the well (Figure 3B). The sandwich is allowed to incubate for 30 minutes to allow all diffusible molecules to initiate signaling molecules [193]. The sandwich is placed in a media bath to separate the slides without shearing the cells and then the spatial slide is allowed to incubate for 1, 4, 8, 12, or 24 hours.

Following incubation, cells on the spatial slide are removed using 0.05% trypsin and incubated for 15 minutes. Trypsinization is terminated using LSC media and the cells are centrifuged and resuspended in a FACS buffer to remove the trypsin. Cells are stained with DAPI as a dead cell stain, passed through a 35μm cell strainer, and placed on ice. Converted cells (569/581nm Ex/Em) are separated from unconverted cells (506/516nm Ex/Em) with FACS and sorted in 3X TRIzol LS to lyse the cell (Figure 3C) [190]. At this point, RNA can be extracted from cells and stored for future RNA-Seq analysis. The SpaSeq process is repeated for all space and time points to create a comprehensive spatio-temporal profile of gene expression following a wound.

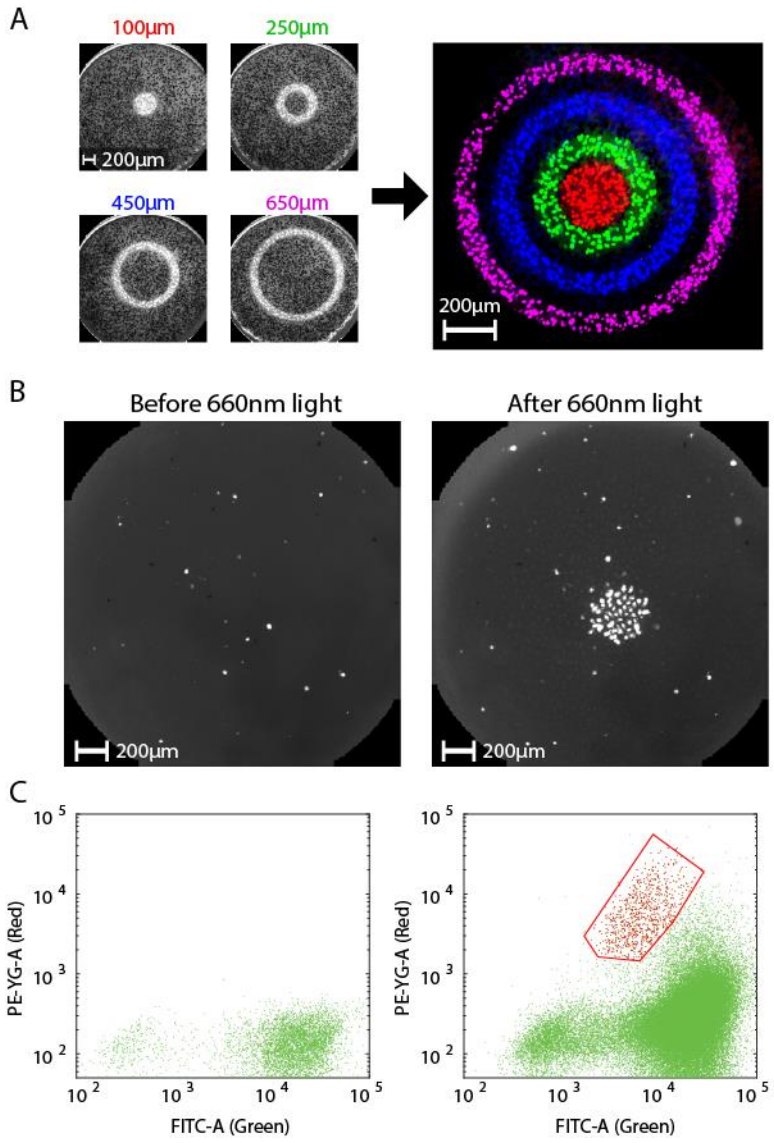

Figure 3.3. SpaSeq spatially separates cells following a wound. A.LSC cells expressing tdEos are specifically converted from green to red to create spatial patterns. Images on left are the ratio of Red to Green image. Image on right shows images from left placed on top of each other. Each ring is distinct from the other. B. Cells loaded with 20µM of PPME are selectively killed with a 660nm laser. Dead cells are marked with Sytox Blue. Left shows dead cells before 660nm light and right shows dead cells after 660nm light. C. Left: FACS sorting of non-converted cells. Right: FACS sorting of cells after conversion. Gated cells in red are converted cells that will be used for sequencing.

Methods

LSC cell culture and manipulation

LSC cells are cultured in media according to the below recipe:

Table 3.1. LSC cell media formula.

Reagent	Stock Conc.	Add Volume	Final Conc.
DMEM	1X	215 mL	
DMEM/F12	1X	215 mL	
FBS	1X	60 ml	
Penicillin Streptomycin	1X	5 ml	
Adenine		5 ml	
EGF	100 ug/ml	50 ul	10 ng/ml
Insulin	4 mg/ml	625 ul	5 ug/ml
Cholera Toxin	1 mg/ml= 0.05 M		10^{-10} M
Hydrocortisone	1 mg/ml	200 uL	0.4 ug/ml
3,3',5-Triiodo-L-Thyronine		1 ml	2×10^{-9} M= 2nM

Media is sterilized through a 0.22μm filter and stored at 4˚C for up to 2 weeks.

All culture dishes, plates, and PTFE glass slides (EMS 63434-02) are coated with 2% Matrigel (Corning 356231) in DMEM for 30 minutes at room temperature. An aliquot of Matrigel is thawed on ice at 4˚C for 2 hours before use.

PPME (Sigma P3787) is dissolved at a concentration of 1mM in ethanol and stored at -20˚C and diluted in LSC media when incubated with cells. To ensure that cells are being killed in the correct area, dead cells are marked with 1μM Sytox Blue (Thermo Fisher S34857).

FACS preparation and separation

Cells are passed through a 35μm mesh filter (Corning 352235) and placed on ice prior to FACS separation. Cells are resuspended in a FACS buffer consisting of 96% PBS, 2% fetal bovine serum, 1% 100X Pen/Strep, and 1% 0.5M EDTA (pH 7.4). Cells are sorted into 3X

TRIzol LS Reagent (ThermoFisher 10296010) which is diluted in water such that the final cell volume occupies less than a third of the total final volume to ensure all cells are immediately lysed upon contact.

Discussion

Here we present a method to measure the spatio-temporal gene response of epithelial cells following a wound. We take advantage of several techniques including photoconvertible proteins, fluorescent microscopy, FACS, and RNA-Seq. Although we present an accessible method to measure the spatio-temporal differential gene expression in wounds, there are technical challenges. For example, cells in the cell sandwich have limited viability due to the small volume of media available. Although previous work shows that wound signals diffuse for 30 minutes, removing the wounded cells from the healthy cells may disturb the wound healing process since wounded cells are not removed from healthy cells this quickly in vivo [193]. Similarly, placing the spatially patterned cells into a media bath following the initial 30-minute incubation may cause artifacts due to diffusion of paracrine molecules. However, these potential artifacts will equally influence all cells in the wound and therefore will not exhibit differential expression.

With additional development, this method has potential to measure the spatio-temporal gene patterns in three-dimensional tissue following a wound. Cells in a three-dimensional tissue, such as a cornea, expressing tdEos can be patterned similarly using high-intensity lasers, dissociated, separated, and sequenced. Furthermore, this method can be adapted to other spatially relevant biological events such as development, immune cell recruitment in cancer, morphogenesis, among other. Overall, this approach provides a novel but simple method to measure the differential gene expression in wounds and other spatially relevant biological contexts.

Acknowledgments

Chapter 3 is a work in collaboration with Anna Pilko and Alon Oyler-Yaniv. The dissertation author is the author of this material.

CONCLUSION

The best part about studying wound healing is that it is easy to explain to any scientist or non-scientist the importance of wound healing. Everyone gets cuts and no one likes them. Even more, wound healing is a regeneration mechanism happening right before our eyes. The importance of understanding wound healing extends beyond healing healthy wounds in healthy individuals, of course. The ability to heal wounds more efficiently has applications for those with autoimmune disorders who are unable to heal quickly or to soldiers in combat who need quick solutions for serious injuries. For these reasons, and more, extensive research has been and continues to be conducted to understand the complex, multi-step process of wound healing.

Although a lot is known about wound healing, less is known about the initial wound response signals. Wounds can take days, weeks, and sometimes even months to heal. However, wound healing begins as soon as the wound occurs. Furthermore, most wounding studies have been conducted at the population level, as noted in the introduction, which cannot account for differences in cellular response of cells at different distances from the wound. Improvements in live-cell imaging, fluorescent biomarkers, and computational modeling have made exploring the initial wound response immediately surrounding the wound in a spatially relevant manner possible.

Using these technologies, I have shown that the initial wound response signal ATP travels using a simple release and diffusion mechanism. Any noise due to the use of a simple mechanism is later filtered out using paracrine communication to maximize the signal to noise ratio. Finally, I have presented a method to determine the differential spatio-temporal gene

expression of epithelial wounds. The combination of these studies provides insight into the wound healing process from the beginning to the end.

It will be interesting to see how the initial wound response signals specifically map to downstream gene responses. Although chapter 3 presents a method to map the genes expressed following wounding, this does not show how the initial molecules such as ATP, Ca^{2+}, and ERK influence the overall gene expression patterns. It will be interesting to see how inhibiting any of these signaling mechanisms impacts the gene expression patterns over time.

One limitation of this work is that all the experiments were conducted using two-dimensional monolayers of cells. Wounding occurs in three-dimensional tissue and uses many cell types in addition to epithelial cells such as neutrophils, macrophages, and fibroblasts to remove dead cells and pathogens. Two-dimensional monolayers, therefore, do not fully replicate the wounding environment. However, as with any model system, the initial advances must be done in simple models before moving to more advanced systems. Improvements in microscopy and biomarkers are allowing more advanced in vivo wound studies [133]. Additionally, advancement in single-cell RNA-Seq will enable understanding how signaling dynamics influence gene expression [194].

Perhaps one of the most exciting things to see will be how these initial signaling mechanisms influence wound healing in vivo. If wound healing begins as soon as the wound occurs, then more efficient wound healing can be achieved with earlier intervention. However, understanding this process will require mapping the signaling dynamics of wound healing to the downstream gene expression for in vivo wounds.

Overall I use new technology to determine how cells talk to each other immediately following a wound in an epithelial monolayer of mammalian cells. I am excited to see if and how this work influences future wound healing discoveries.

REFERENCES

[1] R. Lev Bar-Or, R. Maya, L. a Segel, U. Alon, a J. Levine, M. Oren, Generation of oscillations by the p53-Mdm2 feedback loop: a theoretical and experimental study., Proc. Natl. Acad. Sci. U. S. A. 97 (2000) 11250–11255. doi:10.1073/pnas.210171597.

[2] G. Lahav, N. Rosenfeld, A. Sigal, N. Geva-Zatorsky, A.J. Levine, M.B. Elowitz, U. Alon, Dynamics of the p53-Mdm2 feedback loop in individual cells., Nat. Genet. 36 (2004) 147–50. doi:10.1038/ng1293.

[3] J.E. Purvis, G. Lahav, Encoding and decoding cellular information through signaling dynamics., Cell. 152 (2013) 945–56. doi:10.1016/j.cell.2013.02.005.

[4] S. Tay, J.J. Hughey, T.K. Lee, T. Lipniacki, S.R. Quake, M.W. Covert, Single-cell NF-kappaB dynamics reveal digital activation and analogue information processing., Nature. 466 (2010) 267–71. doi:10.1038/nature09145.

[5] R. Cheong, A. Rhee, C.J. Wang, I. Nemenman, A. Levchenko, Information transduction capacity of noisy biochemical signaling networks., Science. 334 (2011) 354–8. doi:10.1126/science.1204553.

[6] J. Selimkhanov, B. Taylor, J. Yao, A. Pilko, J. Albeck, A. Hoffmann, L. Tsimring, R. Wollman, Systems biology. Accurate information transmission through dynamic biochemical signaling networks., Science. 346 (2014) 1370–3. doi:10.1126/science.1254933.

[7] a a Cohen, N. Geva-Zatorsky, E. Eden, M. Frenkel-Morgenstern, I. Issaeva, a Sigal, R. Milo, C. Cohen-Saidon, Y. Liron, Z. Kam, L. Cohen, T. Danon, N. Perzov, U. Alon, Dynamic proteomics of individual cancer cells in response to a drug., Science. 322 (2008) 1511–6. doi:10.1126/science.1160165.

[8] R.H.N. Editors, J.M. Walker, Fluorescent Protein-Based Biosensors, 1071 (2014) 1–16. doi:10.1007/978-1-62703-622-1.

[9] V. Sample, S. Mehta, J. Zhang, Genetically encoded molecular probes to visualize and perturb signaling dynamics in living biological systems., J. Cell Sci. 127 (2014) 1151–60. doi:10.1242/jcs.099994.

[10] K.M. Dean, A.E. Palmer, Advances in fluorescence labeling strategies for dynamic cellular imaging., Nat. Chem. Biol. 10 (2014) 512–23. doi:10.1038/nchembio.1556.

[11] E.A. Lemke, C. Schultz, Principles for designing fluorescent sensors and reporters., Nat. Chem. Biol. 7 (2011) 480–483. doi:10.1038/nchembio.620.

[12] J. Goedhart, D. von Stetten, M. Noirclerc-Savoye, M. Lelimousin, L. Joosen, M.A. Hink, L. van Weeren, T.W. Gadella Jr., A. Royant, Structure-guided evolution of cyan fluorescent proteins towards a quantum yield of 93%, Nat Commun. 3 (2012) 751. doi:10.1038/ncomms1738.

[13] B.T. Bajar, E.S. Wang, A.J. Lam, B.B. Kim, C.L. Jacobs, E.S. Howe, M.W. Davidson, M.Z. Lin, J. Chu, Improving brightness and photostability of green and red fluorescent proteins for live cell imaging and FRET reporting, Sci. Rep. 6 (2016) 20889. doi:10.1038/srep20889.

[14] N.C. Shaner, P.A. Steinbach, R.Y. Tsien, A guide to choosing fluorescent proteins., Nat. Methods. 2 (2005) 905–909. doi:10.1038/nmeth819.

[15] J.A. Ubersax, J.E. Ferrell Jr, Mechanisms of specificity in protein phosphorylation, Nat. Rev. Mol. Cell Biol. 8 (2007) 530–541. doi:10.1038/nrm2203.

[16] A.Y. Ting, K.H. Kain, R.L. Klemke, R.Y. Tsien, Genetically encoded fluorescent reporters of protein tyrosine kinase activities in living cells., Proc. Natl. Acad. Sci. U. S. A. 98 (2001) 15003–15008. doi:10.1073/pnas.211564598.

[17] J. Zhang, Y. Ma, S.S. Taylor, R.Y. Tsien, Genetically encoded reporters of protein kinase A activity reveal impact of substrate tethering., Proc. Natl. Acad. Sci. U. S. A. 98 (2001) 14997–15002. doi:10.1073/pnas.211566798.

[18] J. Zhang, C.J. Hupfeld, S.S. Taylor, J.M. Olefsky, R.Y. Tsien, Insulin disrupts beta-adrenergic signalling to protein kinase A in adipocytes, Nature. 437 (2005) 569–573. doi:nature04140 [pii]\r10.1038/nature04140.

[19] M.D. Allen, J. Zhang, Subcellular dynamics of protein kinase A activity visualized by FRET-based reporters, Biochem. Biophys. Res. Commun. 348 (2006) 716–721. doi:10.1016/j.bbrc.2006.07.136.

[20] C. Depry, M.D. Allen, J. Zhang, Visualization of PKA activity in plasma membrane

microdomains., Mol. Biosyst. 7 (2011) 52–58. doi:10.1039/c0mb00079e.

[21] A.J. Lam, F. St-Pierre, Y. Gong, J.D. Marshall, P.J. Cranfill, M. a Baird, M.R. McKeown, J. Wiedenmann, M.W. Davidson, M.J. Schnitzer, R.Y. Tsien, M.Z. Lin, Improving FRET dynamic range with bright green and red fluorescent proteins., Nat. Methods. 9 (2012) 1005–12. doi:10.1038/nmeth.2171.

[22] N.-N. Aye-Han, M.D. Allen, Q. Ni, J. Zhang, Parallel tracking of cAMP and PKA signaling dynamics in living cells with FRET-based fluorescent biosensors., Mol. Biosyst. 8 (2012) 1435–40. doi:10.1039/c2mb05514g.

[23] K.J. Herbst, M.D. Allen, J. Zhang, Luminescent kinase activity biosensors based on a versatile bimolecular switch, J. Am. Chem. Soc. 133 (2011) 5676–5679. doi:10.1021/ja1117396.

[24] X.Y. Liu S, Zhang J, FRET-based direct detection of dynamic protein kinase A activity on the sarcoplasmic reticulum in cardiomyocytes., Biochem. Biophys. Res. Commun. 404 (2011) 581–586. doi:10.1016/j.bbrc.2010.11.116.

[25] J.D. Violin, J. Zhang, R.Y. Tsien, A.C. Newton, A genetically encoded fluorescent reporter reveals oscillatory phosphorylation by protein kinase C, J. Cell Biol. 161 (2003) 899–909. doi:10.1083/jcb.200302125.

[26] M.T. Kunkel, Q. Ni, R.Y. Tsien, J. Zhang, A.C. Newton, Spatio-temporal Dynamics of Protein Kinase B/Akt Signaling Revealed by a Genetically Encoded Fluorescent Reporter, J. Biol. Chem. 280 (2005) 5581–5587. doi:10.1074/jbc.M411534200.

[27] M.T. Kunkel, A. Toker, R.Y. Tsien, A.C. Newton, Calcium-dependent Regulation of Protein Kinase D Revelaed by a Genetically Encoded Kinase Activity Reporter, J. Biol. Chem. 282 (2007) 6733–6742. doi:10.1074/jbc.M608086200.

[28] M. Fosbrink, N.-N. Aye-Han, R. Cheong, A. Levchenko, J. Zhang, Visualization of JNK activity dynamics with a genetically encoded fluorescent biosensor., Proc. Natl. Acad. Sci. U. S. A. 107 (2010) 5459–64. doi:10.1073/pnas.0909671107.

[29] C.D. Harvey, A.G. Ehrhardt, C. Cellurale, H. Zhong, R. Yasuda, R.J. Davis, K. Svoboda, A genetically encoded fluorescent sensor of ERK activity., Proc. Natl. Acad. Sci. U. S. A. 105 (2008) 19264–9. doi:10.1073/pnas.0804598105.

[30] N. Komatsu, K. Aoki, M. Yamada, H. Yukinaga, Y. Fujita, Y. Kamioka, M. Matsuda, Development of an optimized backbone of FRET biosensors for kinases and GTPases., Mol. Biol. Cell. 22 (2011) 4647–56. doi:10.1091/mbc.E11-01-0072.

[31] J.G. Albeck, G.B. Mills, J.S. Brugge, Frequency-Modulated Pulses of ERK Activity Transmit Quantitative Proliferation Signals., Mol. Cell. 49 (2013) 249–61. doi:10.1016/j.molcel.2012.11.002.

[32] B. Sparta, M. Pargett, M. Minguet, K. Distor, G. Bell, J.G. Albeck, Receptor level mechanisms are required for epidermal growth factor (EGF)-stimulated extracellular signal-regulated kinase (ERK) activity pulses, J. Biol. Chem. 290 (2015) 24784–24792. doi:10.1074/jbc.M115.662247.

[33] S. Regot, J.J. Hughey, B.T. Bajar, S. Carrasco, M.W. Covert, High-sensitivity measurements of multiple kinase activities in live single cells., Cell. 157 (2014) 1724–34. doi:10.1016/j.cell.2014.04.039.

[34] M.H. Spitzer, G.P. Nolan, Mass Cytometry: Single Cells, Many Features, Cell. 165 (2016) 780–791. doi:10.1016/j.cell.2016.04.019.

[35] A.P. Frei, F.A. Bava, E.R. Zunder, W.E. Hsieh, Y. Chen, G.P. Nolan, P.F. Gherardini, Highly multiplexed simultaneous detection of RNAs and proteins in single cells, 13 (2016). doi:10.1038/nmeth.3742.

[36] J.H. Levine, E.F. Simonds, S.C. Bendall, K.L. Davis, E.D. Amir, M.D. Tadmor, O. Litvin, H.G. Fienberg, A. Jager, E.R. Zunder, R. Finck, A.L. Gedman, I. Radtke, J.R. Downing, D. Pe'er, G.P. Nolan, Data-Driven Phenotypic Dissection of AML Reveals Progenitor-like Cells that Correlate with Prognosis, Cell. 162 (2015) 184–197. doi:10.1016/j.cell.2015.05.047.

[37] S. Krishnaswamy, M.H. Spitzer, M. Mingueneau, S.C. Bendall, O. Litvin, E. Stone, D. Pe'er, G.P. Nolan, Conditional density-based analysis of T cell signaling in single-cell data., Science. (2014). doi:10.1126/science.1250689.

[38] M. Mingueneau, S. Krishnaswamy, M.H. Spitzer, S.C. Bendall, E.L. Stone, S.M. Hedrick, D. Pe'er, D. Mathis, G.P. Nolan, C. Benoist, Single-cell mass cytometry of TCR signaling: amplification of small initial differences results in low ERK activation in NOD mice., Proc. Natl. Acad. Sci. U. S. A. 111 (2014) 16466–71. doi:10.1073/pnas.1419337111.

[39] R. Wollman, N. Stuurman, High throughput microscopy: from raw images to discoveries., J. Cell Sci. 120 (2007) 3715–22. doi:10.1242/jcs.013623.

[40] J.E. Sero, H.Z. Sailem, R.C. Ardy, H. Almuttaqi, T. Zhang, C. Bakal, Cell shape and the microenvironment regulate nuclear translocation of NF- j B in breast epithelial and tumor cells, (2015).

[41] B. Snijder, R. Sacher, P. Rämö, E.-M. Damm, P. Liberali, L. Pelkmans, Population context determines cell-to-cell variability in endocytosis and virus infection., Nature. 461 (2009) 520–3. doi:10.1038/nature08282.

[42] R.J. Steininger, S. Rajaram, L. Girard, J.D. Minna, L.F. Wu, S.J. Altschuler, On comparing heterogeneity across biomarkers, Cytom. Part A. 87 (2015) 558–567. doi:10.1002/cyto.a.22599.

[43] D.K. Singh, C.-J. Ku, C. Wichaidit, R.J. Steininger, L.F. Wu, S.J. Altschuler, Patterns of basal signaling heterogeneity can distinguish cellular populations with different drug sensitivities, Mol. Syst. Biol. 6 (2010) 1–10. doi:10.1038/msb.2010.22.

[44] L.-H. Loo, L.F. Wu, S.J. Altschuler, Image-based multivariate profiling of drug responses from single cells., Nat. Methods. 4 (2007) 445–453. doi:10.1038/nmeth1032.

[45] Z.E. Perlman, M.D. Slack, Y. Feng, T.J. Mitchison, L.F. Wu, S.J. Altschuler, Multidimensional drug profiling by automated microscopy., Science. 306 (2004) 1194–8. doi:10.1126/science.1100709.

[46] A.A. Dima, J.T. Elliott, J.J. Filliben, M. Halter, A. Peskin, J. Bernal, M. Kociolek, M.C. Brady, H.C. Tang, A.L. Plant, Comparison of segmentation algorithms for fluorescence microscopy images of cells, Cytom. Part A. 79 A (2011) 545–559. doi:10.1002/cyto.a.21079.

[47] T. Wittenberg, Review of free software tools for image analysis of fluorescence cell micrographs, 257 (2014) 39–53. doi:10.1111/jmi.12184.

[48] N. Chenouard, I. Smal, F. de Chaumont, M. Maška, I.F. Sbalzarini, Y. Gong, J. Cardinale, C. Carthel, S. Coraluppi, M. Winter, A.R. Cohen, W.J. Godinez, K. Rohr, Y. Kalaidzidis, L. Liang, J. Duncan, H. Shen, Y. Xu, K.E.G. Magnusson, J. Jaldén, H.M. Blau, P. Paul-Gilloteaux, P. Roudot, C. Kervrann, F. Waharte, J.-Y. Tinevez, S.L. Shorte, J. Willemse, K. Celler, G.P. van Wezel, H.-W. Dan, Y.-S. Tsai, C. Ortiz de Solórzano, J.-C. Olivo-Marin, E. Meijering, Objective comparison of particle

tracking methods., Nat. Methods. 11 (2014) 281–289. doi:10.1038/nmeth.2808.

[49] B. Pavie, S. Rajaram, A. Ouyang, J.M. Altschuler, R.J. Steininger, L.F. Wu, S.J. Altschuler, Rapid analysis and exploration of fluorescence microscopy images., J. Vis. Exp. (2014) 2014. doi:10.3791/51280.

[50] M. Balasubramanian, E.L. Schwartz, The isomap algorithm and topological stability., Science. 295 (2002) 7. doi:10.1126/science.295.5552.7a.

[51] L. Van Der Maaten, G. Hinton, Visualizing Data using t-SNE, J. Mach. Learn. Res. 9 (2008) 2579–2605. doi:10.1007/s10479-011-0841-3.

[52] E.D. Amir, K.L. Davis, M.D. Tadmor, E.F. Simonds, J.H. Levine, S.C. Bendall, D.K. Shenfeld, S. Krishnaswamy, G.P. Nolan, D. Pe'er, viSNE enables visualization of high dimensional single-cell data and reveals phenotypic heterogeneity of leukemia., Nat. Biotechnol. 31 (2013) 545–52. doi:10.1038/nbt.2594.

[53] M.D. Brennan, R. Cheong, A. Levchenko, Systems biology. How information theory handles cell signaling and uncertainty., Science. 338 (2012) 334–5. doi:10.1126/science.1227946.

[54] A. Levchenko, I. Nemenman, Cellular noise and information transmission, Curr. Opin. Biotechnol. 28 (2014) 156–164. doi:10.1016/j.copbio.2014.05.002.

[55] I.L. Charles W. Tolman, Frances Cherry, Rene van Hezewijk, Problems of Theoretical Psychology, Captus University Publications, 1995.

[56] M.J. Berridge, P. Lipp, M.D. Bootman, The versatility and universality of calcium signalling., Nat. Rev. Mol. Cell Biol. 1 (2000) 11–21. doi:10.1038/35036035.

[57] G.W.D.E. Youngt, J. Keizer, Youngt, Keizer - Unknown - 1992, 89 (1992) 9895–9899.

[58] G. Dupont, C. Erneux, Simulations of the effects of inositol 1,4,5-trisphosphate 3-kinase and 5-phosphatase activities on Ca2+ oscillations, Cell Calcium. 22 (1997) 321–331. doi:10.1016/S0143-4160(97)90017-8.

[59] J. Keizer, L. Levine, Ryanodine Receptor Adaptation and Ca2+-lnduced Ca2+ Release- Dependent Ca2+ Oscillations, Biophys. J. 71 (1996) 3477–3487. doi:10.1016/S0006-3495(96)79543-7.

[60] B. Fioretti, F. Franciolini, L. Catacuzzeno, A model of intracellular Ca 2+ oscillations based on the activity of the intermediate-conductance Ca 2+-activated K + channels, Biophys. Chem. 113 (2005) 17–23. doi:10.1016/j.bpc.2004.07.037.

[61] M.R. Maurya, S. Subramaniam, A kinetic model for calcium dynamics in RAW 264.7 cells: 1. Mechanisms, parameters, and subpopulational variability., Biophys. J. 93 (2007) 709–28. doi:10.1529/biophysj.106.097469.

[62] G. Lemon, W.G. Gibson, M.R. Bennett, Metabotropic receptor activation, desensitization and sequestration—I: modelling calcium and inositol 1,4,5-trisphosphate dynamics following receptor activation, J. Theor. Biol. 223 (2003) 93–111. doi:10.1016/S0022-5193(03)00079-1.

[63] A. Hoffmann, A. Levchenko, M.L. Scott, D. Baltimore, The IkappaB-NF-kappaB signaling module: temporal control and selective gene activation., Science. 298 (2002) 1241–5. doi:10.1126/science.1071914.

[64] C.Y. Huang, J.E. Ferrell, Ultrasensitivity in the mitogen-activated protein kinase cascade., Proc. Natl. Acad. Sci. U. S. A. 93 (1996) 10078–83.

[65] J.G. Albeck, J.M. Burke, S.L. Spencer, D. a Lauffenburger, P.K. Sorger, Modeling a snap-action, variable-delay switch controlling extrinsic cell death., PLoS Biol. 6 (2008) 2831–2852. doi:10.1371/journal.pbio.0060299.

[66] J.G. Albeck, J.M. Burke, B.B. Aldridge, M. Zhang, D.A. Lauffenburger, P.K. Sorger, Quantitative Analysis of Pathways Controlling Extrinsic Apoptosis in Single Cells, Mol. Cell. 30 (2008) 11–25. doi:10.1016/j.molcel.2008.02.012.

[67] S.L. Spencer, S. Gaudet, J.G. Albeck, J.M. Burke, P.K. Sorger, Non-genetic origins of cell-to-cell variability in TRAIL-induced apoptosis., Nature. 459 (2009) 428–32. doi:10.1038/nature08012.

[68] T. Eissing, H. Conzelmann, E.D. Gilles, F. Allgower, E. Bullinger, P. Scheurich, Bistability analyses of a caspase activation model for receptor-induced apoptosis, J. Biol. Chem. 279 (2004) 36892–36897. doi:10.1074/jbc.M404893200.

[69] D.E. Nelson, a E.C. Ihekwaba, M. Elliott, J.R. Johnson, C. a Gibney, B.E. Foreman, G. Nelson, V. See, C. a Horton, D.G. Spiller, S.W. Edwards, H.P. McDowell, J.F. Unitt, E. Sullivan, R. Grimley, N. Benson, D. Broomhead, D.B. Kell, M.R.H. White, Oscillations in NF-kappaB signaling control the dynamics of gene expression.,

Science. 306 (2004) 704–8. doi:10.1126/science.1099962.

[70] R.E.C. Lee, S.R. Walker, K. Savery, D. a Frank, S. Gaudet, Fold change of nuclear NF-κB determines TNF-induced transcription in single cells., Mol. Cell. 53 (2014) 867–79. doi:10.1016/j.molcel.2014.01.026.

[71] M. Koenigsberger, R. Sauser, M. Lamboley, J.-L. Bény, J.-J. Meister, Ca2+ dynamics in a population of smooth muscle cells: modeling the recruitment and synchronization., Biophys. J. 87 (2004) 92–104. doi:10.1529/biophysj.103.037853.

[72] M.R. Birtwistle, J. Rauch, A. Kiyatkin, E. Aksamitiene, M. Dobrzyński, J.B. Hoek, W. Kolch, B. a Ogunnaike, B.N. Kholodenko, Emergence of bimodal cell population responses from the interplay between analog single-cell signaling and protein expression noise., BMC Syst. Biol. 6 (2012) 109. doi:10.1186/1752-0509-6-109.

[73] J.E. Ferrell, E.M. Machleder, The biochemical basis of an all-or-none cell fate switch in Xenopus oocytes., Science. 280 (1998) 895–898. doi:10.1126/science.280.5365.895.

[74] H. Ryu, M. Chung, M. Dobrzyński, D. Fey, Y. Blum, S.S. Lee, M. Peter, B.N. Kholodenko, N.L. Jeon, O. Pertz, Frequency modulation of ERK activation dynamics rewires cell fate., Mol. Syst. Biol. 11 (2015) 838. doi:10.15252/msb.20156458.

[75] O. Feinerman, J. Veiga, J.R. Dorfman, R.N. Germain, G. Altan-Bonnet, Variability and robustness in T cell activation from regulated hterogeneity in protein levels, Science (80-.). 321 (2008) 1081–1084.

[76] C.-C. Wang, M. Cirit, J.M. Haugh, PI3K-dependent cross-talk interactions converge with Ras as quantifiable inputs integrated by Erk., Mol. Syst. Biol. 5 (2009) 246. doi:10.1038/msb.2009.4.

[77] S. Ahmed, K.G. Grant, L.E. Edwards, A. Rahman, M. Cirit, M.B. Goshe, J.M. Haugh, Data-driven modeling reconciles kinetics of ERK phosphorylation, localization, and activity states., Mol. Syst. Biol. 10 (2014) 718. doi:10.1002/msb.134708.

[78] M.B. Elowitz, A.J. Levine, E.D. Siggia, P.S. Swain, Stochastic gene expression in a single cell., Science (80-.). 297 (2002) 1183–6. doi:10.1126/science.1070919.

[79] K.A. Janes, D.A. Lauffenburger, Models of signalling networks - what cell biologists can gain from them and give to them., J. Cell Sci. 126 (2013) 1913–21.

doi:10.1242/jcs.112045.

[80] R.N. Gutenkunst, J.J. Waterfall, F.P. Casey, K.S. Brown, C.R. Myers, J.P. Sethna, Universally sloppy parameter sensitivities in systems biology models., PLoS Comput. Biol. 3 (2007) 1871–78. doi:10.1371/journal.pcbi.0030189.

[81] Z. Cheng, B. Taylor, D.R. Ourthiague, A. Hoffmann, Distinct single-cell signaling characteristics are conferred by the MyD88 and TRIF pathways during TLR4 activation, Sci. Signal. 8 (2015) 1–13. doi:10.1126/scisignal.aaa5208.

[82] H. Eydgahi, W.W. Chen, J.L. Muhlich, D. Vitkup, J.N. Tsitsiklis, P.K. Sorger, Properties of cell death models calibrated and compared using Bayesian approaches., Mol. Syst. Biol. 9 (2013) 644. doi:10.1038/msb.2012.69.

[83] E.K. Sackmann, A.L. Fulton, D.J. Beebe, The present and future role of microfluidics in biomedical research., Nature. 507 (2014) 181–9. doi:10.1038/nature13118.

[84] Y. Liu, H. Lu, Microfluidics in systems biology—hype or truly useful?, Curr. Opin. Biotechnol. 39 (2016) 215–220. doi:10.1016/j.copbio.2016.04.020.

[85] Y. Yawata, J. Nguyen, R. Stocker, R. Rusconi, Microfluidic studies of biofilm formation in dynamic environments., J. Bacteriol. (2016). doi:10.1128/JB.00118-16.

[86] M.R. Bennett, J. Hasty, Microfluidic devices for measuring gene network dynamics in single cells, Nat. Rev. Genet. 10 (2009) 628–638. doi:10.1038/nrg2625.

[87] A. Prindle, J. Liu, M. Asally, S. Ly, J. Garcia-Ojalvo, G.M. Suel, G.M. Süel, Ion channels enable electrical communication in bacterial communities, Nature. 527 (2015) 59–63. doi:10.1038/nature15709.

[88] J. Liu, A. Prindle, J. Humphries, M. Gabalda-sagarra, M. Asally, D.D. Lee, Metabolic co-dependence gives rise to collective oscillations within biofilms, Nature. 523 (2015) 550–554. doi:10.1038/nature14660.

[89] P. Hersen, M.N. McClean, L. Mahadevan, S. Ramanathan, Signal processing by the HOG MAP kinase pathway., Proc. Natl. Acad. Sci. U. S. A. 105 (2008) 7165–70. doi:10.1073/pnas.0710770105.

[90] R.A. Kellogg, C. Tian, T. Lipniacki, S.R. Quake, S. Tay, Digital signaling decouples

activation probability and population heterogeneity, Elife. 4 (2015) 1–26. doi:10.7554/eLife.08931.

[91] R.A. Kellogg, R.G.-S. Berg, A.A. Leyrat, S.T. Tay, High-throughput microfluidic single-cell analysis pipeline for studies of signaling dynamics, Nat. Protoc. 9 (2014) 1713–1726. doi:10.1038/nprot.2014.120.

[92] R.A. Kellogg, S. Tay, Noise Facilitates Transcriptional Control under Dynamic Inputs, Cell. 160 (2015) 381–392. doi:10.1016/j.cell.2015.01.013.

[93] L. Naomi Handly, A. Pilko, R. Wollman, Paracrine communication maximizes cellular response fidelity in wound signaling, Elife. 4 (2015) 1–18. doi:10.7554/eLife.09652.

[94] Y.-C. Chen, S.G. Allen, P.N. Ingram, R. Buckanovich, S.D. Merajver, E. Yoon, Single-cell Migration Chip for Chemotaxis-based Microfluidic Selection of Heterogeneous Cell Populations., Sci. Rep. 5 (2015) 9980. doi:10.1038/srep09980.

[95] J.E. Toettcher, O.D. Weiner, W. a Lim, Using optogenetics to interrogate the dynamic control of signal transmission by the ras/erk module., Cell. 155 (2013) 1422–34. doi:10.1016/j.cell.2013.11.004.

[96] K. Zhang, L. Duan, Q. Ong, Z. Lin, P.M. Varman, K. Sung, B. Cui, Light-mediated kinetic control reveals the temporal effect of the Raf/MEK/ERK pathway in PC12 cell neurite outgrowth., PLoS One. 9 (2014) e92917. doi:10.1371/journal.pone.0092917.

[97] Y.I. Wu, D. Frey, O.I. Lungu, A. Jaehrig, I. Schlichting, B. Kuhlman, K.M. Hahn, A genetically encoded photoactivatable Rac controls the motility of living cells., Nature. 461 (2009) 104–108. doi:10.1038/nature08241.

[98] W.K. Karunarathne, L. Giri, V. Kalyanaraman, N. Gautam, Optically triggering spatiotemporally confined GPCR activity in a cell and programming neurite initiation and extension, Proc Natl Acad Sci U S A. 110 (2013) E1565-74. doi:10.1073/pnas.1220697110.

[99] P.R. O'Neill, N. Gautam, Subcellular optogenetic inhibition of G proteins generates signaling gradients and cell migration., Mol. Biol. Cell. 25 (2014) 2305–14. doi:10.1091/mbc.E14-04-0870.

[100] X. Wang, L. He, Y.I. Wu, K.M. Hahn, D.J. Montell, Light-mediated activation reveals

a key role for Rac in collective guidance of cell movement in vivo., Nat. Cell Biol. 12 (2010) 591–597. doi:10.1038/ncb2061.

[101] L.R. Polstein, C.A. Gersbach, A light-inducible CRISPR-Cas9 system for control of endogenous gene activation, Nat. Chem. Biol. 11 (2015) 198–200. doi:10.1038/nchembio.1753.

[102] L.E. Dow, J. Fisher, K.P. O'Rourke, A. Muley, E.R. Kastenhuber, G. Livshits, D.F. Tschaharganeh, N.D. Socci, S.W. Lowe, Inducible in vivo genome editing with CRISPR-Cas9., Nat. Biotechnol. 33 (2015) 390–394. doi:10.1038/nbt.3155.

[103] F. Kawano, H. Suzuki, A. Furuya, M. Sato, Engineered pairs of distinct photoswitches for optogenetic control of cellular proteins., Nat. Commun. 6 (2015) 6256. doi:10.1038/ncomms7256.

[104] Z. Yao, J. Petschnigg, R. Ketteler, I. Stagljar, Application guide for omics approaches to cell signaling, Nat. Chem. Biol. 11 (2015) 387–397. doi:10.1038/nchembio.1809.

[105] A. Sigal, R. Milo, A. Cohen, N. Geva-Zatorsky, Y. Klein, Y. Liron, N. Rosenfeld, T. Danon, N. Perzov, U. Alon, Variability and memory of protein levels in human cells., Nature. 444 (2006) 643–6. doi:10.1038/nature05316.

[106] A. Bar-Even, J. Paulsson, N. Maheshri, M. Carmi, E. O'Shea, Y. Pilpel, N. Barkai, Noise in protein expression scales with natural protein abundance., Nat. Genet. 38 (2006) 636–643. doi:10.1038/ng1807.

[107] J.P. Junker, A. Van Oudenaarden, Every cell is special: Genome-wide studies add a new dimension to single-cell biology, Cell. 157 (2014) 8–11. doi:10.1016/j.cell.2014.02.010.

[108] A. Sanchez, I. Golding, Genetic Determinants and Cellular Constraints in Noisy Gene Expression, Science (80-.). (2013) 1188–1193.

[109] J. Selimkhanov, B. Taylor, J. Yao, a. Pilko, J. Albeck, a. Hoffmann, L. Tsimring, R. Wollman, Accurate information transmission through dynamic biochemical signaling networks, Science (80-.). 346 (2014) 1370–1373. doi:10.1126/science.1254933.

[110] M. Voliotis, R.M. Perrett, C. McWilliams, C. a McArdle, C.G. Bowsher, Information transfer by leaky, heterogeneous, protein kinase signaling systems., Proc. Natl. Acad.

Sci. U. S. A. 111 (2014) E326-33. doi:10.1073/pnas.1314446111.

[111] A.S. Hansen, E.K.O. Shea, Limits on Information Transduction through Amplitude and Frequency Regulation of Transcription Factor Activity, (2015).

[112] S.J. Altschuler, L.F. Wu, Cellular Heterogeneity: Do Differences Make a Difference?, Cell. 141 (2010) 559–563. doi:10.1016/j.cell.2010.04.033.

[113] J.J. Hughey, M. V. Gutschow, B.T. Bajar, M.W. Covert, Single-cell variation leads to population invariance in NF- B signaling dynamics, Mol. Biol. Cell. 26 (2014) 583–590. doi:10.1091/mbc.E14-08-1267.

[114] R. a Kellogg, S. Tay, Noise Facilitates Transcriptional Control under Dynamic Inputs, Cell. 160 (2015) 381–392. doi:10.1016/j.cell.2015.01.013.

[115] V. Piras, K. Selvarajoo, The reduction of gene expression variability from single cells to populations follows simple statistical laws, Genomics. (2014) 137–144. doi:10.1016/j.ygeno.2014.12.007.

[116] U. Rand, M. Rinas, J. Schwerk, G. Nöhren, M. Linnes, A. Kröger, M. Flossdorf, K. Kály-Kullai, H. Hauser, T. Höfer, M. Köster, Multi-layered stochasticity and paracrine signal propagation shape the type-I interferon response., Mol. Syst. Biol. 8 (2012) 584. doi:10.1038/msb.2012.17.

[117] A.K. Shalek, R. Satija, J. Shuga, J.J. Trombetta, D. Gennert, D. Lu, P. Chen, R.S. Gertner, J.T. Gaublomme, N. Yosef, S. Schwartz, B. Fowler, S. Weaver, J. Wang, X. Wang, R. Ding, R. Raychowdhury, N. Friedman, N. Hacohen, H. Park, A.P. May, A. Regev, Single-cell RNA-seq reveals dynamic paracrine control of cellular variation., Nature. 509 (2014) 363–9. doi:10.1038/nature13437.

[118] J.R.S. Newman, S. Ghaemmaghami, J. Ihmels, D.K. Breslow, M. Noble, J.L. DeRisi, J.S. Weissman, Single-cell proteomic analysis of S. cerevisiae reveals the architecture of biological noise., Nature. 441 (2006) 840–846. doi:10.1038/nature04785.

[119] B. Enyedi, P. Niethammer, Mechanisms of epithelial wound detection, Trends Cell Biol. (2015) 1–10. doi:10.1016/j.tcb.2015.02.007.

[120] J. Yin, K. Xu, J. Zhang, A. Kumar, F.-S.X. Yu, Wound-induced ATP release and EGF receptor activation in epithelial cells., J. Cell Sci. 120 (2007) 815–25.

doi:10.1242/jcs.03389.

[121] R. Wetzker, F. Böhmer, Transactivation joins multiple tracks to the ERK/MAPK cascade, Nat. Rev. Mol. Cell Biol. 4 (2003) 651–657.

[122] J. V Cordeiro, A. Jacinto, The role of transcription-independent damage signals in the initiation of epithelial wound healing., Nat. Rev. Mol. Cell Biol. 14 (2013) 249–62. doi:10.1038/nrm3541.

[123] M. Sholley, G.M. Jr, Cortaon RS, Cellular migration and replication in endothelial regeneration: a study using irradiated endothelial cultures, Lab. Investig. 36 (1977) 18–25.

[124] J. Akerboom, N. Carreras Calderón, L. Tian, S. Wabnig, M. Prigge, J. Tolö, A. Gordus, M.B. Orger, K.E. Severi, J.J. Macklin, R. Patel, S.R. Pulver, T.J. Wardill, E. Fischer, C. Schüler, T.-W. Chen, K.S. Sarkisyan, J.S. Marvin, C.I. Bargmann, D.S. Kim, S. Kügler, L. Lagnado, P. Hegemann, A. Gottschalk, E.R. Schreiter, L.L. Looger, Genetically encoded calcium indicators for multi-color neural activity imaging and combination with optogenetics., Front. Mol. Neurosci. 6 (2013) 2. doi:10.3389/fnmol.2013.00002.

[125] Y. Zhao, S. Araki, J. Wu, T. Teramoto, Y.-F. Chang, M. Nakano, A.S. Abdelfattah, M. Fujiwara, T. Ishihara, T. Nagai, R.E. Campbell, An expanded palette of genetically encoded Ca^{2+} indicators., Science. 333 (2011) 1888–91. doi:10.1126/science.1208592.

[126] B.N. Armbruster, X. Li, M.H. Pausch, S. Herlitze, B.L. Roth, Evolving the lock to fit the key to create a family of G protein-coupled receptors potently activated by an inert ligand., Proc. Natl. Acad. Sci. U. S. A. 104 (2007) 5163–8. doi:10.1073/pnas.0700293104.

[127] S. Dong, J. a Allen, M. Farrell, B.L. Roth, A chemical-genetic approach for precise spatio-temporal control of cellular signaling., Mol. Biosyst. 6 (2010) 1376–80. doi:10.1039/c002568m.

[128] W.N. Ross, Understanding calcium waves and sparks in central neurons., Nat. Rev. Neurosci. 13 (2012) 157–68. doi:10.1038/nrn3168.

[129] H.C. Berg, Random walks in biology, Princeton University Press, 1993.

[130] S. Uda, T.H. Saito, T. Kudo, T. Kokaji, T. Tsuchiya, H. Kubota, Y. Komori, Y. Ozaki, S. Kuroda, Robustness and compensation of information transmission of signaling pathways., Science. 341 (2013) 558–61. doi:10.1126/science.1234511.

[131] J.O. Dubuis, G. Tkacik, E.F. Wieschaus, T. Gregor, W. Bialek, Positional information, in bits., Proc. Natl. Acad. Sci. U. S. A. 110 (2013) 16301–8. doi:10.1073/pnas.1315642110.

[132] K.J. Sonnemann, W.M. Bement, Wound repair: toward understanding and integration of single-cell and multicellular wound responses., Annu. Rev. Cell Dev. Biol. 27 (2011) 237–63. doi:10.1146/annurev-cellbio-092910-154251.

[133] T. Hiratsuka, Y. Fujita, H. Naoki, K. Aoki, Y. Kamioka, M. Matsuda, Intercellular propagation of extracellular signal-regulated kinase activation revealed by in vivo imaging of mouse skin, Elife. 4 (2015) 1–18. doi:10.7554/eLife.05178.

[134] Y. Kumagai, H. Naoki, E. Nakasyo, Y. Kamioka, E. Kiyokawa, M. Matsuda, Heterogeneity in ERK activity as visualized by in vivo FRET imaging of mammary tumor cells developed in MMTV-Neu mice., Oncogene. 34 (2014) 1–7. doi:10.1038/onc.2014.28.

[135] I. Ben-Shlomo, S. Yu Hsu, R. Rauch, H.W. Kowalski, A.J.W. Hsueh, Signaling receptome: a genomic and evolutionary perspective of plasma membrane receptors involved in signal transduction., Sci. STKE. 2003 (2003) RE9. doi:10.1126/stke.2003.187.re9.

[136] I. Ben-Shlomo, R. Rauch, O. Avsian-Kretchmer, A.J.W. Hsueh, Matching receptome genes with their ligands for surveying paracrine/autocrine signaling systems., Mol. Endocrinol. 21 (2007) 2009–14. doi:10.1210/me.2007-0087.

[137] T. Sasaki, B. Granovskiy, R.P. Mann, D.J.T. Sumpter, S.C. Pratt, Ant colonies outperform individuals when a sensory discrimination task is difficult but not when it is easy, Proc. Natl. Acad. Sci. 110 (2013) 13769–13773. doi:10.1073/pnas.1304917110.

[138] A.B. Kao, I.D. Couzin, P.R.S. B, Decision accuracy in complex environments is often maximized by small group sizes Decision accuracy in complex environments is often maximized by small group sizes, (2014).

[139] D.J. Hoare, I.D. Couzin, J.G.J. Godin, J. Krause, Context-dependent group size choice

in fish, Anim. Behav. 67 (2004) 155–164. doi:10.1016/j.anbehav.2003.04.004.

[140] C. Sueur, J.-L. Deneubourg, O. Petit, I.D. Couzin, Group size, grooming and fission in primates: a modeling approach based on group structure., J. Theor. Biol. 273 (2011) 156–166. doi:10.1016/j.jtbi.2010.12.035.

[141] L. Batsilas, A.M. Berezhkovskii, S.Y. Shvartsman, Stochastic Model of Autocrine and Paracrine Signals in Cell Culture Assays, 85 (2003).

[142] C.B. Muratov, S.Y. Shvartsman, Discrete Models of Autocrine Cell Communication in Epithelial Layers, 84 (2003) 3624–3635.

[143] C.B. Muratov, S.Y. Shvartsman, Long-Range Signal Transmission in Autocrine Relays, 84 (2003).

[144] L.E. Kreuz, A.H. Levy, L.E.O.E. Kreuz, Interferon Physical Properties of Chick Interferon, 89 (1965).

[145] T. Gregor, D.W. Tank, E.F. Wieschaus, W. Bialek, Probing the limits to positional information., Cell. 130 (2007) 153–64. doi:10.1016/j.cell.2007.05.025.

[146] J. Debnath, S.K. Muthuswamy, J.S. Brugge, Morphogenesis and oncogenesis of MCF-10A mammary epithelial acini grown in three-dimensional basement membrane cultures, Methods. 30 (2003) 256–268. doi:10.1016/S1046-2023(03)00032-X.

[147] M.S. Ferry, I. a Razinkov, J. Hasty, Microfluidics for synthetic biology: from design to execution., 1st ed., Elsevier Inc., 2011. doi:10.1016/B978-0-12-385075-1.00014-7.

[148] A. Edelstein, N. Amodaj, K. Hoover, R. Vale, N. Stuurman, Computer control of microscopes using μManager., Curr. Protoc. Mol. Biol. Chapter 14 (2010) Unit14.20. doi:10.1002/0471142727.mb1420s92.

[149] W.J. Polacheck, J.L. Charest, R.D. Kamm, Interstitial flow influences direction of tumor cell migration through competing mechanisms., Proc. Natl. Acad. Sci. U. S. A. 108 (2011) 11115–11120. doi:10.1073/pnas.1103581108.

[150] J. V Cordeiro, A. Jacinto, The role of transcription-independent damage signals in the initiation of epithelial wound healing., Nat. Rev. Mol. Cell Biol. 14 (2013) 249–62. doi:10.1038/nrm3541.

[151] E.M. Schwiebert, A. Zsembery, Extracellular ATP as a signaling molecule for epithelial cells, Biochim. Biophys. Acta - Biomembr. 1615 (2003) 7–32. doi:10.1016/S0005-2736(03)00210-4.

[152] R. Corriden, P. a Insel, Basal release of ATP: an autocrine-paracrine mechanism for cell regulation., Sci. Signal. 3 (2010) re1. doi:10.1126/scisignal.3104re1.

[153] J. Pastor, M. Calonge, Epidermal growth factor and corneal wound healing. A multicenter study., Cornea. 11 (1992) 311–314.

[154] S. Feldman, The effect of epidermal growth factor on corneal wound healing: practical considerations for therapeutic use, Refract Corneal Surg. 7 (1991) 232–239.

[155] A. Caporossi, C. Manetti, Epidermal growth factor in topical treatment following epikeratoplasty., Ophthalmologica. 205 (1992) 121–124.

[156] M.D. Bootman, Calcium signaling., Cold Spring Harb. Perspect. Biol. 4 (2012) a011171. doi:10.1101/cshperspect.a011171.

[157] W. Razzell, I.R. Evans, P. Martin, W. Wood, Calcium Flashes Orchestrate the Wound Inflammatory Response through DUOX Activation and Hydrogen Peroxide Release., Curr. Biol. 23 (2013) 424–429. doi:10.1016/j.cub.2013.01.058.

[158] B. Sun, J. Lembong, V. Normand, M. Rogers, H. a Stone, Spatial-temporal dynamics of collective chemosensing., Proc. Natl. Acad. Sci. U. S. A. 109 (2012) 7753–8. doi:10.1073/pnas.1121338109.

[159] N.J. Warren, M.H. Tawhai, E.J. Crampin, Mathematical modelling of calcium wave propagation in mammalian airway epithelium: evidence for regenerative ATP release., Exp. Physiol. 95 (2010) 232–49. doi:10.1113/expphysiol.2009.049585.

[160] T. Höfer, a Politi, R. Heinrich, Intercellular Ca2+ wave propagation through gap-junctional Ca2+ diffusion: a theoretical study., Biophys. J. 80 (2001) 75–87. doi:10.1016/S0006-3495(01)75996-6.

[161] G. Dupont, L. Combettes, G.S. Bird, J.W. Putney, Calcium oscillations., Cold Spring Harb. Perspect. Biol. 3 (2011). doi:10.1101/cshperspect.a004226.

[162] S. Locovei, J. Wang, G. Dahl, Activation of pannexin 1 channels by ATP through P2Y

receptors and by cytoplasmic calcium, 580 (2006) 239–244. doi:10.1016/j.febslet.2005.12.004.

[163] C.-L. Ho, C.-Y. Yang, W.-J. Lin, C.-H. Lin, Ecto-Nucleoside Triphosphate Diphosphohydrolase 2 Modulates Local ATP-Induced Calcium Signaling in Human HaCaT Keratinocytes., PLoS One. 8 (2013) e57666. doi:10.1371/journal.pone.0057666.

[164] G.R. Dubyak, Both sides now: multiple interactions of ATP with pannexin-1 hemichannels. Focus on "A permeant regulating its permeation pore: inhibition of pannexin 1 channels by ATP"., Am. J. Physiol. Cell Physiol. 296 (2009) C235-41. doi:10.1152/ajpcell.00639.2008.

[165] W.G. Junger, Immune cell regulation by autocrine purinergic signalling., Nat. Rev. Immunol. 11 (2011) 201–12. doi:10.1038/nri2938.

[166] R. Corriden, P. a Insel, Basal release of ATP: an autocrine-paracrine mechanism for cell regulation., Sci. Signal. 3 (2010) re1. doi:10.1126/scisignal.3104re1.

[167] E.R. Block, A.R. Matela, N. SundarRaj, E.R. Iszkula, J.K. Klarlund, Wounding induces motility in sheets of corneal epithelial cells through loss of spatial constraints: role of heparin-binding epidermal growth factor-like growth factor signaling., J. Biol. Chem. 279 (2004) 24307–12. doi:10.1074/jbc.M401058200.

[168] J.K. Klarlund, E.R. Block, Free edges in epithelia as cues for motility, Cell Adhes. Migr. 5 (2011) 106–110. doi:10.4161/cam.5.2.13728.

[169] U. V Wesley, P.F. Bove, M. Hristova, S. McCarthy, A. van der Vliet, Airway epithelial cell migration and wound repair by ATP-mediated activation of dual oxidase 1., J. Biol. Chem. 282 (2007) 3213–20. doi:10.1074/jbc.M606533200.

[170] W.J. Gault, B. Enyedi, P. Niethammer, Osmotic surveillance mediates rapid wound closure through nucleotide release, J. Cell Biol. 207 (2014) 767–782. doi:10.1083/jcb.201408049.

[171] H. Takada, K. Furuya, M. Sokabe, Mechanosensitive ATP release from hemichannels and Ca^{2+} influx through TRPC6 accelerate wound closure in keratinocytes., J. Cell Sci. 127 (2014) 4159–71. doi:10.1242/jcs.147314.

[172] S. Nakagawa, T. Omura, A. Yonezawa, I. Yano, T. Nakagawa, K. Matsubara, Extracellular nucleotides from dying cells act as molecular signals to promote wound repair in renal tubular injury., Am. J. Physiol. Renal Physiol. (2014) ajprenal.00196.2014. doi:10.1152/ajprenal.00196.2014.

[173] V.E. Klepeis, I. Weinger, E. Kaczmarek, V. Trinkaus-Randall, P2Y receptors play a critical role in epithelial cell communication and migration., J. Cell. Biochem. 93 (2004) 1115–33. doi:10.1002/jcb.20258.

[174] V.E. Klepeis, A. Cornell-bell, V. Trinkaus-randall, Growth factors but not gap junctions play a role in injury-induced Ca 2 + waves in epithelial cells, (2001).

[175] E.R. Block, J.K. Klarlund, Wounding Sheets of Epithelial Cells Activates the Epidermal Growth Factor Receptor through Distinct Short- and Long-Range Mechanisms, 19 (2008) 4909–4917. doi:10.1091/mbc.E08.

[176] M. Idzko, D. Ferrari, H.K. Eltzschig, Nucleotide signalling during inflammation., Nature. 509 (2014) 310–7. doi:10.1038/nature13085.

[177] J. Yu, X. Liao, L. Li, L. Lv, X. Zhi, J. Yu, J. Yu, A preliminary study of the role of extracellular -5 ′ - nucleotidase in breast cancer stem cells and epithelial-mesenchymal transition, (2017) 132–140. doi:10.1007/s11626-016-0089-y.

[178] R.T. Lawrence, E.M. Perez, C.A. Blau, C.P. Miller, K.M. Haas, H.Y. Irie, R.T. Lawrence, E.M. Perez, D. Herna, The Proteomic Landscape of Triple-Negative Breast Resource The Proteomic Landscape of Triple-Negative Breast Cancer, (2015) 630–644. doi:10.1016/j.celrep.2015.03.050.

[179] S. a Lévesque, E.G. Lavoie, J. Lecka, F. Bigonnesse, J. Sévigny, Specificity of the ecto-ATPase inhibitor ARL 67156 on human and mouse ectonucleotidases., Br. J. Pharmacol. 152 (2007) 141–150. doi:10.1038/sj.bjp.0707361.

[180] S. a Eming, T. Krieg, J.M. Davidson, Inflammation in wound repair: molecular and cellular mechanisms., J. Invest. Dermatol. 127 (2007) 514–25. doi:10.1038/sj.jid.5700701.

[181] I. a Darby, T.D. Hewitson, Fibroblast differentiation in wound healing and fibrosis., Int. Rev. Cytol. 257 (2007) 143–79. doi:10.1016/S0074-7696(07)57004-X.

[182] Y. Feng, C. Santoriello, M. Mione, A. Hurlstone, P. Martin, Live imaging of innate immune cell sensing of transformed cells in zebrafish larvae: parallels between tumor initiation and wound inflammation., PLoS Biol. 8 (2010) e1000562. doi:10.1371/journal.pbio.1000562.

[183] M. Schäfer, S. Werner, Cancer as an overhealing wound: an old hypothesis revisited., Nat. Rev. Mol. Cell Biol. 9 (2008) 628–638. doi:10.1038/nrm2455.

[184] R. Rivera-Pomar, H. Jackle, From gradients to stripes in Drosophila embryogenesis: filling in the gaps, Trends Genet. 12 (1996) 478–483. doi:https://doi.org/10.1016/0168-9525(96)10044-5.

[185] a Bejsovec, E. Wieschaus, Segment polarity gene interactions modulate epidermal patterning in Drosophila embryos., Development. 119 (1993) 501–517.

[186] M. Nahmad, A.D. Lander, Spatiotemporal mechanisms of morphogen gradient interpretation., Curr. Opin. Genet. Dev. 21 (2011) 726–31. doi:10.1016/j.gde.2011.10.002.

[187] J.C. Pearson, M.T. Juarez, M. Kim, Ø. Drivenes, W. McGinnis, Multiple transcription factor codes activate epidermal wound-response genes in Drosophila., Proc. Natl. Acad. Sci. U. S. A. 106 (2009) 2224–9. doi:10.1073/pnas.0810219106.

[188] F.X. Yu, I.K. Gipson, Y. Guo, Differential gene expression in healing rat corneal epithelium, Invest Ophthalmol Vis Sci. 36 (1995) 1997–2007. http://www.ncbi.nlm.nih.gov/entrez/query.fcgi?cmd=Retrieve&db=PubMed&dopt=Citation&list_uids=7544780.

[189] N. V Welham, C. Ling, J. a Dawson, C. Kendziorski, S.L. Thibeault, Microarray-based characterization of differential gene expression during vocal fold wound healing in rats, (2015) 311–321. doi:10.1242/dmm.

[190] S.A. McKinney, C.S. Murphy, K.L. Hazelwood, M.W. Davidson, L.L. Looger, A bright and photostable photoconvertible fluorescent protein., Nat. Methods. 6 (2009) 131–3. doi:10.1038/nmeth.1296.

[191] G.U. Nienhaus, K. Nienhaus, A. Hölzle, S. Ivanchenko, F. Renzi, F. Oswald, M. Wolff, F. Schmitt, C. Röcker, B. Vallone, W. Weidemann, R. Heilker, H. Nar, J. Wiedenmann, Photoconvertible fluorescent protein EosFP: biophysical properties and cell biology applications., Photochem. Photobiol. 82 (2005) 351–358.

doi:10.1562/2005-05-19-RA-533.

[192] J. Wiedenmann, S. Ivanchenko, F. Oswald, F. Schmitt, C. Röcker, A. Salih, K.-D. Spindler, G.U. Nienhaus, EosFP, a fluorescent marker protein with UV-inducible green-to-red fluorescence conversion., Proc. Natl. Acad. Sci. U. S. A. 101 (2004) 15905–10. doi:10.1073/pnas.0403668101.

[193] H. Weavers, J. Liepe, A. Sim, W. Wood, P. Martin, M.P.H. Stumpf, Systems Analysis of the Dynamic Inflammatory Response to Tissue Damage Reveals Spatiotemporal Properties of the Wound Attractant Gradient, Curr. Biol. 26 (2016) 1975–1989. doi:10.1016/j.cub.2016.06.012.

[194] K. Lane, D. Van Valen, M.M. DeFelice, D.N. Macklin, T. Kudo, A. Jaimovich, A. Carr, T. Meyer, D. Pe'er, S.C. Boutet, M.W. Covert, Measuring Signaling and RNA-Seq in the Same Cell Links Gene Expression to Dynamic Patterns of NF-κB Activation, 2017. doi:10.1016/j.cels.2017.03.010.